UNIVERSITÀ DEGLI STUDI DI MILANO–BICOCCA
LAUREA MAGISTRALE IN FISICA

DECEMBER 2007

THE LHCb RICH PMTs READOUT ELECTRONICS AND THE MONITORING OF THE HPDs QUANTUM EFFICIENCY

Marco Villa 079525

Internal supervisor: Clara Matteuzzi
External supervisor: Carmelo D'Ambrosio
Co–supervisor: Gianluigi Pessina

INDEX

PREFACE

LHCb is one of the four main experiments under construction on the Large Hadron Collider at CERN. Its purpose is to study CP violation in B mesons and to look for new physics effects in rare decays of b–hadrons. Particle identification will be essential to enhance the signal/background ratio in the selection of physics channels. For this reason, the Ring Imaging Cherenkov technique has been implemented: two RICH detectors (RICH1 and RICH2) have been designed to cover the wide momentum range 1–150 GeV/c. The produced Cherenkov photons will be focused on two planes of Hybrid PhotoDetectors (HPDs), which are sensitive to external magnetic fields and then need to be shielded. Despite the shielding, however, there will be some fringe field inside the HPDs volume and so it is necessary to experimentally check what is the behaviour of each photodetector when the LHCb dipole magnet is on and the HPDs are illuminated by test patterns.
In RICH2, two LED projectors based on the Digital Light Processing technology are exploited to generate the test patterns, which have to be precisely aligned on the two HPD planes. The matching procedure is carried out using six PMTs permanently placed inside the HPD matrices.
The work described in this thesis concerns the design, realization and test of the PMTs readout system, both on the HW and SW level. In the last chapter, I will also try to evaluate the possibility to periodically monitor the HPDs Q.E. using the same beamer selected for the magnetic distortion tests.
Chapter 1 is an introduction to CERN and the LHCb experiment. Paragraph 1.2 focuses on the two RICH sub–systems, while in 1.3 the HPD working principle is described.
In paragraph 2.1 I describe the PMTs installed in the RICH2, while the rest of the chapter is dedicated to the DLP projectors to be used during the magnetic distortion tests. In particular, 2.2 illustrates the DLP technology, while 2.4 and 2.5 are about the beamers tests.
Chapter 3 is dedicated to the PMTs readout electronics design, realization and test. After a theoretical study carried out in paragraph 3.1, in 3.2 I describe the realized shaper amplifier prototype. In 3.3 the choice of the digitiser to be installed in cascade to the shaper is discussed and the DAQ software program is described, while 3.4 summarizes the results obtained testing the prototype with the real signals. In 3.5 the final six–channel shaper amplifier + ADC is presented and tested, while 3.6 describes the installation of this module in the pit environment.
Finally, in chapter 4 I estimate the sensitivity of the HPD Q.E. monitoring based on the magnetic distortion test apparatus.

1 – LHCb

Figure 1.1: aerial view of CERN accelerator complex. The circles superimposed on the picture represent three accelerator machines displaced in underground tunnels. The smallest circle is the PS, the medium one is the SPS and the largest one is the LEP tunnel, now used for the LHC.

CERN (Conseil Européen pour la Recherche Nucléaire) is the world largest High Energy Physics research center. Located on the Swiss–French border, CERN houses a variety of different accelerator machines and experiments. The most important project under construction at the moment is the Large Hadron Collider (LHC), which is scheduled to start in 2008 and will accelerate alternatively either protons or lead ions.
Particles extracted from plasmas are pre–accelerated by linear accelerators, Linac2 for protons and Linac3 for lead ions, and then they are injected into the Proton–Synchrotron Booster (PSB). From here the particle bunches reach the Proton–Synchrotron (PS) ring and, when they are energetic enough, they are transferred into the Super Proton–Synchrotron (SPS). Finally, the protons or lead ions bunches enter into the LHC ring.
LHC is assembled one hundred meters below ground level, in the 26659 meters long tunnel which housed the Large Electron–Positron collider (LEP) in the past (Figure 1.1). According to the design reports, the LHC beam will have the characteristics listed in Table 1.1[1]:

Particles collided	p p	Pb Pb
Energy [TeV]	7.00	2.76 / nucleon
Maximum luminosity [10^{30} cm^{-2}s^{-1}]	$1.0 \cdot 10^{4}$	$1.0 \cdot 10^{-3}$
Bunch crossing frequency [MHz]	40.08	10.02
Bunch length [cm]	7.55	7.94
Bunch radius [μm]	16.6	15.9

Table 1.1: LHC beam specifications in p p and Pb Pb operating modes.

Four big experiments have been placed on the LHC interaction points. Two of them, ATLAS (A large Toroidal LHC ApparatuS) and CMS (Compact Muon Solenoid), are general purpose detectors, mainly devoted to the Higgs boson and supersymmetric particles search. The other two are dedicated experiments, specifically optimised to explore a restricted number of physics phenomena; their names are ALICE (A Large Ion Collider Experiment) and LHCb (Large Hadron Collider beauty experiment).

1.1 – THE LHCb EXPERIMENT

A proton–proton collision with a centre of mass energy of 7+7 TeV has a high $b\bar{b}$ production cross section, about 500 μbarn[2]. As a consequence, the LHC will be by far the most copious source of beauty particles ever built. The high luminosity of the machine will make available with large statistics B_u, B_d, B_s, B_c mesons and a variety of b–hadrons. This suggested to install on LHC a specialised b–physics detector. The name of this detector is LHCb and it is located in IP8. Its purpose is to study with high precision CP violation in the B mesons system and to look for new physics effects in rare decays of b–hadrons. The experimental data is expected to bring a deep understanding of the flavour physics inside the Standard Model and to suggest possible extensions.

A 7 TeV proton has a De Broglie wavelength of the order of 10^{-19} m, much less than the typical baryon dimension, which is of the order of 10^{-13} m. For this reason, LHC collisions are actually parton–parton collisions. Furthermore, at 7 TeV the proton partonic distribution functions are such that it is very likely that the interaction happens between partons with very different momenta. Although the centre of mass of the two crossing protons is still in the laboratory reference frame, the centre of mass of the colliding partons is not. For momentum conservation, the $b\bar{b}$ pairs produced in the anelastic scattering will be highly Lorentz boosted along the initial proton direction and will move in the same forward or backward direction. The composed particles generated in the successive hadronization of the $b\bar{b}$ pair will of course have memory of this and will move in small cones around the initial proton beam direction. The events of interest for b–physics are not evenly distributed around the interaction point, but they are strongly peaked at small angles with respect to the beam axis. This conclusion is well illustrated in Figure 1.2, which shows the calculated polar angle distribution for b and $\bar{b}$ –hadrons produced in a proton–proton collision at LHC[3].

There is evidently no need to surround the interaction point with detectors, since the most of the particle trajectories of interest lie inside a cone of a few hundred mrad aperture. The LHCb design is then very different from the one of the others LHC

detectors and from collider experiments in general. The chosen geometry is that of a single–arm forward spectrometer. In this configuration the detector can obtain the same precision as a double–arm one, but the statistics collected is cut in half. Due to the high beam luminosity and to the large cross section for b–hadrons production, the reduced statistics will not be a problem. Figure 1.3 shows the actual LHCb layout. The total length of the detector is about 20 meters and it is limited by the cavern dimension. In order to analyse the experimental data, a right handed coordinate system has been defined. Its origin has been fixed on the interaction point, *z* runs along the beam axis, *y* points upwards and *x* points toward the centre of the LHC ring.

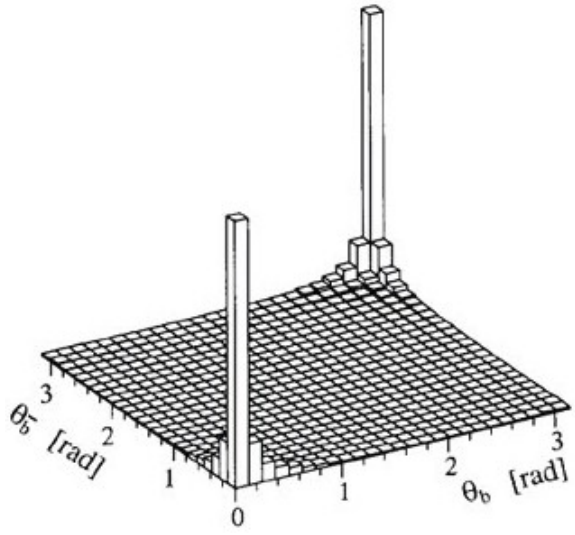

Figure 1.2: polar angle distribution for b and $\bar{b}$ –hadrons produced in a proton–proton collision at LHC. The simulation has been carried out using the PYTHIA event generator.

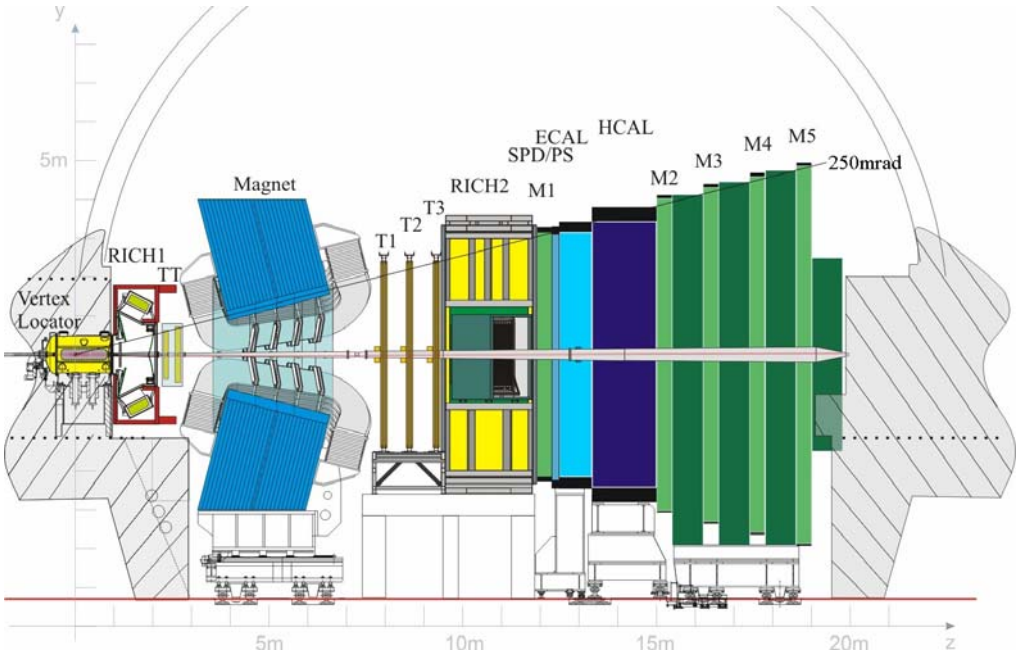

Figure 1.3: side view of the LHCb detector (non–bending plane), with the coordinate system and the dimensions superimposed. The sub–detector structure is also visible.

Given the overall detector shape, the single sub–detectors have to be designed to adapt to the events of interest. In particular, a robust and highly performing trigger and a particle identification system are mandatory in order to study the wide range of decay modes.

VERTEX LOCATOR (VELO). The hadrons produced in proton–proton primary interactions in LHC and containing beauty (anti–beauty) quarks are highly Lorentz boosted in the laboratory reference frame and they travel about one centimetre before decaying. The spatial localization of the secondary vertices originated by b–hadrons decays is an important information for the event selection system. The primary interaction point is then surrounded by a vertex locator. This device is constituted by 21 silicon stations placed along the beam direction, which can measure particle trajectories in cylindrical coordinates (r, θ, z). The silicon stations are placed at a radial distance from the beam which is smaller than the aperture required by LHC during injection and must therefore be retractable[4].

MAGNET. To measure charged particle momentum it is necessary to introduce a magnetic field. LHCb requires a dipole field with a free aperture of ±300 mrad horizontally and ±250 mrad vertically. In particular, the tracking detectors have to provide momentum measurement for charged particles with a precision better than 0.5% for momenta up to 200 GeV/c. This demands an integrated field of 4 Tm for tracks originating near the primary interaction point. Furthermore, a good field uniformity along the transverse coordinate is required by the muon trigger.
The complicated shape of the coils and the high magnetic forces would make a superconducting magnet too expensive and mechanically unstable. LHCb has, therefore, moved to the design of a warm magnet cooled with water. To reduce electrical power requirements to about 4.2 MW, the pole faces are shaped to follow the acceptance angles of the experiment. Besides significantly lower costs, faster construction and lower risks, the warm coils offer additional advantages. A warm dipole permits rapid ramping–up of the field, synchronous to the ramping–up of LHC magnets, as well as regular field inversions to reduce systematic errors on asymmetries in CP violation[5].

TRACKING SYSTEM (TT, T1, T2, T3). The tracking system is composed by four tracking stations. Its purpose is to detect tracks in the zone between RICH1 and RICH2 and to measure particles momenta from their curvature in the magnetic field. This system also has to determinate the direction of the particles crossing the two RICH detectors and it has to connect the information from the Vertex Locator with the information from the calorimeters and the muon chambers.
The tracking stations named respectively T1, T2 and T3 are placed downstream the magnet, just before RICH2. Each of these three stations is built using two different technologies. The innermost part, where the particle flux is greater, is called Inner Tracker (IT), while the outermost part is named Outer Tracker (OT). The IT covers a cross–shaped area around the beam pipe, approximately 120 cm wide and 40 cm high. Each IT station consists of four silicon strip detection layers, with two ±5° stereo views sandwitched in between two layers with vertical strips[6]. The OT, on the other hand, is constituted of straw–tube drift chambers[7].
The fourth tracking station is called Trigger Tracker (TT) and it is placed between RICH1 and the magnet. The TT station fulfils a two–fold purpose. Firstly, it is used to

reconstruct the trajectories of low–momentum particles, which are bent out of the experiment acceptance by the magnetic field and thus do not reach stations T1–T3. Moreover, the TT is used in the trigger to assign transverse momentum information to large impact parameter tracks. The TT is built entirely using the IT technology, but, in contrast with stations T1–T3, it will be split in two sub–stations, with a gap of 30 cm in between the second and third detection layers[6].

CALORIMETERS (SPD/PS, ECAL, HCAL). The main purpose of the LHCb calorimeter system is the identification of photons, electrons and hadrons and the measurement of their energies and positions. The collected data is immediately used in the L0 trigger to select the high p_T particles. Since this is a real–time selection, the information from the calorimeters has to be available within the 25 ns separating two bunch crossings. The selected data is also used for the complete reconstruction of electromagnetic and hadronic showers, but this analysis requires long time and so it is not part of the L0 trigger. The other essential function of the calorimeter system is the detection of photons with enough precision to allow identification of decay channels which contain in the final state a prompt photon or a neutral pion.
The calorimeter system is constituted of three different sections. The first one, i.e. the one closer to the interaction point, is constituted of two detection planes located just before and just after a 12 mm thick lead wall. The detector elements are 15 mm thick scintillator pads, which are called respectively Scintillator Pad Detector (SPD) and PreSower detector (PS). A groove in the scintillator holds the helicoidal WaveLength Shifter (WLS) fiber which collects the scintillation light. The light from both WLS fiber ends is sent by long clear fibers to multianode photomultipliers that are located above and below the detector. Since the number of interacting particles per unit surface varies of two orders of magnitude moving from centre to the outer edge, the SPD/PS has been divided in three concentric zones with different spatial granularity.
The Electromagnetic Calorimeter (ECAL) is placed just downstream the PS. It has a sampling structure of 2 mm lead sheets interspersed with 4 mm thick scintillator plates. The produced light is collected by WLS filers, which are then bunched together and read by phototubes. Similarly to SPD/PS, ECAL is divided in three zones with different spatial granularity.
The Hadronic Calorimeter (HCAL) is the last calorimeter section. The sampling structure has 16 mm thick iron plates spaced with 4 mm thick scintillator plates, readout via WLS fibers. Given the dimensions of the hadronic showers and the performance requirements of the hadron trigger, the HCAL cells were chosen larger than those of ECAL. Furthermore, a lateral segmentation into only two zones has been adopted[8].

MUON SYSTEM (M1, M2, M3, M4, M5). Muon triggering and offline muon identification are fundamental requirements of the LHCb experiment. Muons are present in the final states of many CP–sensitive B decays, in particular the two "gold–plated" channels $B_d^0 \to J/\psi\left(\mu^+\mu^-\right)K_S^0$ and $B_s^0 \to J/\psi\left(\mu^+\mu^-\right)\phi$. Moreover, muons from semi–leptonic b decays provide a tag of the initial state flavour of accompanying neutral B meson. In addition, the study of rare B decays such as the flavour–changing neutral current decay $B_s^0 \to \mu^+\mu^-$ may reveal new physics beyond the Standard Model.
The main requirement for the LHCb muon system is to provide a high–p_T muon trigger at the earliest trigger level (L0). In addition, the muon trigger must unambiguously

identify the bunch crossing, requiring a time resolution better than 25 ns. The heavy–flavour content of triggered events, enhanced by requiring the candidate muons to have high transverse momentum, is utilised also offline, to accurately identify muons reconstructed in the tracking system and to provide a powerful B–meson flavour tag.
The muon system consists of five muon tracking stations, named M1, M2, M3, M4 and M5, placed along the beam axis and interspersed with shields to attenuate hadrons, electrons and photons. The first station is located just downstream RICH2 and before the calorimeters, which constitute the attenuator between M1 and M2. These two stations are the ones used to evaluate p_T for the L0 trigger. The other three stations are positioned after M2 and are interspaced with iron walls 80 cm thick[9].
Stations M2–M5 are constituted of four layers of Multi–Wire Poportional Chambers (MWPC), while the outermost part of M1 has only two MWPC layers in order to reduce the material budget seen by the calorimeters[10]. In the innermost region of the first station, where the particle flux is higher, the MWPC technology is not suitable. Here the Gas Electron Multiplier (GEM) technology is used, in the form of a triple–GEM detector[11],[12].

TRIGGER & DATA STORAGE. The LHCb sub–systems will produce a huge quantity of raw data, which has to be combined and analysed in order to extract the final results. The online analysis in clearly not possible. The adopted strategy is that of a cascade–like system, in which the lower levels operate very fast and rough decisions and pass the selected events to the upper levels. The implemented system consists of two layers.

- Level zero trigger (L0). The lowest level of trigger is completely implemented in custom electronics. The input frequency is 40 MHz, corresponding to the proton–proton bunch crossing, while the output frequency is 1 MHz. It takes data from SPD, PS, ECAL, HCAL and from the muon system and selects events with high p_T. Also the VELO Pile–Up system is considered, in order to reject high–multiplicity events. This rejection assures that the selection is based on b–signatures rather than large combinatories and that the selected events will not occupy a disproportional fraction of the data–flow bandwidth or available processing power in the subsequent trigger level.
- High Level Trigger (HLT). The HLT is a software trigger and it is based on data from all sub–detectors. The input frequency is 1 MHz and the output frequency is 2 kHz[13].

1.2 – THE PARTICLE IDENTIFICATION SYSTEM

In order to obtain precise experimental data on CP–violation in the B system, it is fundamental for LHCb to identify the decay products of b–hadrons. In particular, the ability to distinguish between pions and kaons in a variety of final states is essential for the physics that the experiment is designed to study. Meaningful CP–violation measurements in many important channels are possible only if hadron identification is available. Identifying kaons from the accompanying b–hadron decay in the event also provides a valuable flavour tag. This tag is achieved by identifying kaons from the $b \rightarrow c \rightarrow s$ cascade decay, where the charge of the kaon depends on the charge of the initial b quark. Finally, the particle identification system can complement the calorimeters and the muon system in the identification of electrons and muons.

A clear example of the importance of the particle identification system is the measurement of the CP asymmetry in $B_d^0 \to \pi^+\pi^-$. This measure requires the rejection of other two–body backgrounds with the same topology, such as $B_d^0 \to K^+\pi^-$, $B_s^0 \to K^-\pi^+$ and $B_s^0 \to K^+K^-$. Figure 1.4 (left) shows the reconstructed invariant–mass spectrum without particle identification system. The signal is dwarfed by the backgrounds. Figure 1.4 (right) shows the same reconstructed invariant–mass distribution once the decay products have been correctly identified. The improvement in the signal/background ratio in the selection of the interesting physical channel is clear.

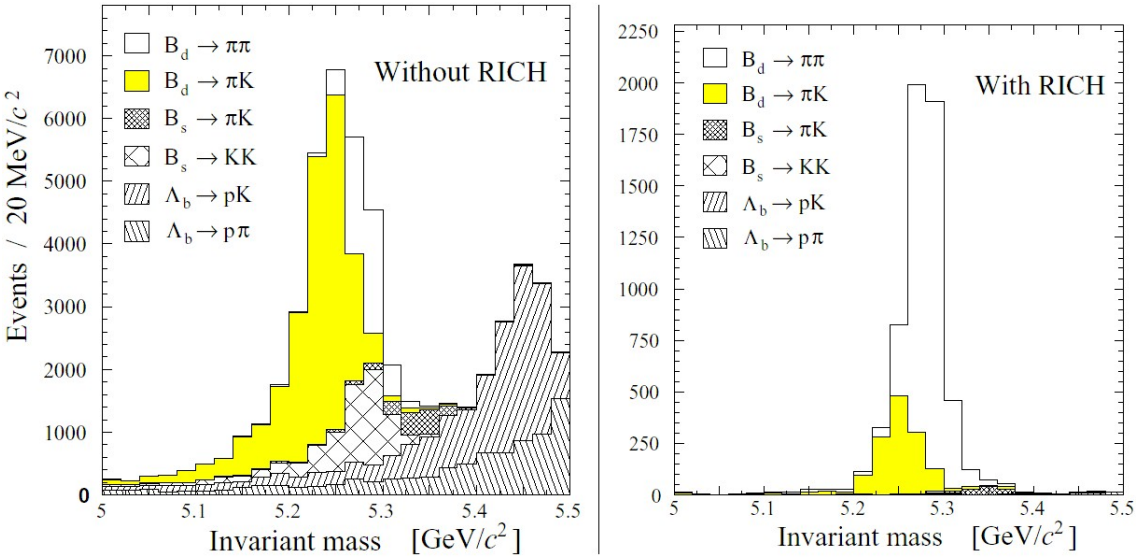

Figure 1.4: reconstructed invariant–mass spectrum for the decay of a B_d into two pions before (left) and after (right) the identification of the final states using the designed LHCb particle identification system.

One of the benchmark channels of LHCb is $B_s^0 \to D_s^{\mp}K^{\pm}$, which will be used to extract the γ angle of the unitarity triangle from a time–dependent fit to the asymmetries. In this case, the branching ratio of the $B_s^0 \to D_s^{\mp}\pi^{\pm}$ decays is about fifteen times more abundant than the channel of interest, as can be seen in Figure 1.5 (left). This would overwhelm the signal if particle identification was not available. Again, a great improvement can be obtained using the designed LHCb particle identification system, as shown in Figure 1.5 (right).

The particle identification system should cover the full angular acceptance of the LHCb spectrometer, from 10 mrad to 300 mrad in the horizontal plane and from 10 mrad to 250 mrad in the vertical plane. The identification of tagging kaons and tracks from high multiplicity decays determines the requirement for the lower momentum limit. Identification down to 1 GeV/c is actually desirable. As regarding the upper limit in momentum required for π–K separation, it corresponds to the momentum carried by the pions in the two–body B decay $B_d^0 \to \pi^+\pi^-$. Simulations show that 90% of such pions have a momentum lower than 150 GeV/c.

The charge of the final states is easily obtainable from the bending direction in the **B** dipole field, but the accurate measurement of the mass is more difficult. The tracking system gives the particles momenta so, if it was possible to measure the particles

velocity in the meanwhile, mass determination would become possible. The only feasible technique that can cover the required momentum range is the detection of Cherenkov photons produced by the passage of charged particles through a radiator. Nevertheless, a single Cherenkov radiator cannot satisfy the requirement of a such large range. The LHCb particle identification system has then been equipped with three different radiators.

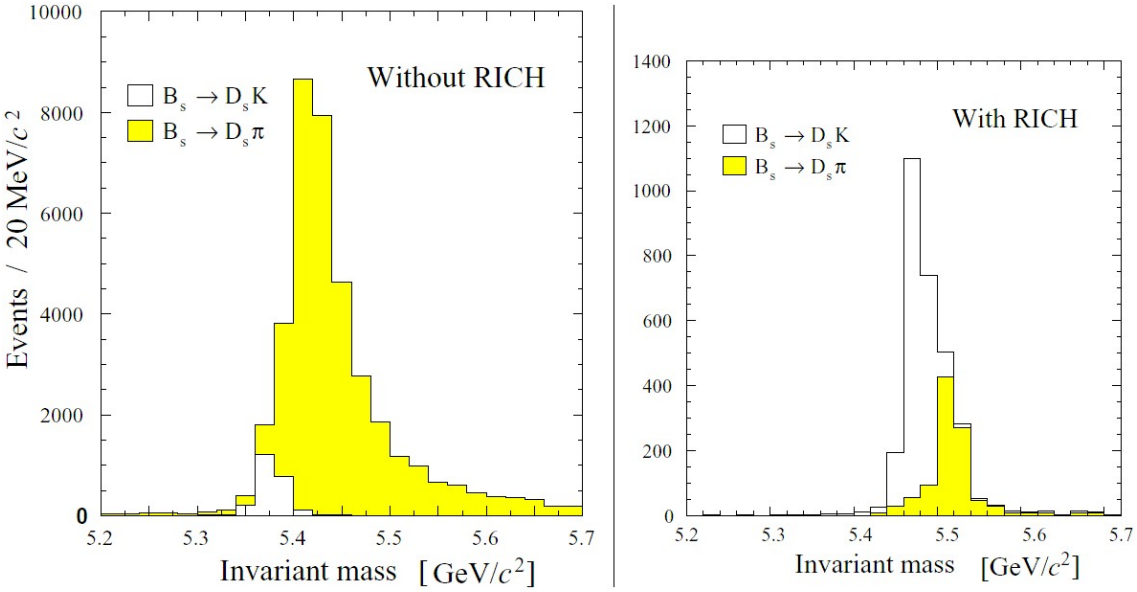

Figure 1.5: reconstructed invariant–mass spectrum for the decay of a B_s into a D_s and a kaon before (left) and after (right) the identification of the final states.

A 5 cm thick aerogel radiator with refractive index n=1.03 is suitable for the lowest momentum tracks. It can provide positive kaon identification above 2 GeV/c and π–K separation up to about 10 GeV/c[14]. The second radiator, used for the intermediate momentum region, is C_4F_{10} gas, which occupies a 85 cm long region along the z axis. Its refractive index is n=1.0014 and it can provide π–K separation up to about 60 GeV/c[10]. Finally, for the highest momentum tracks, gaseous CF_4 is used. It extends for 167 cm, it has a refractive index n=1.0005 and it allows π–K separation up to 150 GeV/c. Table 1.2 summarises the most important properties of the three radiators. Here θ_C^{max} represents the maximum Cherenkov angle, which corresponds to the saturated condition β=1. $\sigma^{tot}(\theta_C)$ is the total error on the reconstructed angle for single photoelectron detection. Finally, $<\#_{pe}/ring>$ is the mean number of detected photoelectrons per Cherenkov ring.

Simulated $b\bar{b}$ events reveal that there is a strong correlation between the polar angle and the momentum of tracks. Figure 1.6 clearly shows that at wide angles the momentum spectrum is softer. The particle identification system has therefore been divided into two detectors, named respectively RICH1 and RICH2. RICH1 is dedicated to the lowest momentum particles, indicatively from 1 GeV/c to 60 GeV/c, and it contains both the aerogel and the C_4F_{10} gas radiators. Its angular acceptance ranges from 25 mrad (25 mrad) to 300 mrad (250 mrad) in the bending (non–bending) plane, being limited internally by the beam pipe size. On the other hand, RICH2 is designed to match the requirements of the highest momentum tracks, up to 150 GeV/c, and it contains the

CF_4 gas radiator. Its angular coverage is limited to the region from 15 mrad (15 mrad) to 120 mrad (100 mrad) in the bending (non–bending) plane[14].

Radiator	Aerogel	C_4F_{10} gas	CF_4 gas
Length [cm]	5	85	167
n (λ=600 nm)	1.03	1.0014	1.0005
θ_C^{max} [mrad]	242	53	32
$\sigma^{tot}(\theta_C)$ [mrad]	2.00	1.45	0.58
<#$_{pe}$/ring>	6.6	32.7	18.4
$p_{thresh}(\pi)$ [GeV/c]	0.6	2.6	4.4
p_{thresh}(K) [GeV/c]	2.0	9.3	15.6

Table 1.2: the most important properties of the three LHCb Cherenkov radiators.

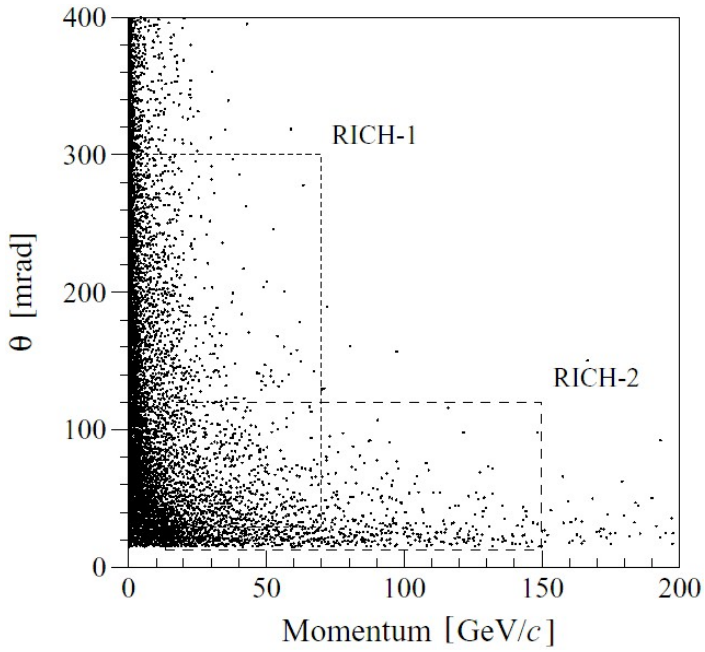

Figure 1.6: polar angle θ versus particle momentum for simulated decays of a B_d into two pions. The regions of interest for RICH1 and RICH2 are indicated by the dashed lines.

RICH1 is required to cover the full LHCb angular acceptance. For this reason, it has been located close to the interaction region, just downstream the vertex locator and before the trigger tracker, in order to catch particles that will be swept out of the spectrometer acceptance by the dipole magnet. A schematic of the RICH1 layout is shown in Figure 1.7 (left). To reduce the material budget, this detector has no entrance window, but it is sealed directly to the VELO tank. The produced Cherenkov photons are reflected by four spherical mirrors with curvature radius of 2400 mm and dimensions of 820 × 600 mm each.

The detectors which use this feature are called Ring Imaging CHerenkov detectors (RICH) and they present two interesting characteristics. First of all, spherical mirrors focus parallel light rays, such as the ones produced in a Cherenkov radiator, to a single

point. The result is that the Cherenkov cone is converted into a circle or an ellipse, depending on the cone axis inclination. Secondly, it is easy to bring the Cherenkov light out of the spectrometer acceptance, simply by tilting the spherical mirrors with respect to the beam axis. This constitutes a great advantage, because it makes possible to place the photodetectors where they don't interact with the tracks of interest.

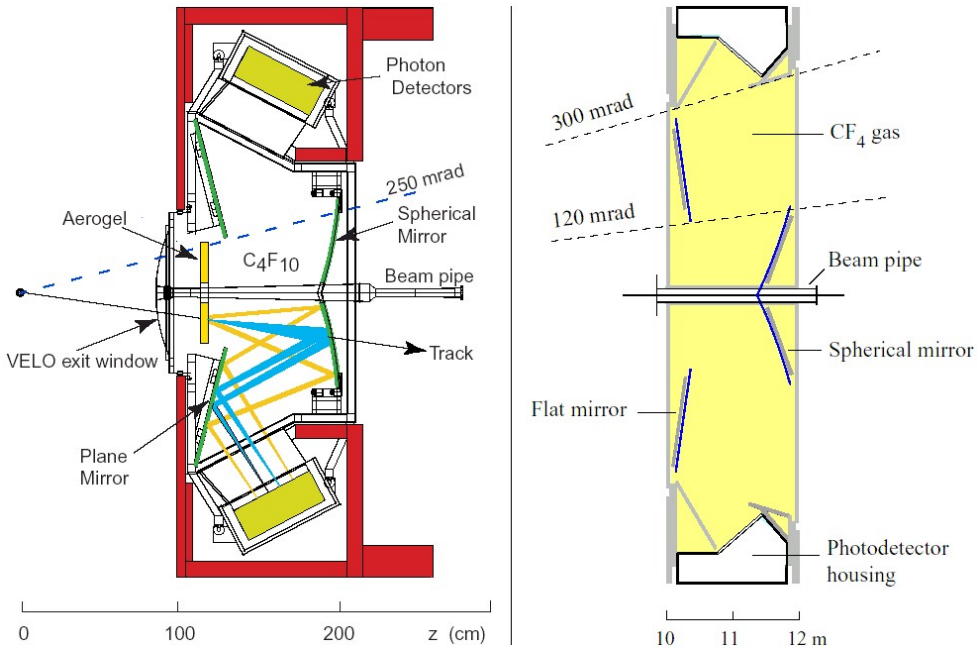

Figure 1.7: layout of the RICH1 detector in the vertical (yz) plane (left) and of the RICH2 detector in the horizontal (xz) plane (right).

In RICH1 the light rays are again reflected using secondary plane mirrors before reaching the photodetectors, so that it is possible to contain the detector length along the beam axis. The RICH1 photodetectors are located above and below the beam, housed in iron shielding boxes which accomplish to a double task. First of all, they are needed to create a zone where the **B** field is attenuated by a factor of about 25, in order to allow operation of the photodetectors. Secondly, they focus the dipole magnet fringe field into the zone of RICH1, where an integrated magnetic field of 0.15 Tm is required between the interaction point and the trigger tracker to determine particles momenta with a resolution of 20–40%[10].

RICH2 is placed 10 m downstream the interaction point, between the last tracking station and the first muon station. Its vessel measures approximately 7 × 7 × 2 m. A schematic of the RICH2 layout is shown in Figure 1.7 (right). The general structure is similar to the one of RICH1, with tilted spherical mirrors, flat mirrors and shielding boxes for the photodetectors, but the overall displacement is horizontal, not vertical as it is in RICH1. In this case the spherical mirror array is made of 56 hexagonal segments inscribed in a circle of 502 mm diameter and with curvature radius of 8000 mm, while the flat mirrors are composed of 40 square segments of 437 × 437 mm[14].

1.3 – THE PHOTODETECTORS

The four photodetector planes of both RICH1 and RICH2 together cover a total area of 2.8 m^2. The photodetectors must be able to detect with high efficiency single Cherenkov photons with wavelength from 200 nm to 600 nm over this large area with a good active–to–total area ratio of about 70%[15]. The spatial granularity of detection is requested to be 2.5 × 2.5 mm, so that the error on the reconstructed Cherenkov angle coming from the spatial uncertainty is comparable with the other error sources. Reducing the pixel size would incur increased cost with little benefit to the Cherenkov angle precision. The photodetectors readout must be fast, compatible with the 25 ns time between LHC bunch crossings and the overall LHCb readout scheme. Finally, the photodetectors will be situated in the fringe field of the dipole magnet and they will experience a radiation dose up to 3 kRad/year.

To satisfy these requirements, a pixel Hybrid PhotoDetector (HPD) has been chosen as the photodetector, its advanced design being carried out in close collaboration with industry. A schematic of the HPD is given in Figure 1.8.

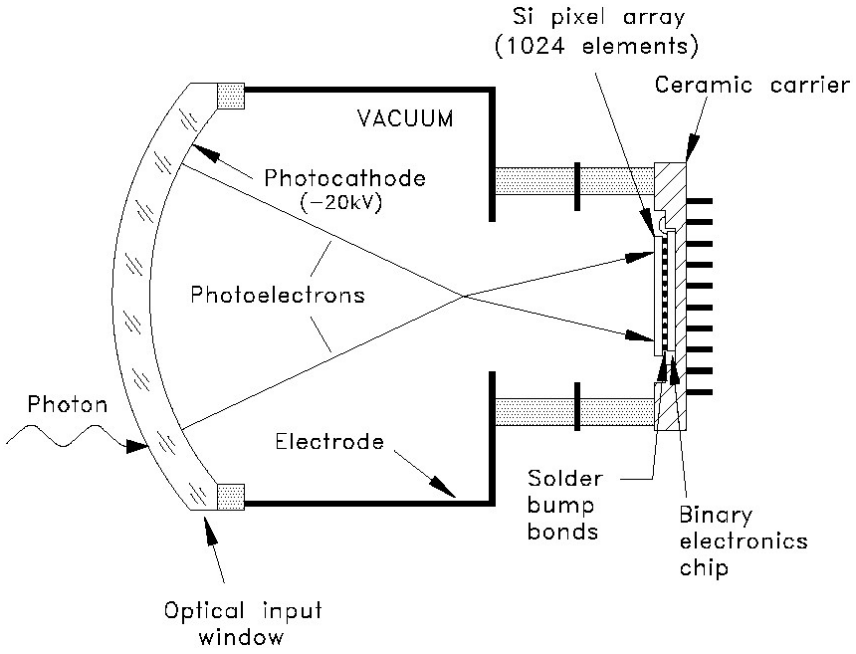

Figure 1.8: schematic of the pixel HPD, illustrating the photoelectron trajectories.

The HPD is an evacuated cylindrical tube with an overall diameter of 83 mm. It has a 7 mm thick, spherical quartz entrance window with a thin layer of S20 multialkali photocathode deposited on its inner surface. This photocathode has a very low photoelectric threshold energy, less than 2 eV, and so it allows detection of low–energy photons, like the ones in the visible spectrum. The measured typical quantum efficiency as a function of the incident photon energy is shown is Figure 1.9[14].

To cover 2.8 m^2 of photodetector planes, 484 HPDs are used. In particular, RICH1 houses 7 columns of 14 tubes each on each photodetector plane (7 columns on A–side and 7 columns on C–side) and RICH2 is equipped with 18 columns of 16 tubes each, equally distributed between A–side and C–side[16]. Inside every photodetector box, the columns are installed in such a way that the HPDs result in a hexagonal close packing configuration, with a inter–axial distance of 87 mm. This kind of packing assures a high

geometrical coverage, about 90.7%. Since the photocathode is sensitive over a 75 mm diameter, the actual active–to–total area ratio is $0.907 \cdot (75/87)^2 = 67.4\%$, which complies to the requested fraction of about 70%.

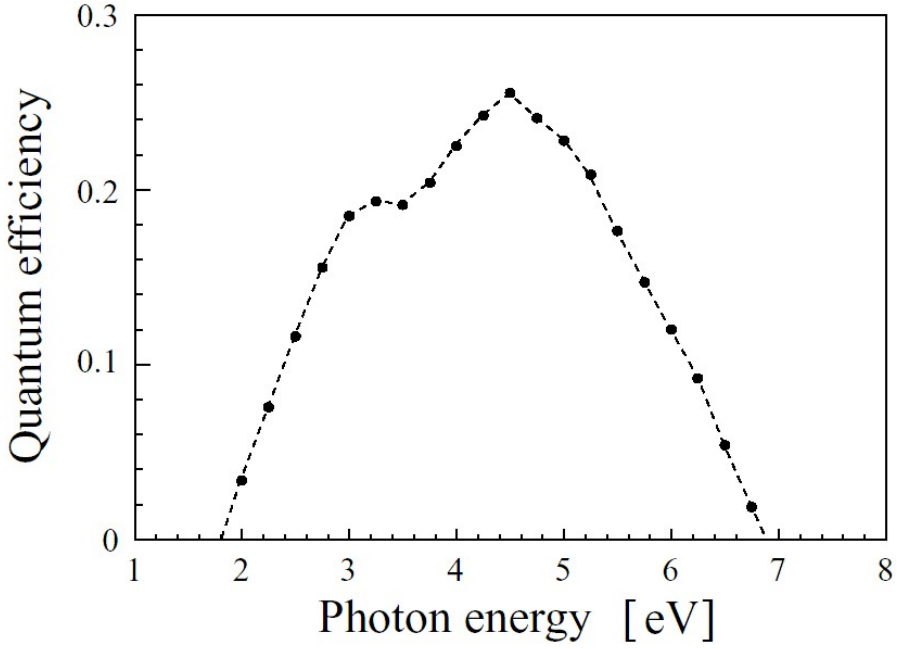

Figure 1.9: photocathode quantum efficiency as a function of incident photon energy, taken from measurements on HPD prototypes with a quartz window.

The HPD uses a static electrical field to accelerate the photoelectrons between the photocathode, kept at –20 kV, and the anode, housed in the basis of the tube and connected to ground. Two intermediate electrodes, at –19.7 kV and –16.4 kV respectively, are used to cross–focus the photoelectrons on the anode and to define the magnification factor, which is fixed to 1/5.

The anode is a silicon detector with active area of 16 × 16 mm, organised as a matrix of 32 × 256 rectangular pixels of 500 × 62.5 μm. This is the anode native spatial granularity, but in the LHCb experiment the pixels are read out eight by eight, as explained below. When a photoelectron hits the anode, a mean charge of 5000 electron–hole pairs is released. Each anodic pixel is a 80 V reverse–biased p–n junction, which is directly bump–bonded to the LHCBPIX1 readout chip. The pixel detector and readout chip assembly is then glued and wire–bonded onto a ceramic carrier before the encapsulation in the vacuum tube.

The LHCBPIX1 readout chips are manufactured in 0.25 μm CMOS technology. They must discriminate single photoelectron hits with high efficiency and time–tag them with the LHC bunch crossing. For these reasons, the signal from every silicon pixel is pre–amplified and then shaped with a shaping time < 25 ns. The obtained signal is discriminated using a global threshold < 2000 e, which can be regulated pixel–by–pixel using a 3–bit fine adjustment. This value of threshold allows detection of single photoelectrons which experience charge sharing among neighbouring pixels. In “Alice mode” each channel is read out separately, while in “LHCb mode” the discriminated signals are ORed eight by eight before the digital processing, thus obtaining a matrix of 32 × 32 super–pixels. A scheme of the encapsulated electronics is shown in Figure 1.10.

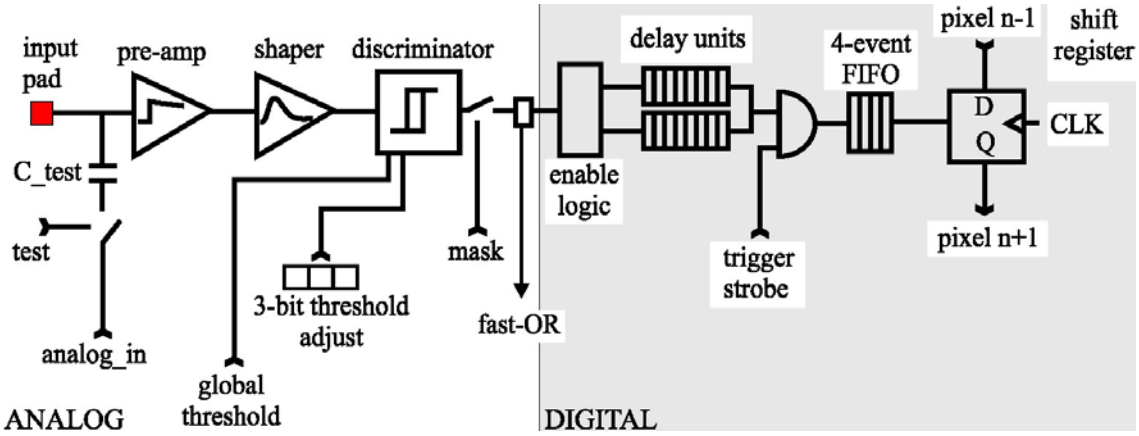

Figure 1.10: schematic of the encapsulated front–end electronics placed in cascade to every HPD pixel.

The LHCBPIX1 chip accepts input data at 40 MHz and provides binary signals with 4 μs latency from each hit pixel, in 32 parallel channels read out at 1 MHz into the on–detector Level–0 adapter module. Every such module services two HPDs and provides a second level of multiplexing so that the data can be read out through optical links into the off–detector Level–1 electronics situated at 100 m distance. The Level–1 electronics removes events rejected by the trigger and derandomizes the data for transport to the DAQ and event building network[14].

The HPD geometry has demonstrated to be very robust against external electric fields, but not against magnetic fields. A **B** field directed like the HPD axis makes photoelectrons move in a helicoidal way and so the resulting anodic image will be deformed. A transverse **B** field can have even worse effects, since it tends to bring photoelectrons out of the anode acceptance. The image seen by the pixel anode shows deformations even with very low magnetic fields, of the order of 1 G, but this distortion can be parameterised and corrected off–line if the field inside the HPD volume is uniform and if its intensity is lower than about 10 G. Figure 1.11 shows the results of experimental tests on non–shielded HPDs. Here the tubes are read out in Alice mode and the colour indicates the number of hits/pixel. The first image on the left shows the test pattern seen by the HPD when no external magnetic field is present. The second image shows how the detected pattern is deformed when the tube is inserted into an axial **B** field of 30 G intensity. In the third picture a 50 G axial field has been used and in the last one a 50 G transverse field has been set.

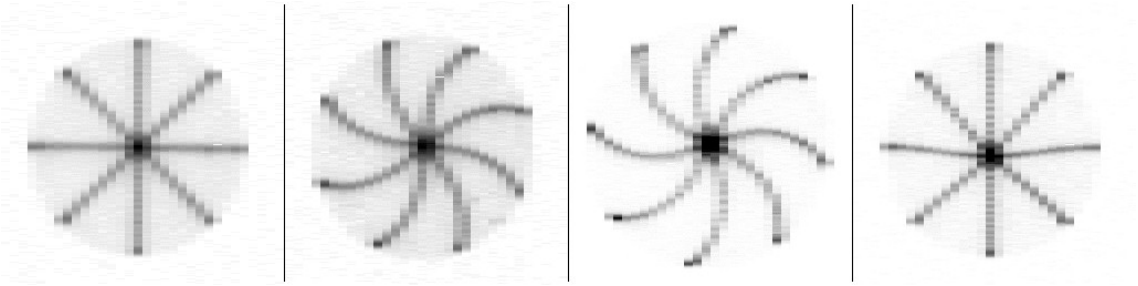

Figure 1.11: HPD image distortion due to an external magnetic field.

In the LHCb experiment the two RICH detectors are placed in zones where the magnetic field is not negligible. In particular, RICH1 is close to the dipole magnet,

while RICH2 is located halfway between the magnet and the big ferromagnetic mass of the hadronic calorimeter. For this reason, the photodetectors need to be shielded. Each HPD matrix is then enclosed into a thick iron shielding box which helps to lower the field inside its volume. Furthermore, every single HPD is laterally surrounded by a local shield consisting of a 0.9 mm thick Mumetal cylinder 140 mm high and with external diameter of 85.8 mm. Mumetal is a magnetic shielding alloy composed by 77% Ni, 14% Fe, 5% Cu and 4% Mo with extremely high magnetic permeability, of the order of $10^5 \div 10^6 \mu_0$. These local shields permit to reduce the field inside the HPDs volume and help to make this fringe field as uniform as possible.

2 – PROJECTORS TESTS

The HPD magnetic shielding system described in the previous chapter will be able to reduce the dipole magnet fringe field and to keep it as uniform as possible inside each HPD. In these conditions, it is possible to parameterise the anodic image distortions and to correct them off–line. In order to carry out the parameterisation, however, it is necessary to know exactly what the actual image deformation is in each of the 484 HPDs mounted on the four RICH photodetector planes. Given the complexity of the system, the only way to get this information is with experimental measurements. The basic idea, then, is to shine a well defined test pattern on the HPDs, one by one or all together, and read out the resulting anodic image when the magnet is off and with different intensities of the magnetic field. The RICH1 and RICH2 groups implemented completely different solutions to do these magnetic distortion tests. All the work described in this thesis has been carried out in the framework of RICH2.
In principle, there are many different possibilities for the light source to be used in shining the test pattern on the HPDs. The solution chosen for RICH2 is to use a commercial light projector (or beamer) with adequate specifications. This idea has some advantages, highlighted here below.

- Modern projectors can be really small and light, therefore easy to handle, to transport and to install. For this reason, there is no need to leave the beamer fixed in the pit environment, but it is possible to bring it inside the RICH2 vessel only once or twice a year, in correspondence to the LHC stops.
- As a consequence of the previous point, the beamer electronics is not requested to be radiation hard. Furthermore, the projector and its support will not contribute to the spectrometer material budget, simply because they will be removed during the LHC runs. Finally, there is freedom of choice for the beamer positioning inside the vessel, since it is not requested to be out of the acceptance.
- Using a projector with adequate angular aperture allows to illuminate all the HPDs in a photodetector plane at one time. So, two light sources are enough to cover RICH2 A–side and C–side. The most external HPDs will have a fraction of the photocathode shaded by the Mumetal shield, but a careful choice of the beamers positions can minimize this effect. The selected positions are symmetrically distributed around the beam pipe, as illustrated in Figure 2.1.
- Figure 2.1 also shows that from these positions it is possible to reach the photodetector planes in two ways. In the first configuration (left) the HPDs are illuminated directly, but not perpendicularly. In the second configuration (right), which can be obtained simply by rotating the beamers, the light rays are

focalised by the spherical mirrors and then reflected on the flat mirrors. The latter method can also constitute a tool to verify the mirrors alignment.

- A projector can be connected to a computer and so it is extremely easy to change the test pattern shape and position inside the beamer acceptance.
- The magnetic distortion apparatus can be also used to periodically monitor the HPDs quantum efficiency. The absolute value of Q.E. is not really important in this context, what is interesting is the eventual Q.E. variation due to radiation damage. This can be done by illuminating the photocathodes with a fixed amount of light and checking what is the mean number of photoelectrons detected. In this measurement, a projector has the great advantage to provide more than one colour, so permitting a Q.E. monitoring at different wavelengths.
- Finally, a commercial beamer has a low cost of a few hundreds euros.

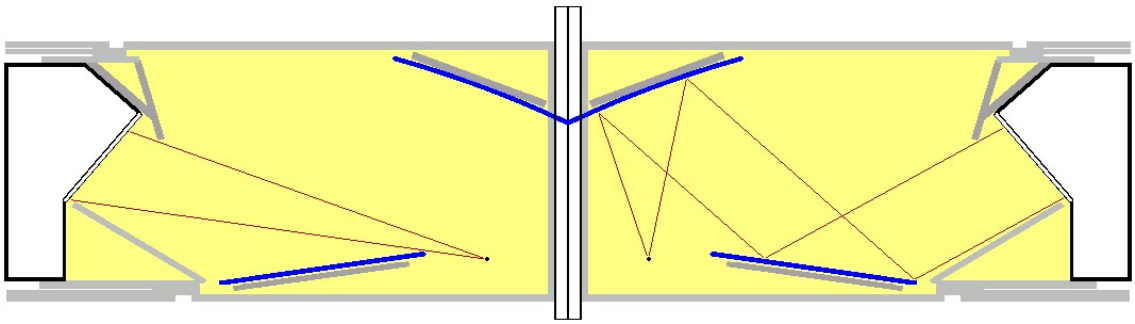

Figure 2.1: selected projectors positions inside the RICH2 vessel. The left and right parts illustrate the two different ways in which the photodetector planes can be reached.

2.1 – THE PHOTO MULTIPLIER TUBES

Six Photo Multiplier Tubes (PMTs) have been inserted in the RICH2 photodetector planes, in the HPD matrices. Three of them are located on A–side, one in the middle of the top, one in the top–external position and one in the bottom–external position, while the other three are located on C–side, in a symmetrical way. Their precise positions have been triangulated with respect to the LHCb coordinate system, so that they can be used as absolute reference points.

These PMTs will have two tasks. First of all, they are used to align the magnetic distortion test pattern. The selected pattern is composed by a matrix of dots for every HPD, each spot corresponding to a beamer pixel, in order to have a good resolution on the dots movements under the external magnetic field. In this pattern there are three bigger spots corresponding to the three PMTs photocathode positions. To align the pattern it is sufficient to move it via software on the computer connected to the beamer, until a maximum in the three PMTs anodic signals is reached. This method allows to align the test pattern with a precision equal to the beamer pixel size. Since the magnetic distortion setup will be also used to periodically monitor the HPDs Q.E., the need for a precise pattern alignment is evident. If the pattern is not correctly positioned, the HPD photocathode can be illuminated by a different quantity of light, so constituting a source of errors in the estimation of the mean number of detected photoelectrons.

The second reason for the presence of the PMTs is strictly connected to the HPD Q.E. monitoring. It is possible, in fact, that the mean number of detected photoelectrons

decreases not for a real HPD Q.E. loss or for a pattern misalignment, but for any other reason connected to the light production or propagation. A fast photodiode placed just in front of the projector can be used to monitor the quantity of emitted light, but it will not be able to monitor any variation in between the light source and the photodetector plane. The PMTs instead, being placed at the same level as the HPDs, can accomplish this task. Unfortunately, the PMTs themselves can undergo a Q.E. loss due to radiation aging. Nevertheless, they have been chosen for some important reasons: they can have an active area large enough to be used as a reference point, they are well known devices and they are not so expensive to make impossible a replacement in case of excessive aging.
The selected PMT model is Hamamatsu H3164–10 photo multiplier tube assembly. It consists of the tube itself and of an external magnetic shielding, for an overall diameter of 10.5 mm. The bialkali photocathode, deposited on a borosilicate glass entrance window, has a diameter of 8 mm and it is sensitive in the wavelength range from 300 nm (4.13 eV) to 650 nm (1,91 eV), with a peak sensitivity at 420 nm (2.95 eV). The photoelectron multiplication chain is based on a linear–focused dynode structure with 8 dynode stages, which can provide a non–saturated gain of 10^6 when operated at the nominal supply voltage of –1250 V. In this way, the cathode typical luminous sensitivity of 100 μA/lm gives an anode sensitivity of 100 A/lm, with a mean anodic dark current of 1 nA after half an hour of operation. As regarding the time response, the typical transit time is 9.0 ns, with a transit time spread of 0.5 ns and a mean rise time of 0.8 ns[17].
An electronic module to read out the RICH2 PMTs and to extract real–time the information about the amount of light that hits each of the six tubes is clearly needed. The purpose of this thesis is exactly to realize such a module. In the rest of this chapter I will explain the Digital Light Processing (DLP) technology, which is the basis of the used projectors, and I will illustrate the results of the tests on two beamers. In the next chapter, I will concentrate on the electronics design, realization and test. Finally, in chapter four I will discuss the feasibility of the HPD Q.E. monitoring and I will estimate the sensitivity of the method.

2.2 – THE DLP TECHNOLOGY

Both the projectors I tested are based on the DLP technology, invented in 1987 by Larry Hornbeck, a scientist of Texas Instruments[18]. Similarly to the Liquid Crystal Display (LCD) projectors, the DLP ones can produce dynamic digital images, but they present some advantages. The operating principle of a DLP beamer is schematically illustrated in Figure 2.2 (left).
The light source is usually a powerful incandescence lamp, surrounded by a parabolic mirror which reflects the rays in the forward direction. These rays traverse a condensing lens and, in correspondence to the focal plane, they encounter a colour filter. The filter basically consists in a fast spinning wheel segmented into three coloured sectors which select the red, green or blue component. The light obtained in this way is not really monochromatic, but it has a spectrum with a typical width of some tens nanometers. Sometimes the wheel has a fourth transparent sector, which helps to regulate the luminosity of the final image, even if it reduces the colour saturation. Furthermore, the most recent models can have more than four colours, including for example the yellow or the violet. The spinning frequency is set equal to the image refresh frequency, so that

for every movie frame a complete sequence of colours is generated. In order to maintain this precise synchronism, a feedback mechanism is requested. For this reason, the wheel rotational velocity is constantly monitored and the supply voltage is real–time adjusted. The final images obtained using the DLP technology present an undesired effect, known as “rainbow effect”: the contours of very contrasted figures appear to be constituted by the wheel primary colours. To reduce this effect, the wheel frequency is usually set to a multiple of the image refresh frequency.

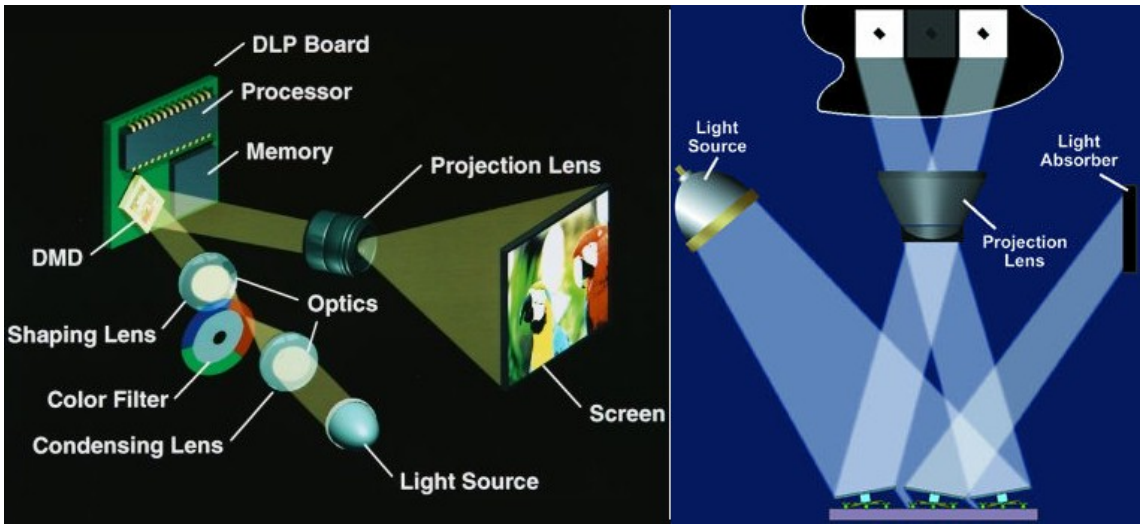

Figure 2.2: operating principle of a DLP beamer (left) and of a DMD (right).

The light exiting the colour filter is directed by a shaping lens onto the surface of the Digital Micro–mirror Device (DMD), which is the very heart of a DLP projector. A DMD is a micro electro–mechanical system constituted by a rectangular matrix of square flat mirrors located on a semiconductor integrated circuit. The whole matrix has an area smaller than one square centimetre and typically includes 800 × 600, 1024 × 768, 1280 × 720 or 1920 × 1080 mirrors. Every mirror can assume two positions with respect to the horizontal plane: depending on the DMD model, it can tilt of ±10° or ±12°. When the mirror forms a positive angle (+10° or +12°) with respect to the flat position, the incident light is reflected towards the projection lens and so the corresponding pixel on the screen is illuminated. On the other hand, when the mirror has a negative inclination (–10° or –12°), the incident light is reflected towards a light absorber placed inside the beamer and so the corresponding pixel appears nearly black. Figure 2.2 (right) shows the operating principle of a one–dimensional 3–pixel DMD.
It is clear that the resolution of the produced image corresponds to the number of pixels in the DMD. This resolution is called “native resolution”. If the video signal sent to the beamer has a resolution equal to the native resolution, no problem arises. Otherwise, a rescaling circuit is enabled, which adapts the video signal resolution to the native one. Since the DLP projectors are digital devices, the rescaling procedure can deteriorate the image quality much more than in an analogical device: if the input resolution is too low, the final image will be pixelised, while if the input resolution is too high, the final image could be distorted.
Figure 2.3 (left) shows an exploded view of a single DMD cell, while Figure 2.3 (right) illustrates a 2–pixel DMD assembly. The micro–mirror is rigidly mounted on the top of

a flipping yoke, which is connected by torsion hinges to two static landing tips. These tips are fixed on the landing site which is just above the integrated circuit and which is used to polarise the micro–mirror and the yoke. The integrated circuit on the basis is a single CMOS SRAM memory cell, constituted by a couple of inverters in cascade. The choice of SRAM memory has been made because it can maintain its binary status until the system is turned off with no need for refresh. The micro–mirror rotation is a consequence of the electrostatic attraction and repulsion between the mirror itself and the two mirror address electrodes and between the yoke and the two yoke address electrodes, which are activated by the SRAM. The mean mechanical commutation time between the +10° and the –10° positions is ~ 15 μs, which corresponds to a mean optical commutation time of ~ 2 μs.

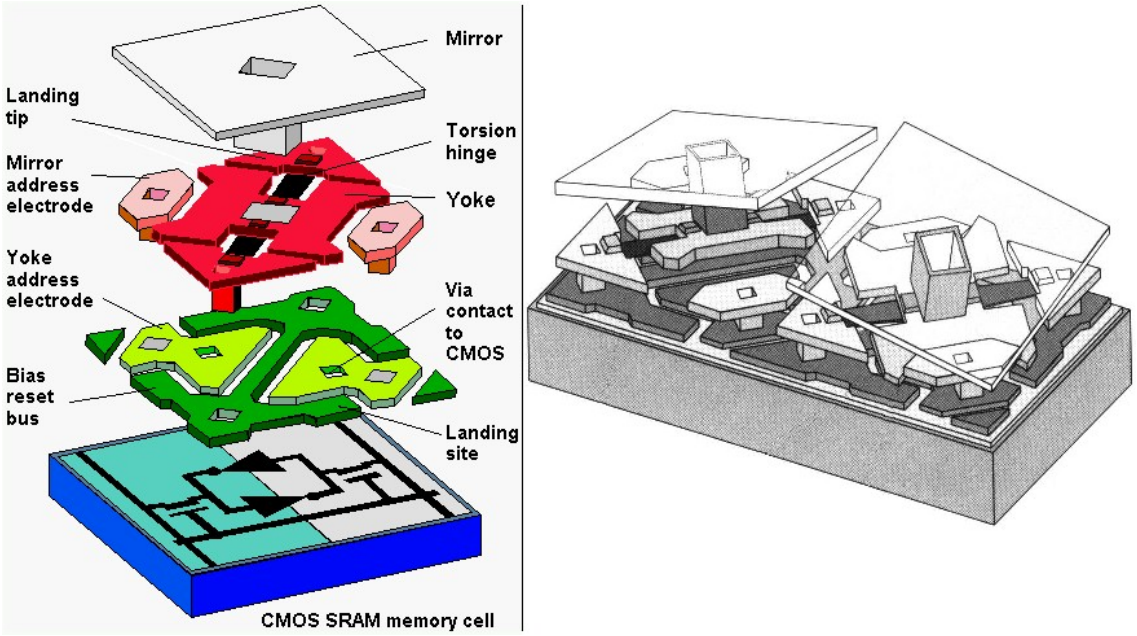

Figure 2.3: exploded view of a single DMD cell (left) and 2–pixel DMD assembly (right).

The DMD memory cells are driven by binary words produced by the DLP chip. This chip analyses the incoming video stream, checks what is the quantity of red, green and blue present in every pixel of each frame and produces digital words proportional to the colour saturation required: the higher is the binary number, the longer is the time the micro–mirror will spend in the projecting position. Since the DLP chip is synchronised with the colour wheel, the pattern produced by the DMD will combine on the screen in such a way to digitally reproduce the incoming video stream. The most common DLP chips use 8–bits words and so they allow to obtain $2^8 = 256$ levels of saturation for each colour. In a DLP projector equipped with a 3–colours wheel, this implies that it is possible to generate $256^3 = 16.8$ millions of colours.
All the digital projectors, both the LCD based and the DLP based, cannot reproduce the true black, but the DLP ones have a better contrast and they are more stable than the LCD ones. For these reasons, the DLP technology has been selected to project the RICH2 magnetic distortion pattern.

2.3 – THE TEST ENVIRONMENT

All the projectors tests described in the rest of this chapter and some of the measurements described in the next two chapters have been carried out in a laboratory located inside building 156, in the CERN Meyrin site. Figure 2.4 (left and right) shows the experimental setup inside this lab.

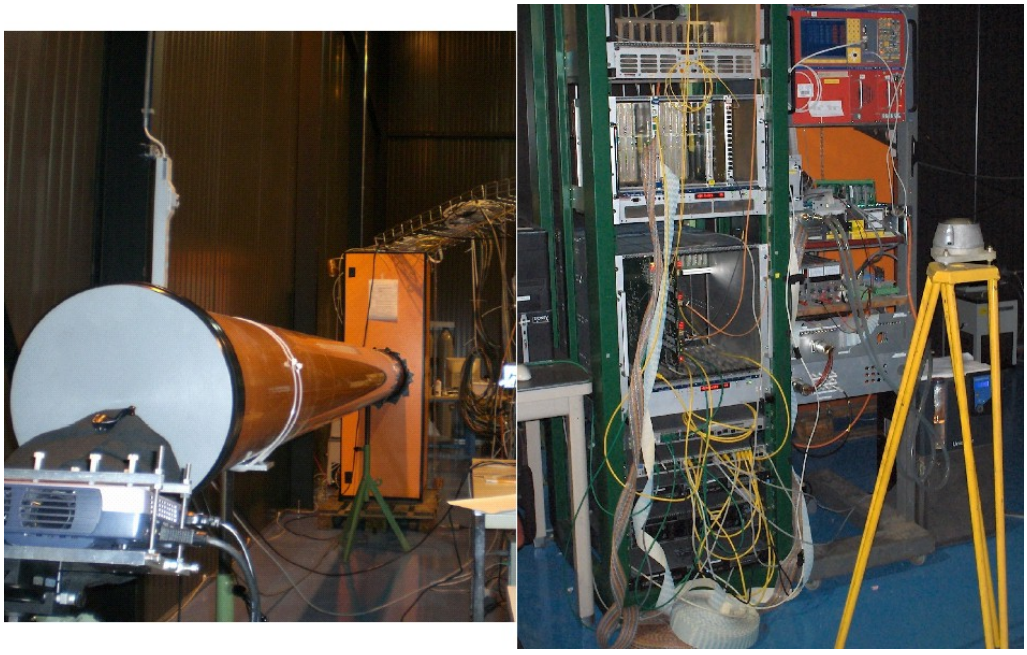

Figure 2.4: experimental setup inside the laboratory 156.

The projector is positioned on a tripod, which also holds an optical filter support. This can contain some Neutral Density (ND) filters, used to reduce the beamer light intensity. Just downstream the filter support, a mechanical shutter mounted at the entrance of a long plastic tube allows to completely shut the light emitted by the projector without turning it off. The plastic tube is used to simulate the space between the beamer and the photodetector plane in the RICH2 vessel. In order to make the tube tight to the external light, it has been covered with a layer of aluminium foils and a layer of black carton (not shown in Figure 2.4). Furthermore, the junctions at the two ends, which are more sensitive to the external light, have been covered with black cloths. The other end of the tube has been connected to a big metal box containing a RICH HPD spare column, including the Level–0 (L0), Low Voltage (LV) and High Voltage (HV) boards. This column has 16 HPDs, but two of them, the fifth and the tenth from the top, experienced problems and so the vacuum tubes have been removed, leaving the pixel chips in their positions.

The described geometry allows to project the attenuated pattern onto the photodetector plane, but not all the HPDs can be reached. The six upper tubes and the six lower ones remain completely shaded, while the tenth tube from the top is partially illuminated, but being one of the pixel chips, doesn't reveal the incident light. As a consequence, only three tubes can give a response to the projector light: the seventh tube from the top (HPD 628) has half the active surface illuminated, while the eighth and the ninth (respectively, HPD 629 and 684), are completely illuminated.

Figure 2.4 (right) shows some of the electronics used to run the HPD column. In the right crate from top to bottom are visible the Silicon bias power supply and the LV power supply with its cooling system. On the other hand, in the left crate are housed the Level–1 (L1) board, the Odin acquisition supervisor board and some of the computers used to control the hardware: the L0 pc, the Embedded Local Monitor Board (ELMB) pc and the event builder pc.
Also two PMTs Hamamatsu H3164–10 have been placed inside the metallic box, in position that can be reached by the projector light. The first PMT, which from now on will be called PMT1, is fixed between HPD 628 and 629, on the side, while the second PMT, called PMT2, is positioned between HPD 629 and 684.

2.4 – THE LAMP PROJECTOR TEST

The first projector which has been tested is a BENQ PB2120 SVGA. In Figure 2.5 the beamer is dismounted and it is possible to distinguish all the parts described in paragraph 2.2.

Figure 2.5: dismounted BENQ PB2120 SVGA DMD DLP lamp projector.

A – The power supply board, which gives AC voltage to the primary lamp and distributes DC voltage to the rest of the projector.
B – The lamp assembly, which includes the powerful lamp, the parabolic mirror and the condensing lens.
C – The lamp housing box.
D – Three fans used to dissipate the intense heat produced by the primary lamp.
E – The coloured wheel, with the return cables for the speed monitoring and regulation.
F – The command buttons on the top panel.
G – The remote sensor.
H – The video decoding board, which digitally processes the incoming video stream and sends data to the DLP board.

I – The DLP board, which accepts data from the video decoding board, checks the level of saturation of each primary colour and commands the DMD.
J – The DMD parallel bus, which interfaces the DLP board with the DMD.
K – The DMD, housed into a block including also the shaping lens.
L – The projection lenses system, with adjustable zoom and focusing.
The first test carried out on this projector is the experimental check of the wheel and DMD timing. The beamer has been mounted on the support shown in Figure 2.4 (left) and its light has been attenuated by a factor of 10^5 using two Kodak ND gelatine filters (F3.00 + F2.00) in order not to damage the photodetectors. The projected pattern was controlled via a computer with video settings corresponding to the beamer's native resolution and colour depth: 800 × 600 pixels, with 16.8 millions of colours and a refresh frequency of 60 Hz. The static image to be drawn on the photodetector plane was generated using Windows Paint and it consists of a 800 × 600 pixels black screen with two coloured squares in correspondence of the PMTs photocathodes. The colours used for the test and the corresponding parameters are reported in Table 2.1.

Colour	Hue	Saturation	Luminosity	Red	Green	Blue
Black	160	0	0	0	0	0
Red	0	240	120	255	0	0
Green	80	240	120	0	255	0
Blue	160	240	120	0	0	255
White	160	0	240	255	255	255

Table 2.1: colour parameters used in the projector timing test.

By changing the squares colour and checking in the meanwhile the resulting PMTs anodic signal with an oscilloscope, it is possible to determine the wheel colour sequence and the wheel and DMD timing. Figure 2.6 shows for example the configuration obtained when PMT1 is illuminated with green light and PMT2 with white light. The results of this test are summarized here below.

- According to the general DLP mechanism explained in paragraph 2.2, the projector light is not emitted continuously in time, but it is compacted in bunches, each bunch corresponding to a colour wheel sector. Inside every bunch the light is quite uniform in time, as can be seen in Figure 2.6.
- The colour wheel has four sectors and it spins with an angular frequency double with respect to the video refresh frequency. In this case, the maximum temporal width of each bunch is $(60\ \text{Hz} \cdot 4 \cdot 2)^{-1} = 2.083$ ms, which is compatible with the bunch length in Figure 2.6.
- The wheel colour sequence is: red, green, white (transparent sector), blue.
- The primary colours used in Paint and listed in Table 2.1 are actually read by the projector as real red, green and blue, respectively. This can be checked observing that only one bunch per colour cycle appears when a primary colour is programmed on the computer.
- The light from the red sector is hardly detectable with the PMTs and with the HPDs (as described subsequently), because the photocathode Q.E. is very low at this wavelength.

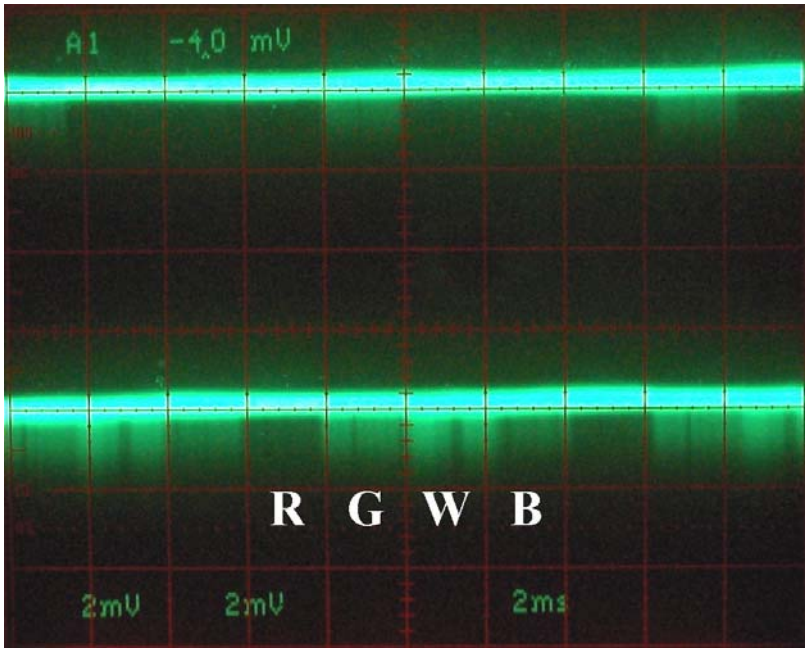

Figure 2.6: anodic signal from PMT1 illuminated by green light (CH1, top) and from PMT2 illuminated by white light (CH2, bottom). The scope is triggering on CH1.

In order to check how the projector behaves when the image colour luminosity is changed, I use patterns with different luminosity and I record what is the bunch length on the scope. This test has been repeated using green and blue, but not with red, because in the latter case the anodic signal is too low. The results are shown in Figure 2.7. Here the errors have been estimated from the bunch width jittering on the scope.

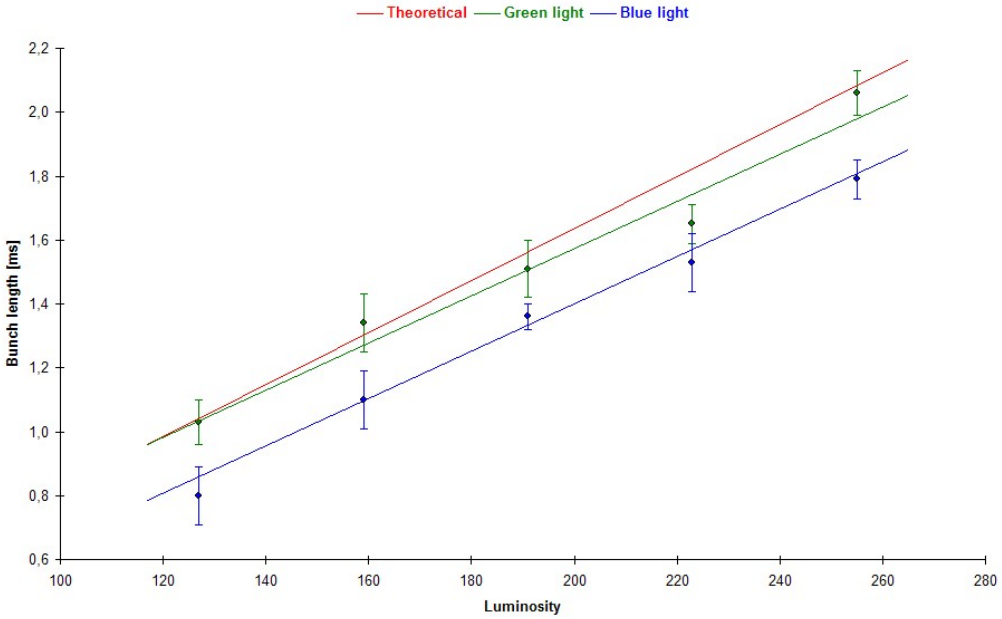

Figure 2.7: theoretical and experimental bunch length of the light emitted by the projector as a function of the image colour luminosity.

When a low–luminosity colour is programmed, the bunch length is reduced, but the number of photons per unit time inside the shorten bunch remains the same. In the previous plot, the "theoretical" line corresponds to what should be observed for each colour in the hypothesis of a colour wheel with equal width sectors, while the "green light" and "blue light" lines are linear fits on the experimental data. Both fits well match the data, with reduced $\chi^2 = 1.44$ for green and reduced $\chi^2 = 0.39$ for blue. The blue data do not match the theoretical prediction, so revealing that the filter wheel has sectors of different length. This fact will be noticed more remarkably in the LED projector and it will be important to keep trace of it in optimising the DAQ software.
Another test has been performed on this projector in order to check what is the obtainable spatial resolution on the HPDs photocathode. The same experimental geometry described above has been used, but now the drawn pattern is a black screen with a grid of green pixels in correspondence of each of the three accessible HPDs. The obtained results show that this resolution is about 2.7 × 2.7 mm. This is a very good result, because it is only slightly larger than the HPD photocathode resolution, which is 2.5 × 2.5 mm. A finest resolution wouldn't increase appreciably the sensitivity on the magnetic distortion measurements.
Tests carried out by other people on the BENQ PB2120 SVGA also show that the light is emitted quite uniformly on the whole screen and that the pixel spatial stability on the screen is good.
Unfortunately, all the DLP lamp projectors are basically affected by two problems. First of all, the incandescence lamp light intensity decreases with time, thus constituting a not ideal light source to be used in quantum efficiency monitoring. Nevertheless, it is possible to compensate for this deviation by measuring the emitted quantity of light with a beam splitter and a photodiode as power meter and then rescaling with consequence the number of detected photoelectrons (in HPDs) or the anodic current (in PMTs).
The second drawback is linked to the fact that the powerful primary lamp dissipates some hundreds Watts and so it needs to be cooled. For this reason, the DLP lamp beamers are usually equipped with some fans which establish a continuous air flow inside the projector, as shown in Figure 2.5. During the magnetic distortion tests, the beamer will be exposed to a not shielded magnetic fringe field which can decrease the fans dissipating power and eventually stop them, with consequent risk of overheating and malfunction. It is important to notice that the colour wheel is not affected by this effect, because it is equipped with a feedback mechanism to control the spinning velocity, while the other fans do not have such a feedback. A shielding box around the projector could help to decrease the field, but it would prevent the air to circulate freely and so it would be necessary a forced cooling system, big and not very practical. The alternative is to use a light source which dissipates a limited amount of energy, as it will be exposed in the next paragraph.

2.5 – THE LED PROJECTOR TEST

It is possible to solve the overheating problem described in paragraph 2.4 by using a LED DLP beamer. This kind of projectors operate in the same way as the lamp DLP beamers illustrated in paragraph 2.2, except for the fact that the optical group constituted by incandescence lamp + parabolic mirror + condensing lens + colour filter + shaping lens is replaced by three coloured LEDs and a shaping prism. The red, green

and blue LEDs are turned on alternatively and they are synchronized with the DMD, so acting as light source and as colour filter at the same time. As a result, the final product turns out to be extremely compact and light and, due to the low LED power consumption, there is no need for cooling fans.
The tested projector is a Mitsubishi PK10. It has a native resolution of 800 × 600 pixels, a depth of 16.8 millions of colours and a contrast of 300:1. During all the tests the image refresh frequency has been set to 60 Hz. The maximum achievable luminosity is much lower than the one of BENQ PB2120 SVGA, but this doesn't constitute a problem, since for our purpose we always need to attenuate the outgoing light. The beamer optics offers a manual regulation for the focus, but no zoom is available. The overall dimensions are 97 × 123 × 47 mm, the weight is 450 g and the total power consumption is only 17 W[19].
Similarly to what has been done for BENQ PB2120 SVGA, the first test carried out on the Mitsubishi PK10 is the experimental check of the LEDs and DMD timing. The followed procedure is nearly the same described in the previous paragraph, with some slight differences. Since the light emitted by the LEDs is much less intense than the one produced by the lamp, it is necessary to reduce the attenuation by a factor of 100 in order to see a clear signal on the oscilloscope: a Kodak ND gelatine filter with attenuation 10^3 (F3.00) has been positioned in front of the projector. The computer connected to the beamer has then been used to draw a 800 × 600 pixels, 16.8 millions of colours, static black screen with coloured squares in correspondence of the two PMTs photocathode. The used colours are listed in Table 2.1. The obtained results are summarized here below.

- As usual in DLP projectors, the light is emitted in bunches. The temporal width of a bunch is proportional to the colour luminosity, but the light emitted per unit time inside a single bunch is a fixed value for each primary colour.
- Three primary colours are present, corresponding to the three LEDs. The colour cycle frequency is four times higher than the image refresh frequency and so the colour cycle length is $(60\ \text{Hz} \cdot 4)^{-1} = 4.167$ ms.
- The colour sequence and the maximum bunch length for each colour are: red (907 ± 3 μs), green (2497 ± 5 μs), blue (754 ± 3 μs). The measured colour cycle length 4158 ± 7 μs thus agrees with the value calculated in the previous point.
- The Windows Paint primary colours correspond to the beamer's LEDs colours.

As regarding the obtainable spatial resolution on the HPDs photocathode, a test similar to the one carried out on BENQ PB2120 SVGA has been executed on this projector. Now the resolution is about 3.9 × 3.9 mm, which is much bigger than the photocathode resolution, 2.5 × 2.5 mm.
Summarizing, this DLP LED beamer has demonstrated to be a very interesting device to be used as the pattern source in the RICH2 magnetic distortion tests and in the RICH2 HPDs quantum efficiency monitoring. It is small and light, not very sensitive to external magnetic fields and its low luminosity doesn't constitute a problem. The only inconvenient is the absence of a zoom system which could help to reduce the pixel size on the photodetector planes. Anyway, by now the Mitsubishi PK10 is the best available choice.
Since no DLP LED projector with zoom is available on the market, the most promising idea for a future upgrade is the realization of a custom DLP beamer which shares the advantages of a LED light source and of a zoom lenses system. This can be done basically in two ways. The first possibility is to find an appropriate zoom system which

can be positioned just downstream the Mitsubishi PK10. The second and more interesting idea is to modify a standard DLP lamp beamer replacing the primary lamp, the condensing lens and the colour filter with a set of LEDs. These LEDs should be supplied with an external power source and they could be placed inside the lamp housing box or they could be kept externally, their light reaching the DMD via optical fibres. In this way it is possible to draw a monochromatic image with no need to synchronize the selected LED with the DMD: it is sufficient to keep the LED always on and to program on the computer a monochromatic pattern, the DMD will do the rest. Furthermore, using different LEDs, it is possible to scan the Q.E. at many different wavelengths, even in the UV region, where most of the Cherenkov light is emitted. In all this, the main problem is to find a way to illuminate uniformly the DMD, in order to obtain a image with homogeneous luminosity from the centre to the border.

3 – ELECTRONICS DESIGN AND TEST

In order to properly design the RICH2 6 PMTs readout electronics, it is necessary to keep in mind the tasks these photodetectors have to accomplish. As it was fully explained in paragraph 2.1, the PMTs will be used to accurately align the magnetic distortion test pattern and they will constitute a helpful tool during the HPDs quantum efficiency monitoring. As a consequence, six independent readout electronics channels are needed, each of them being asked to give an output signal proportional to the anodic charge released per unit time by the corresponding PMT. This basically means that every channel has to work as an integrator. Furthermore, it is of primary importance to consider what is the expected shape of the anodic signals. Because of the choice of the DLP technology for the projector, the light will arrive on the PMTs photocathode compacted in bunches of about 1 μs temporal width and so the resulting anodic signal will look like the one shown in Figure 2.6 (top).
The choice made is to use six custom–made shaper amplifiers, with adequate integration and differentiation time. The inclusion of a differentiator will accomplish to a double task. First of all, an appropriate decay constant allows to re–establish the baseline before the next bunch enters the shaper. Secondly, it will work as a high–pass filter, so allowing to cut the undesired incoming low–frequency noises, typically the 50 Hz and its first harmonics.

3.1 – CHOICE OF THE SHAPING TIMES

Before designing the electronics prototype, it can be useful to calculate from a theoretical point of view what are the integrator and differentiator shaping times which give the best Signal/Noise ratio (S/N). In order to do this, consider the simple filter shown in Figure 3.1 and define $R_1 \cdot C_1 = \tau_H$, the high–pass filter characteristic time constant, and $R_2 \cdot C_2 = \tau_L$, the low–pass filter characteristic time constant.

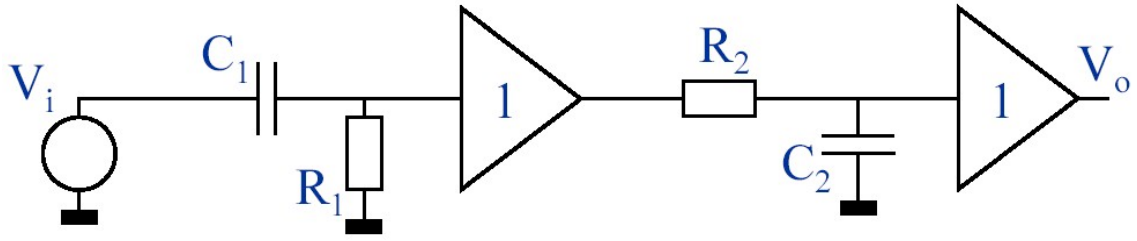

Figure 3.1: schematic of the simplified filter used to build a model for the S/N evaluation.

V_i is a typical PMT anodic signal, similar to the one shown in Figure 2.6 (top). Given the high light attenuation, this corresponds to the tube response to single photons in the visible spectrum: the obtained signal is constituted by a series of closely packed pulses of comparable amplitude, with mean width of about 1 ns and with inter–arrive time distributed according to a Poisson statistics with mean value of about 100 MHz. However, it is not possible to keep trace of a so complex signal in the theoretical computation. For this reason, V_i will be approximated with its envelope, which means a square pulse of temporal width *T* and defined amplitude, set for simplicity to 1.
As regarding the noise superimposed to the signal, from what has been observed testing the two projectors, it is realistic to suppose that the main component is the 50 Hz one.
The last simplification introduced in the model regards the bounds for τ_L and τ_H. First of all, τ_L has to be lower than τ_H to have a band of frequencies with zero attenuation. Furthermore, both the time constants have to be lower than *T* to avoid pile–up between signals relative to successive photon bunches. All this can be summarized in the condition $\tau_L < \tau_H << T$.
Let's start calculating the transfer function of the circuit in Figure 3.1 in the domain of the complex frequency s:

$$V_o(s) = \frac{s\tau_H}{1+s\tau_H}\frac{1}{1+s\tau_L}V_i(s)$$

Since the Laplace transform of the square pulse $V_i(t) = 1(t) - 1(t-T)$ is:

$$V_i(s) = \frac{1-e^{-sT}}{s}$$

the convolution in the domain of the complex frequency results:

$$V_o(s) = \frac{\tau_H}{\tau_H - \tau_L}\left[\frac{1}{s+1/\tau_H} - \frac{1}{s+1/\tau_L}\right]\left[1-e^{-sT}\right] \qquad V_o(s) = \frac{1}{\tau\left[s+1/\tau\right]^2}\left[1-e^{-sT}\right]$$

where the expression on the left is valid for $\tau_L \neq \tau_H$, while the expression on the right is valid for $\tau_L = \tau_H = \tau$. Applying an inverse Laplace transform, it is possible to obtain the shaped signal $V_o(t)$ in the two cases:

$$V_o(t) = \frac{\tau_H}{\tau_H - \tau_L}\left[e^{-t/\tau_H} - e^{-t/\tau_L}\right]1(t) * \left[\delta(t) - \delta(t-T)\right] \qquad V_o(t) = \left[\frac{t}{\tau}e^{-t/\tau}\right]1(t) * \left[\delta(t) - \delta(t-T)\right]$$

where * denotes a convolution. These expressions have a maximum at time $t = t_{max}$:

$$t_{max} = \frac{\tau_H\tau_L}{\tau_H - \tau_L}\ln\left(\frac{\tau_H}{\tau_L}\right) \qquad t_{max} = \tau$$

The maximum of the output signal $S = V_o^2(t_{max})$ is then:

$$S = \left[\frac{\tau_L}{\tau_H}\right]^{2\tau_L/[\tau_H - \tau_L]} \qquad S = \frac{1}{e^2}$$

As regarding the 50 Hz noise, its variance N at the filter output can be calculated as:

$$N = \frac{1}{2\pi}\int_{-\infty}^{+\infty}\left|H(j\omega)\right|^2 N(\omega)d\omega = \frac{\omega_0^2\tau_H^2}{1+\omega_0^2\tau_H^2}\frac{1}{1+\omega_0^2\tau_L^2}$$

where $\omega_0 = 2\pi f_0 = 100\pi$ rad/s. The S/N analytical expression finally results:

$$\frac{S}{N} = \frac{\left[1+\omega_0^2\tau_H^2\right]\left[1+\omega_0^2\tau_L^2\right]}{\omega_0^2\tau_H^2}\left[\frac{\tau_L}{\tau_H}\right]^{2\tau_L/[\tau_H - \tau_L]} \qquad \frac{S}{N} = \frac{\left[1+\omega_0^2\tau^2\right]^2}{\omega_0^2\tau^2 e^2}$$

Figure 3.2 (top) shows a 3D plot of this function where the free parameters τ_L and τ_H vary from 0 to 25 ms, which correspond to cut frequencies from ∞ down to 40 rad/s.

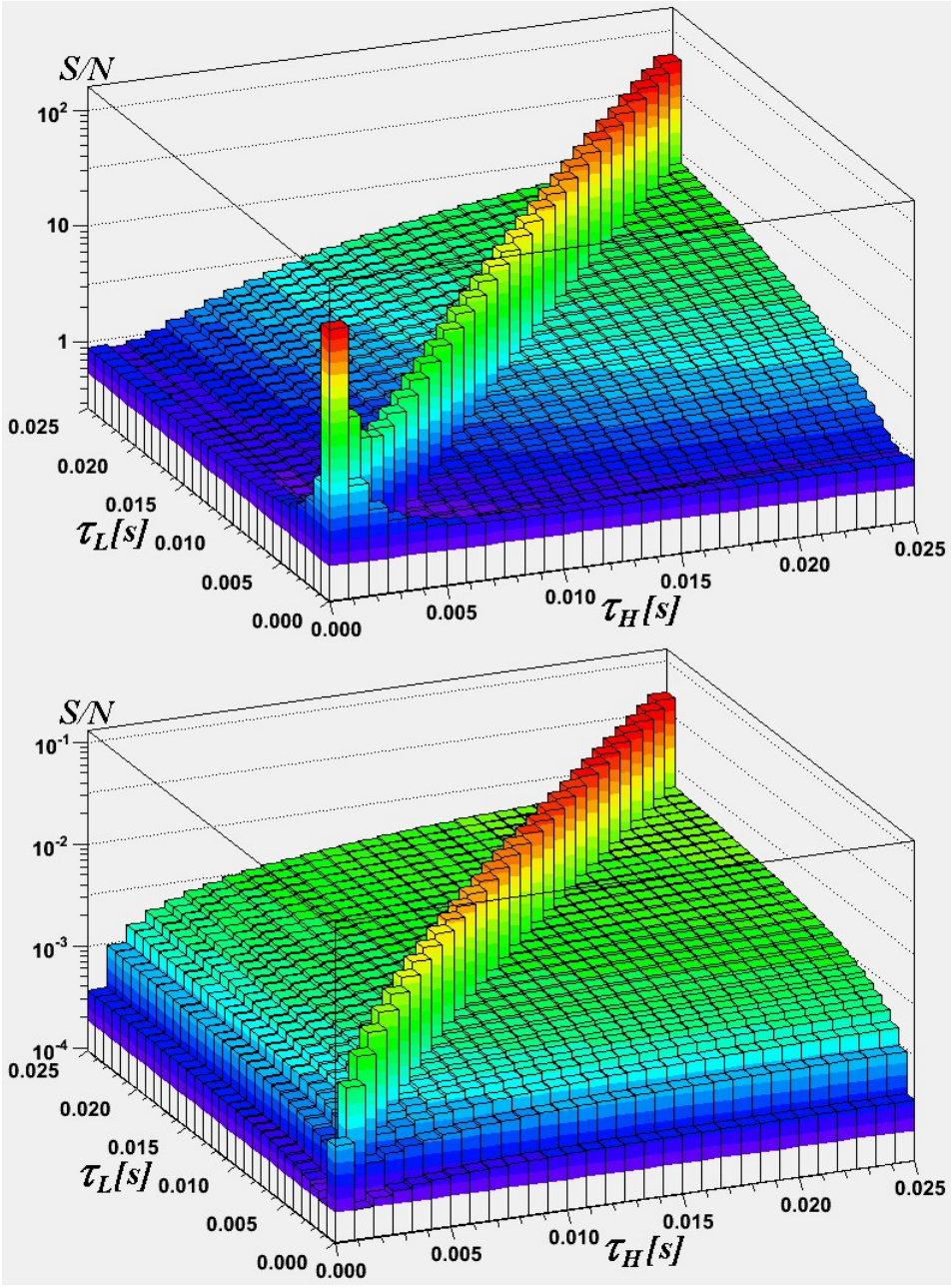

Figure 3.2: logarithmic S/N as a function of τ_L and τ_H. In the upper plot the noise has only one component at 50 Hz, while in the lower graph there is an hergodic homogeneous white noise superimposed on the 50 Hz main line.

The plot clearly shows two zones of the τ_L–τ_H space with particularly good S/N.

- When the two shaping times approach zero, the filter cut frequencies tend to infinite, so excluding completely the 50 Hz noise. Considering the formula of S/N for $\tau_L = \tau_H = \tau$, it is easy to notice that for small values of the shaping times the S/N ratio increases like τ^{-2}.

- When $\tau_L \approx \tau_H$ only a narrow band of frequencies passes through the filter with low attenuation, so giving a high S/N. This is not true in proximity of the noise frequency, because in this case the undesired component is not filtered: at $\tau_L \approx \tau_H \approx 3$ ms the plot has a minimum. From the analytical expression above, for large values of the shaping times the S/N ratio increases like τ^2.

In this model, the use of a simple CR–RC and the hypothesis $\tau_L < \tau_H << T$ do not affect appreciably the qualitative behaviour of S/N. The most important approximations, in fact, have been introduced considering the input signal as a square pulse and using a simple 50 Hz input noise source. It is possible to release the last bound and to consider an hergodic homogeneous white noise superimposed on the 50 Hz one. Repeating the computation, it is possible to obtain a new S/N formula, which behaviour is summarized in Figure 3.2 (bottom). Now the peak at $\tau_L \approx \tau_H \approx 0$ has disappeared, while at large values of $\tau_L \approx \tau_H$ the S/N ratio increases like τ and not like τ^2. In conclusion, this preliminary analysis tells us that it is good to choose the largest shaping times possible in such a way what $\tau_L \approx \tau_H$.

Switching from the model to the choice of the shaping times for the real circuit, there are some additional conditions to keep in mind. The most important of them are listed below.

- The integrator characteristic time τ_L has to be set as large as possible not only for the reasons just explained, but also on a statistical basis. The real input signal is composed by closely packed narrow pulses of comparable amplitude, with inter–arrive time distributed according to a Poisson statistics with mean value ν_0 of about 100 MHz. As a consequence, the integration process can be also seen as the count of the number of pulses during the integration time, which corresponds to k times τ_L. Setting the mean inter–arrive time $t_0 = \nu_0^{-1}$, the actual number n of collected pulses during $k \cdot \tau_L$ will be distributed according to:

$$P_{(k\tau_L/t_0)}(n) = \frac{(k\tau_L/t_0)^n}{n!} e^{-(k\tau_L/t_0)}$$

  with a mean value $\bar{n} = k\tau_L/t_0$ and a variance $\sigma_n^2 = k\tau_L/t_0$. The statistical error introduced in the integration process thus will be $\sigma_n/n = \sqrt{t_0/k\tau_L}$. Since t_0 is fixed by the experimental setup and cannot be decreased for safety reasons and k is a constant, the only way to obtain a lower error is to increase τ_L.
- τ_L has to be much lower than the projector's photon bunch duration for the shaper to work properly and τ_H has to be much lower than the blank space between one bunch and the other in order to re–establish the baseline before the next bunch enters the shaper. Since the selected beamer is the DLP LED Mitsubishi PK10, the minimum full–length bunch width is 754 ± 3 μs (for blue light) and the minimum inter–bunch time is 1670 ± 5 μs (for green light). The conditions to impose are then $\tau_L << 754 \pm 3$ μs and $\tau_H << 1670 \pm 5$ μs.
- Actually, there is another constraint on the integrator characteristic time upper value, which is even more stringent than the one exposed in the previous point. Looking carefully at the PMTs anodic signals obtained using either the lamp or the LED beamer, in fact, it is possible to notice that there are a few blank spaces inside the photon bunches. The positions of these blanks are not random, but they repeat according to a periodic sequence over several bunches. This is clearly a phenomenon linked to the DMD which cannot be controlled if not reprogramming the DLP chip. As it will be shown in paragraph 3.4, these blanks

cause spikes on the output signal which prevent from correctly evaluating the peak value. It is then necessary to keep τ_L much lower than the time period between the beginning of the bunch and the first blank space.

- At last, it can be useful to consider how the output signal peak value will be found. The chosen technique is to connect a digitiser at the shaper output and to sample the signal. To obtain a good result with a reasonable sampling frequency, it is necessary once again to keep τ_L and τ_H as large as possible.

3.2 – PROTOTYPE DESIGN AND PRELIMINARY TEST

On the basis of the theoretical results and of the experimental observations described in the last paragraph, a prototype single–channel shaper amplifier electronics board has been designed. Figure 3.3 shows the schematic of this prototype, which is basically constituted by four stages in cascade.

The first stage is a differential amplifier with 50 Ω terminations on both the inputs. First of all, this stage can be used for noise subtraction in case an external spare cable is available. Secondly, since the second and fourth stages require fixed and small gains, this stage allows to split the required large total gain of the order of 10^2 between the first and third stage, thus avoiding a big reduction in the operational amplifiers bandwidth. In particular, the gain of this stage has been set to 20.

The second stage is a two–pole high–pass active Bessel filter, which has a roll–off of 40 dB/dec, so allowing to improve further the S/N ratio. The filter characteristic time constant is $\tau_H = 100\ \text{nF} \cdot 3.3\ \text{k}\Omega = 330\ \mu\text{s}$, which corresponds to a cut frequency of 3.86 krad/s or, equivalently, 614 Hz. This assures a 50 Hz suppression by a factor ≈ 151. The stage gain is fixed by the Bessel equations and corresponds to 1.267, while the values of R_8 and R_9 have been fixed equal to $R_{10} \parallel (R_{11} + R_{12})$ in order to minimize the stage output voltage offset.

The third stage is a passive low–pass filter with characteristic time constant $\tau_L = 47\ \text{nF} \cdot 1\ \text{k}\Omega = 47\ \mu\text{s}$, which corresponds to a cut frequency of 21.3 krad/s or, equivalently, 3.39 kHz. The passive integrator is followed by the main amplification stage, which gain can be regulated from 11 to 61 via an external potentiometer.

The fourth and last stage is a simple inverter with unitary gain, which can be used to obtain a differential output.

Given the circuit schematic, it is possible to calculate from a theoretical point of view the expected waveform analytical expression at the output of the third stage. The signal at the output of the fourth stage will be the same, except for a minus sign. To carry out the computation, consider as input signal on IN_+ the square pulse $V_i(t) = V_A[1(t) - 1(t-T)]$, where V_A is a negative number corresponding to the anodic pulses envelope amplitude and T is the photon bunch temporal width. The other input IN_- will be connected to ground via R_{21}. Let's define $G_1 = 20$, $G_2 = 1.267$ and $G_3 = 11$ to 61 the gain of the first, second and third stage, respectively, and define $\tau_H = R_8 \cdot C_9 = R_9 \cdot C_7$ the high–pass filter characteristic time constant and $\tau_L = R_2 \cdot C_2$ the low–pass filter characteristic time constant. The transfer functions of the three stages in the domain of the complex frequency s are:

$$H_1(s) = G_1$$

$$H_2(s) = \frac{s^2\tau_H^2}{1 + s[3 - G_2]\tau_H + s^2\tau_H^2} G_2$$

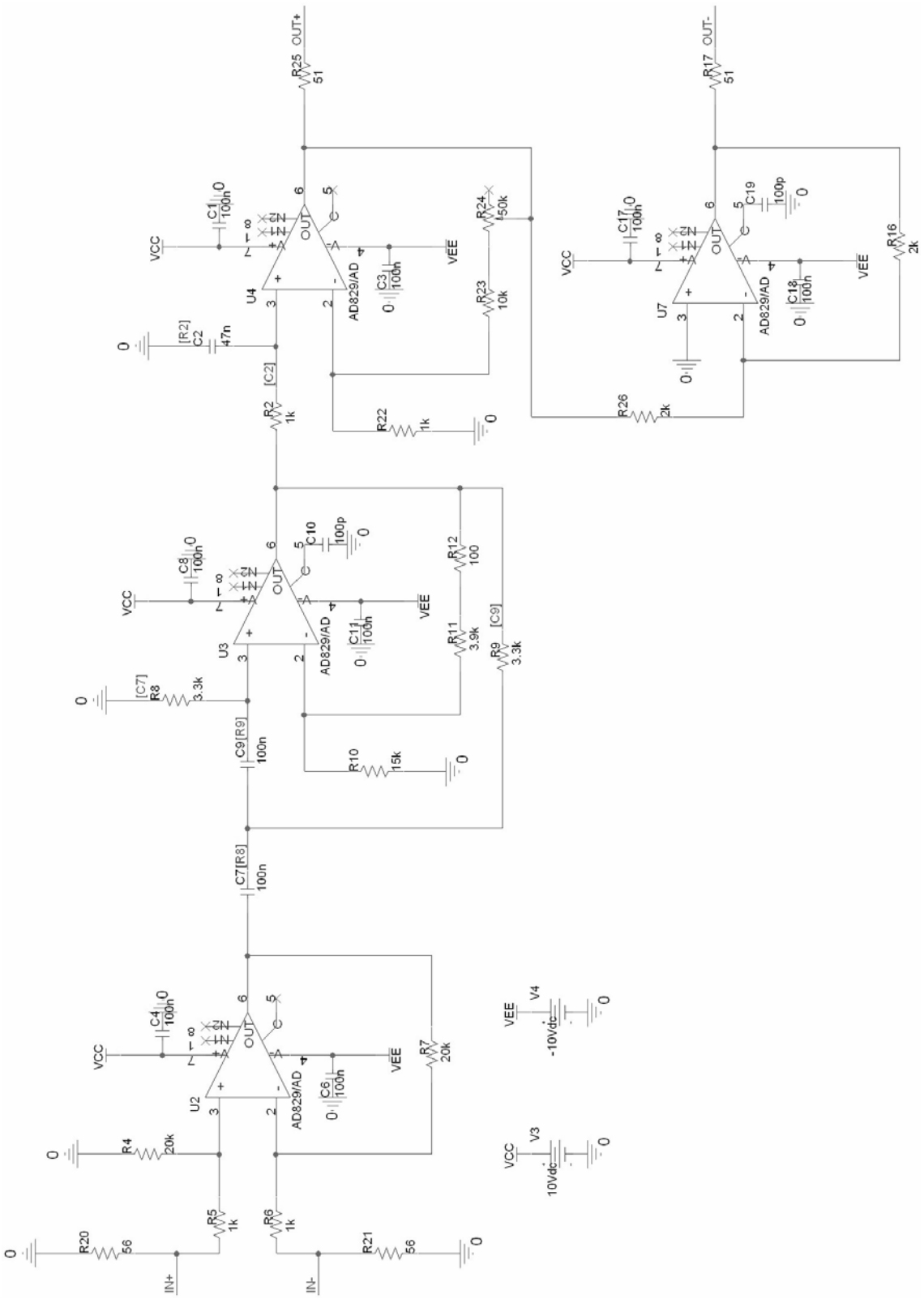

Figure 3.3: schematic of the single–channel shaper amplifier prototype.

$$H_3(s) = \frac{1}{1 + s\tau_L} G_3$$

Since the Laplace transform of the square pulse $V_i(t) = V_A[1(t) - 1(t-T)]$ is:

$$V_i(s) = \frac{1 - e^{-sT}}{s} V_A$$

the convolution in the domain of the complex frequency results:

$$V_o(s) = \left[\frac{A}{s - M_+/\tau_H} + \frac{\overline{A}}{s - M_-/\tau_H} + \frac{B}{s + 1/\tau_L} \right] \left[1 - e^{-sT}\right] G_1 G_2 G_3 V_A$$

$$A = \frac{M_+ \tau_H}{\left[\tau_H + M_+ \tau_L\right]\left[M_+ - M_-\right]}$$

$$B = \frac{-\tau_H^2}{\left[\tau_H + M_+ \tau_L\right]\left[\tau_H + M_- \tau_L\right]}$$

$M_\pm/\tau_H = [a \pm ib]/\tau_H$ being the two complex coniugated poles of the Bessel filter, with $a \approx -0.867$ and $b \approx 0.499$. Applying an inverse Laplace transform, it is possible to obtain the shaped signal $V_o(t)$ at the output of the third stage:

$$V_o(t) = \left[2|A| e^{at/\tau_H} \cos\left(\frac{bt}{\tau_H} + \beta \right) + Be^{-t/\tau_L} \right] 1(t) * [\delta(t) - \delta(t-T)] G_1 G_2 G_3 V_A + baseline$$

$$2|A| = \frac{\tau_H}{b\sqrt{\tau_H^2 + \tau_L^2 + 2a\tau_H\tau_L}}$$

$$B = \frac{-\tau_H^2}{\tau_H^2 + \tau_L^2 + 2a\tau_H\tau_L}$$

$$\beta = \arctan\left(-\frac{a\tau_H + \tau_L}{b\tau_H} \right)$$

Figure 3.4 shows a plot of $V_o(t)$ when the shaping times assume the values τ_L = 47 μs, τ_H = 330 μs and when the square pulse temporal width is set equal to $T = (960\ \text{Hz})^{-1} \approx$ 1.04 ms. Since the used shaper is basically a CR^2–RC^n, the obtained waveform is composed by the superimposition of two reversed bipolar signals, the first in correspondence of the square pulse descending edge and the second in correspondence of the rising edge. The plot also shows that it takes about 2 ms from the end of the square wave to completely re–establish the baseline on a zero–value.

The prototype shaper amplifier electronics board actually realized is shown in Figure 3.5, fixed on the basis of a metallic box in order to shield it from external electromagnetic fields. The resistors and the capacitors are soldered on the back side, not visible in the picture. The labels highlight the most important parts.

A – The 9–pin "D" connector for power supply.

B – The on–board power supply connector.

C – The non–isolated BNC connector for the non–inverting differential input.

D – The non–isolated BNC connector for the inverting differential input.

E, F, G, J – The OP–AMPs of the first, second, third and fourth stage, respectively.

H – The externally settable potentiometer of the main amplification stage.

I – The non–isolated BNC connector for the third stage output, OUT_+.

K – The non–isolated BNC connector for the fourth stage output, OUT_-.

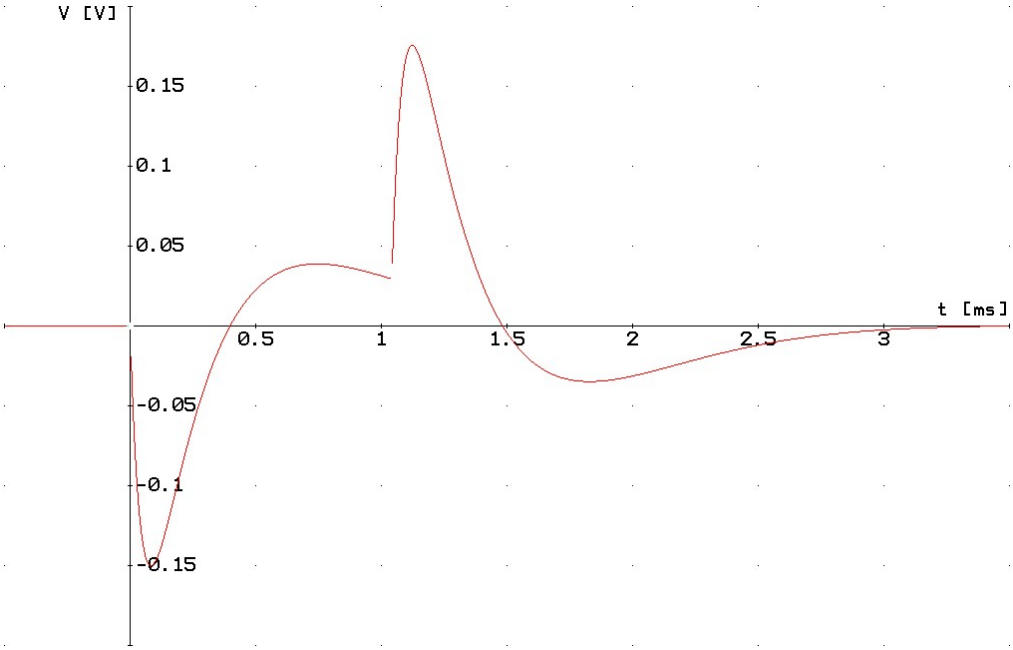

Figure 3.4: calculated waveform at the output of the shaper third stage when the input signal on IN_+ is a square pulse of about 1.04 ms temporal width.

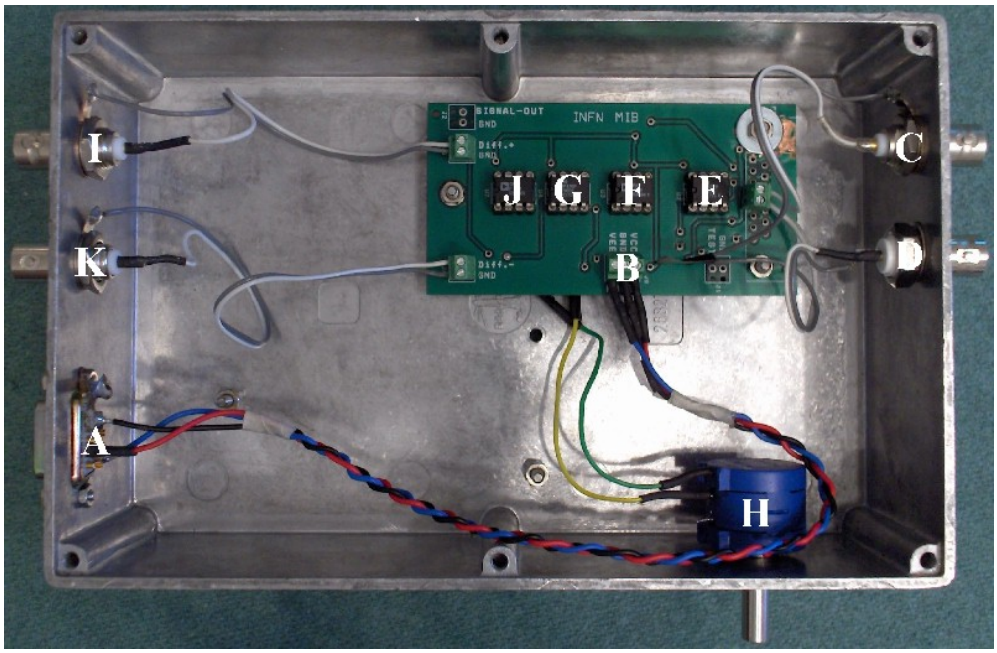

Figure 3.5: top view of the prototype shaper amplifier electronics board inside its shielding box.

The board is grounded via wires to the output BNCs and to the power supply port and it is also grounded directly to the chassis via one of the three metallic support towers.
In order to verify empirically the shaper behaviour, the apparatus described here below has been realized in the Milano–Bicocca electronics laboratory. A hp 33120A arbitrary function generator has been used to create the square wave shown in Figure 3.6 (top, left), which has 100 mV peak–peak amplitude, –50 mV offset, 240 Hz frequency and 25% duty cycle. This wave triggers and modulates an Agilent 81104A pulse/pattern

generator, which is set to create narrow pulses with 6.25 ns temporal width, –100 mV amplitude and 0 mV offset, which repeat with a frequency up to 80 MHz while the triggering wave is up. The obtained signal is represented in Figure 3.6 (top, right) and, except for the amplitude, it simulates quite well the PMTs anodic signals described in paragraphs 2.4, 2.5 and 3.1. Since 100 mV is the minimum settable amplitude for the 81104A, a hp 355D VHF attenuator with 30 dB attenuation factor has been positioned in cascade to the pulse/pattern generator, in order to reduce the signal amplitude and avoid saturation of the shaper operational amplifiers. The resulting waveform, shown in Figure 3.6 (bottom, left), is sent on the shaper non–inverting input. The shaper, powered by an external power supply at ±10 V and with the main amplification stage gain set to 11, gives on OUT_+ and OUT_- the response shown in Figure 3.6 (bottom, right).

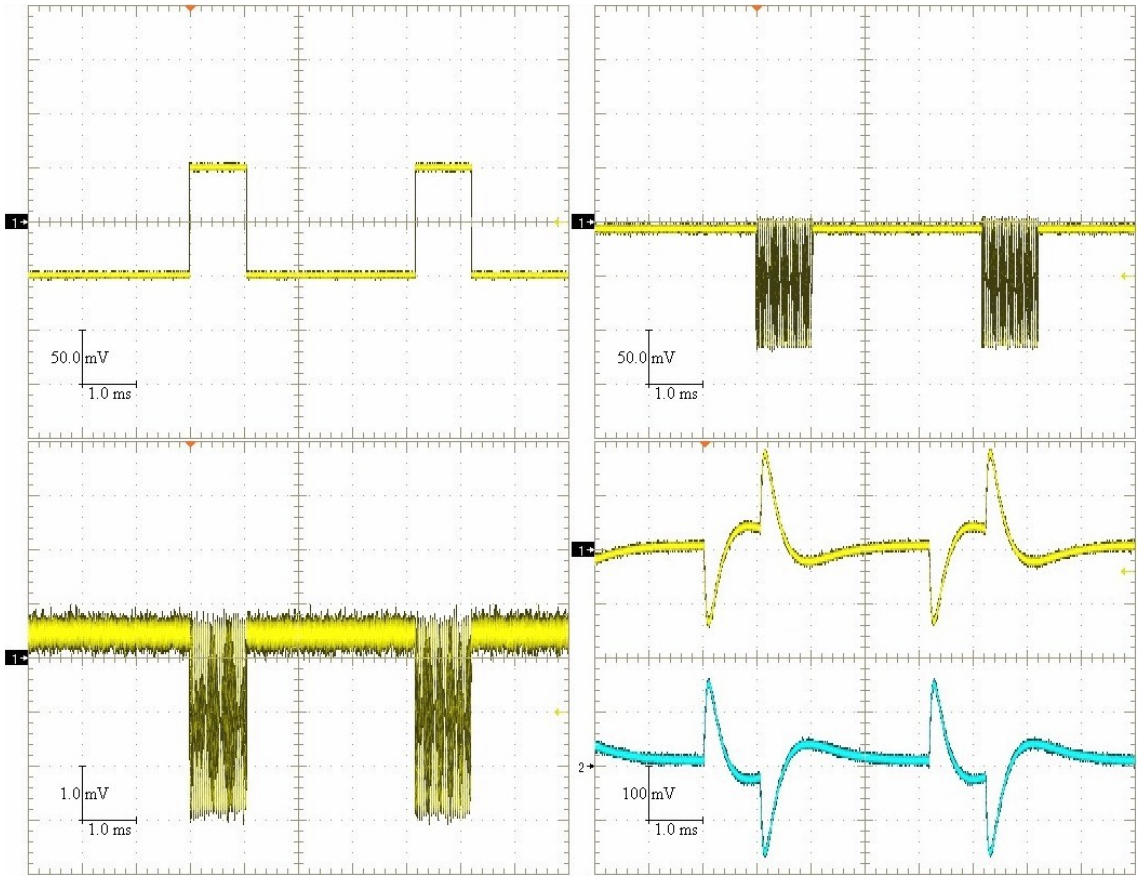

Figure 3.6: waveform at the output of the hp 33120A function generator (top, left), at the output of the Agilent 81104A pulse/pattern generator (top, right), at the output of the hp 355D VHF attenuator (bottom, left) and on the shaper amplifier differential output (bottom, right).

Both the output signals are very clean and they well match the theoretical prediction. As regarding the DC components, OUT_+ has a 0.2 mV offset, while OUT_- has a –0.3 mV offset, both of them being negligible if compared to the actual output signal amplitude of about 140 mV on each channel.
At this point, it is possible to change the frequency on the pulse/pattern generator in order to simulate a variation in the amount of light detected by the PMTs. As expected, the shaper output signal amplitude changes proportionally to the input pulse frequency.

A more accurate analysis of the system linearity will be done in paragraph 3.4, where the prototype shaper amplifier tests in lab 156 at CERN will be discussed.

3.3 – THE DAQ HW & SW

It is now necessary to choose the Analog to Digital Converter (ADC) which will be used to sample the analogical signals generated by the shaper amplifier. In order to select the most appropriate ADC among the many possibilities available on the market, the following requests should be satisfied.

- The ADC will be also used to sample the analogical signals generated in the pit by the final six–channel shaper amplifier. This means that the digitiser is requested to have at least six differential Analogical Inputs (AIs).
- The maximum ADC sampling frequency has to be high enough to permit the peak identification. In order to allow a fast real–time signal processing, the digitised waveform will be elaborated as it is, without reconstructing the actual analogical signal via the canonical convolution with the sinx/x interpolating functions. This of course asks for a high sampling frequency of the order of some tens ksamples/s on each differential channel.
- The final six–channel shaper amplifier is requested to fit into a single–width or, at most, into a double–width NIM module. To avoid connecting and disconnecting wires every time the ADC is needed and to assure that all the electronics remains into the NIM shielding box, the digitiser should be small enough to fit into the NIM module and also easy to connect to an external pc.

On the basis of this constraints, the National Instruments USB–6211 multifunction I/O has been chosen. As regarding the analogical inputs, this device offers 16 single ended channels, which can be combined to obtain 8 differential channels. The maximum input voltage range is ±10 V from each AI to the AI ground, while the input impedance is > 10 GΩ in parallel with 100 pF with device on and 1200 Ω in parallel with 100 pF with device off. The crosstalk, referred to a 100 kHz sine, is assured to be less than –75 dB between adjacent channels and less than –90 dB between non–adjacent channels. The AIs are multiplexed to a single ADC having 16 bits of resolution and 250 ksamples/s maximum sampling rate, with an internal buffer size enough to contain 4095 samples. The device overall dimensions, including the plug–in screw terminals, are 16.9 × 9.4 × 3.1 cm, while the connection with an external computer is assured via a B–series high speed USB port[20].

The software used to control the NI USB–6211 and to execute the real–time data elaboration has been developed using LabWindows/CVI, a C–based programmation language by National Instrument. This software has been created in order to satisfy the requirements of the final six–channel shaper amplifier which will be located in the pit and so it can perform data acquisition and elaboration on up to six analogical differential channels. In the following, the program will be presented only from a user point of view, the full code being reported and described in Appendix.

When the DAQ software is started, the window shown in Figure 3.7 appears.

- *Physical channels*: the physical differential AIs to be considered in the data acquisition and elaboration. The keyword *Dev* identifies the device alias and it is used by the computer to address the commands, while *ai* identifies the single differential AI. Up to six channels can be used, in whatever order.

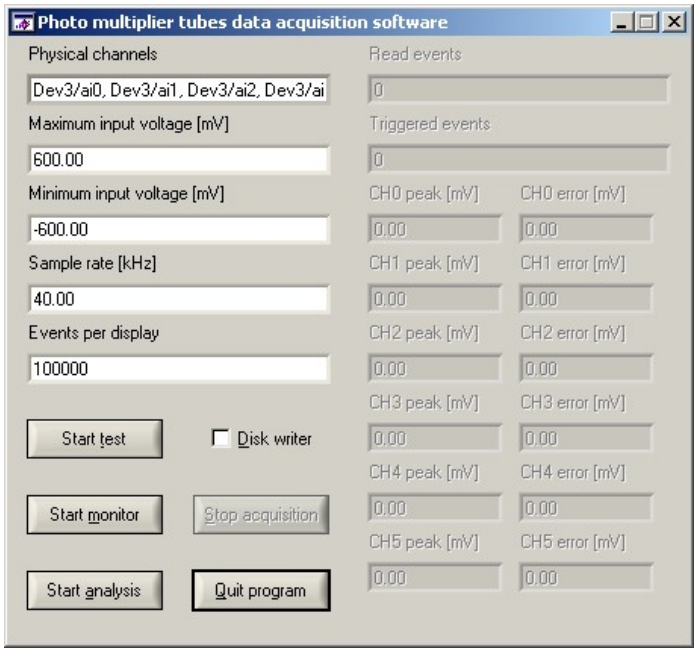

Figure 3.7: the DAQ software main dialog window.

- *Maximum & Minimum input voltage [mV]*: the expected maximum and minimum voltage to be digitised, expressed in mV with respect to the AI ground. These values are used by the ADC to automatically select the most appropriate conversion range among the four available possibilities: ±10 V, ±5 V, ±1 V, ±0.2 V. Furthermore, these values are used by the software itself to rescale the y–axis in the test, monitor and analysis panels described below.
- *Sample rate [kHz]*: the sample rate to be used on each differential AI, expressed in kHz. The maximum settable value has been limited to 41.00 kHz, corresponding to the ADC nominal maximum sampling frequency of 250 ksamples/s distributed on six channels.
- *Events per display*: the number of events successfully read and triggered after which a main panel refresh is forced. The refresh includes the updating of the main panel fields value and the processing of the system events, such as a mouse click. Since the program can become quite slow in responding to system events when this number is too high, the maximum settable value has been limited to 10^5, which gives a mean response time of about one minute. This field value also corresponds to the number of events successfully read and triggered over which the peak mean value and error are estimated in the monitor and analysis operating modes.
- *Disk writer*: checking this box when the monitor or the analysis operating mode is active enables recording the calculated parameters on the hard drive. If the test operating mode is active, the state of this box is ignored and no data is written on disk. The saved data includes the date and time of the measurement, the calculated peak mean value and the corresponding standard deviation for each of the active channels. The data is stored in a ASCII file named PMTsDAQsw_Data_YYYY.mm.dd_HH.MM.SS.dat, located in the program main folder.
- *Quit program*: exits the DAQ program.

When the *Start test*, *Start monitor* or *Start analysis* button is pressed, the program checks for the main panel values to be compatible with the imposed boundaries and, in case of mismatch, the error message shown in Figure 3.8 appears.

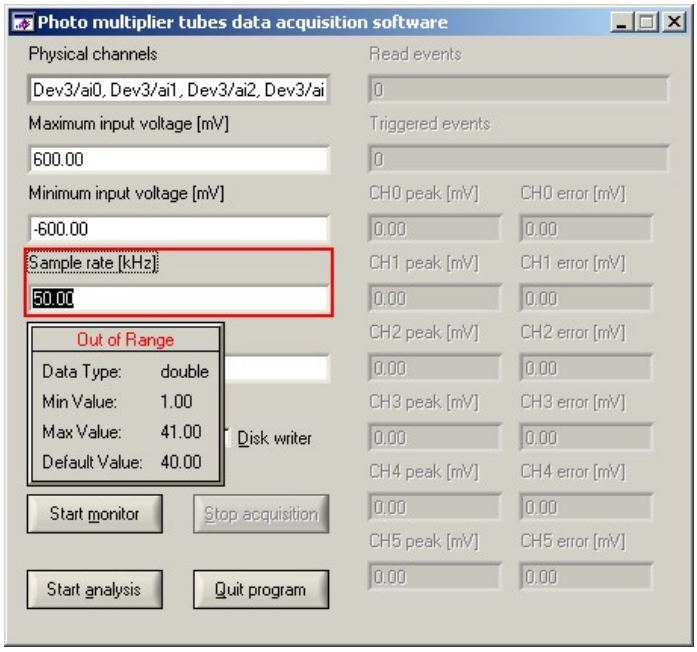

Figure 3.8: typical error message caused by a out–of–boundaries value.

Otherwise, if no error is found, the main dialog window enters the measurement mode, an example of which is shown in Figure 3.9.

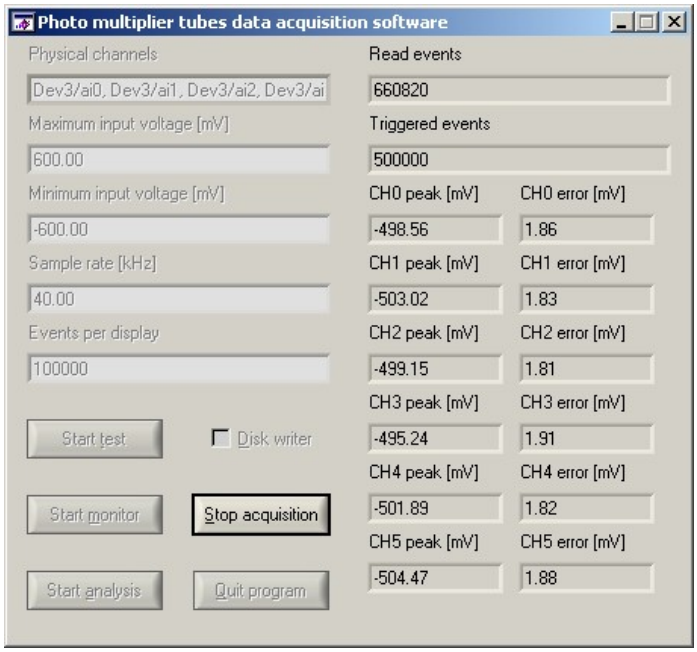

Figure 3.9: the DAQ software main dialog window in measurement mode.

- *Stop acquisition*: stops the running acquisition, closes the data file which is eventually being written and returns to the status shown in Figure 3.7.
- *Read events*: the number of complete waveforms read from the NI USB–6211 hardware buffer and transferred to the computer.
- *Triggered events*: the number of read events which have been triggered. The triggering process is slightly different depending on the selected operating mode, but basically it consists in verifying that the waveform peak position is far from the buffer edges.
- *CH* peak [mV] & CH* error [mV]*: the peak mean value and the corresponding error, relative to the *th differential AI. The mean value is calculated with an arithmetic mean over a number of triggered events equal to *Events per display*, while the error is obtained as the standard deviation of the mean over the same events. These fields are active only in the monitor and analysis operating modes and the number of used fields depends on the number of channels set in the *Physical channels* field.

A brief description of the three DAQ operating modes is given in the following.

- *Start test*: this mode allows to visualize the digitised waveforms, using the NI USB–6211 as a scope. When the mode is activated, the test panel shown in Figure 3.10 (left) appears on the computer screen next to the main dialog window and all the waveforms are plotted into it, triggered on a peak–position basis. By default, CH0, CH1 and CH2 are plotted in the A–side window, while CH3, CH4 and CH5 are plotted in the C–side one.

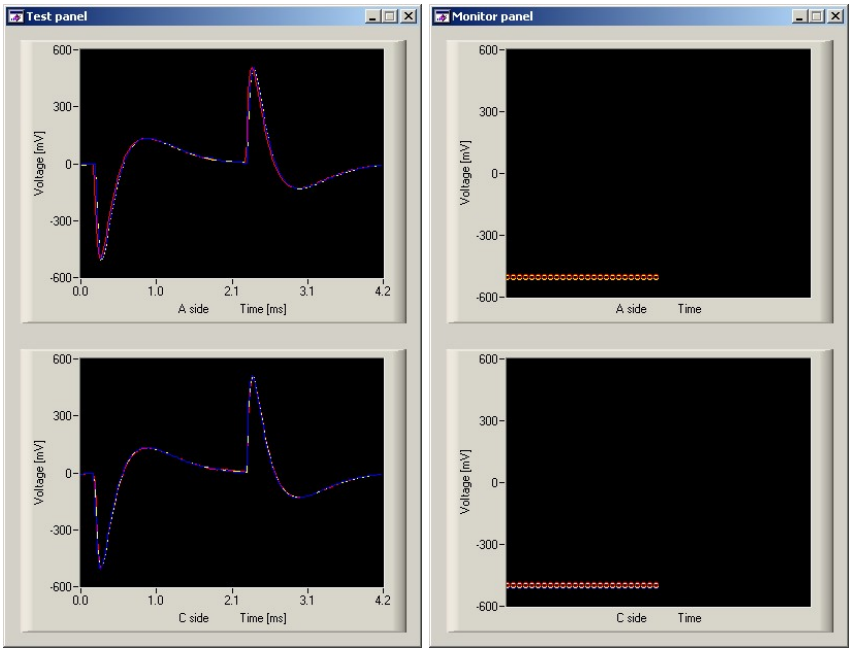

Figure 3.10: test panel (left) and monitor/analysis panel (right).

- *Start monitor*: this mode allows to calculate the waveform peak mean value and to monitor its trend during time. When the mode is activated, the monitor panel shown in Figure 3.10 (right) appears and the numerical peak values reported in the main dialog window *CH* [mV]* fields are plotted. For each triggered event,

the peak value is obtained by subtracting from the minimum acquired sample the baseline value, which is evaluated by averaging the pretriggered signal.

- *Start analysis*: similarly to the monitor mode, this mode allows to calculate the waveform peak mean value and to monitor its trend during time. When the mode is activated, an analysis panel similar to the one shown in Figure 3.10 (right) appears and the numerical peak values reported in the main panel *CH* [mV]* fields are graphically plotted. The difference with respect to the monitor mode is that here the peak values are extracted from fits on the triggered waveforms.

In order to execute fast real–time fits it is not convenient to proceed with numerical minimizations, because they would be too time–consuming: a simple formula is clearly needed. Since the waveform analytical expression is known and the only free parameter is the amplitude, it is possible to carry out explicitly a likelihood maximization and thus obtain the desired formula. Let y_i be the digitised voltage at time t_i, comprehensive of baseline, and let $C \cdot f(t_i)$ be the calculated voltage at the same time. Given a gaussian probability density function for the distribution of y_i – baseline around $C \cdot f(t_i)$, the probability of observing a digitised voltage in the interval $(y_i ; y_i + dy_i)$ is:

$$P_i = \frac{1}{\sqrt{2\pi}\sigma_i} \exp\left(-\frac{[y_i - baseline - Cf(t_i)]^2}{2\sigma_i^2} \right) dy_i$$

where σ_i is the error on the digitised voltage, which is the same for every sample. As a consequence, the logarithmic likelihood will be proportional to:

$$\ln(likelihood) \propto \sum_{i=1}^{N} [y_i - baseline - Cf(t_i)]^2$$

where the sum is extended over a certain number of acquired samples. By requiring the first derivative of this expression with respect to C to be zero, it is possible to obtain:

$$C = \frac{\sum_{i=1}^{N} f(t_i)[y_i - baseline]}{\sum_{i=1}^{N} f^2(t_i)}$$

This is precisely the actual formula used in the DAQ software to fit the digitised waveform. In order to make the computation faster and to avoid some undesired problems linked to the blank spaces in the PMTs anodic signal, the sums run only on a few samples around the peak, the exact number of which being settable via a constant in one of the header files. To get the peak value, with the baseline already subtracted, it is now sufficient to multiply C by $f(t_{max})$, which has been calculated numerically and inserted into one of the software header files.

This fitting procedure, based on analytical formulas, turns out to be very quick and reliable and allows the execution of the analysis operating mode in a time comparable to the one taken by the monitor mode, the fit using a negligible fraction of time. Despite this, the results obtained in analysis mode are much more precise, since the peak value is evaluated over several samples and not with a single point. The improved performance is reflected in the errors reported in the main dialog window, which result smaller using the analysis mode.

3.4 – PROTOTYPE TEST AT CERN

Having the prototype shaper amplifier and the DAQ HW & SW ready, it is possible to test the behaviour of the designed PMTs readout system under the real signals. For this

reason, the electronic apparatus illustrated in Figure 3.11 has been implemented at CERN, inside the laboratory 156 described in paragraph 2.3.

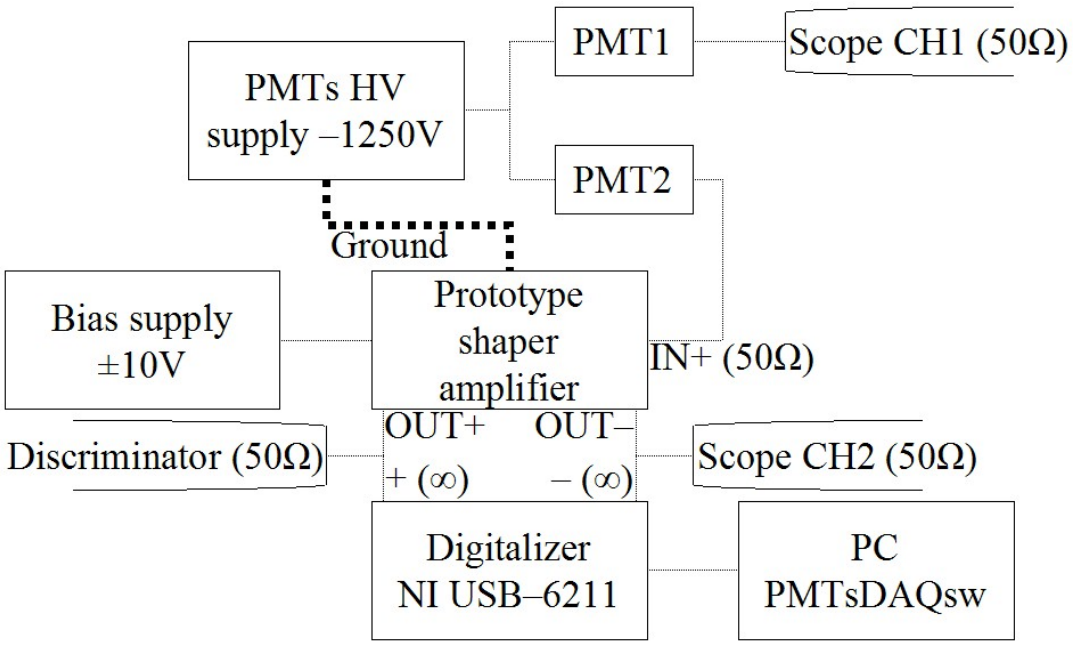

Figure 3.11: scheme of the electronic apparatus used in the laboratory 156 at CERN to test the designed PMTs readout system under the real signals.

Following the procedure described in paragraph 2.5, the Mitsubishi PK10 LED projector has been used to shine a test pattern on the three HPDs and on the two PMTs. The pattern is made up by a matrix of dots in correspondence of the HPDs and by two big spots on the PMTs photocathode. Both the PMTs are supplied by the same Fluke 415B high voltage power supply at the nominal voltage of –1250 V and the outcoming anodic signals are sent into ≈ 60 m long BNC cables in order to simulate the long–cable effects which will be introduced in the pit. The cable from PMT1 enters the oscilloscope CH1, which is terminated with the 50 Ω characteristic impedance and allows to visualize the raw anodic signal. The cable from PMT2, instead, enters the prototype shaper amplifier non–inverting input, the inverting input being grounded via a 50 Ω resistor. The shaper electronics board is supplied by a low voltage bias supply at ±10 V and the shaper shielding box is connected via a thick copper ground cable to the HV power supply chassis, in order to avoid ground problems. The shaper OUT+ is divided in two lines: one cable enters the digitiser AI0+ channel, which impedance is > 10 GΩ in parallel with 100 pF, while the other cable enters a 8–channel NIM discriminator terminated at 50 Ω, which use will be explained in chapter 4. Similarly, the shaper OUT– is divided in two lines: one cable enters the digitiser AI0– channel, while the other cable is connected to the scope CH2, terminated at 50 Ω. Finally, the NI USB–6211 is interfaced with a computer via a USB 1.1 port.
Using this configuration and shining the two PMTs with the same light colour, it is possible to observe on the scope the signal before and after the shaping process. Of course the shaped waveform, coming from the inverted output, will look reversed, but this does not prevent from extracting useful information. Figure 3.12 shows the raw and shaped signal when the PMTs are illuminated by blue light.

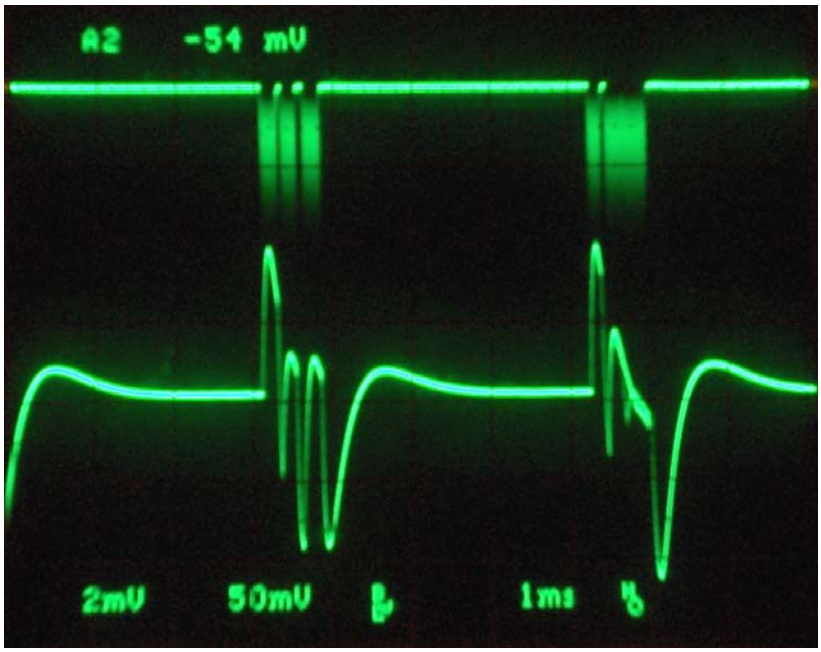

Figure 3.12: raw anodic signal (top) and shaped signal (bottom) when the PMTs are illuminated by blue light, using the Mitsubishi PK10 LED projector.

The signal on CH1 has the typical bunched temporal structure common to all the DLP beamers, but, in addition to this, it clearly presents some blank spaces inside the bunches. As given in paragraph 3.1, the positions of these blanks are not random, but they repeat according to a periodic sequence over several bunches, thus suggesting that their origin is linked with the DLP chip programming. The blanks clearly create problems in the shaped waveform, giving rise to undesired spikes. Anyway, it is possible to safely operate the shaper if the following two conditions are satisfied.

- The integrator characteristic time constant τ_L is much lower than the time period between the beginning of the bunch and the first blank space. In this case, in fact, the shaped signal peak is not affected by the spikes, which will grow only on the tail.
- When operated in analysis mode, the DAQ SW is configured in such a way to execute the fit only on the samples previous to the first spike. This can easily done by setting one of the constants declared in the header files.

Using green light instead of blue light to illuminate the PMTs photocatode, the situation shown in Figure 3.13 is obtained. Two main differences can be noticed with respect to Figure 3.12.

- The time period between the beginning of the bunch and the first blank space is much longer. This allows to use more samples for the waveform fit when the DAQ SW is operated in analysis mode.
- As reported in paragraphs 2.5 and 3.1, the green light bunches are much longer than the blue ones and so the inter–bunch time is reduced to 1670 ± 5 μs. As a consequence, the baseline is restored to a zero–value just before the beginning of the bunch. In order to obtain a good baseline estimation, it is then necessary to decrease the number of samples over which it is estimated, simply by changing the value of a constant in one of the header files.

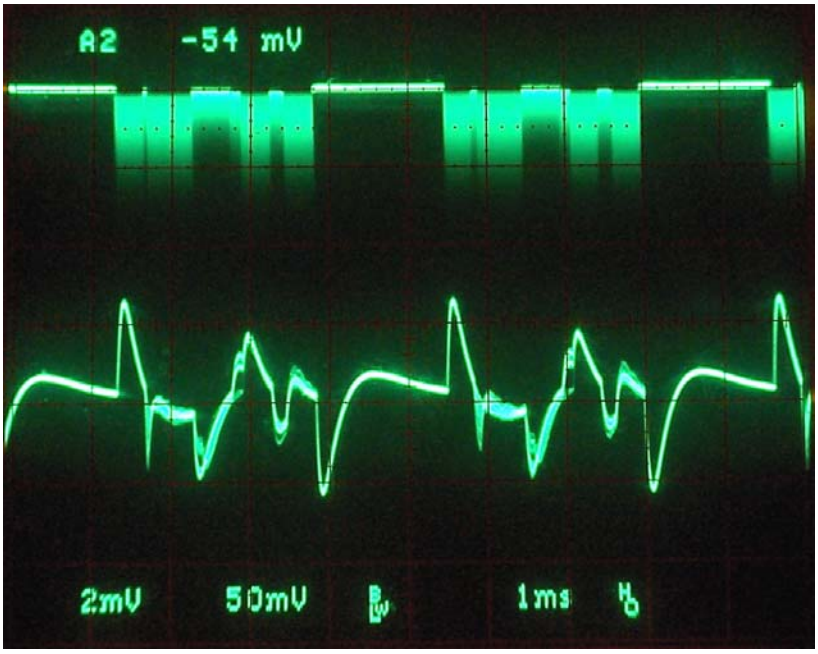

Figure 3.13: raw anodic signal (top) and shaped signal (bottom) when the PMTs are illuminated by green light, using the Mitsubishi PK10 LED projector.

Summarizing, the designed prototype shaper amplifier electronics board can be successfully used when the PMTs are illuminated with either blue or green light. Also the DAQ SW can be used in both cases, but, in order to optimise its performance, two constants need to be changed in one of the header files.

Using the experimental setup shown in Figure 3.11, it is now possible to check if the shaper output peak voltage is linearly proportional to the amount of light incident on the PMTs photocathode. To do this, several DAQ runs have been performed, changing the Kodak ND gelatine optical filters placed just downstream the Mitsubishi PK10 projector and so varying the beamer light attenuation factor in the range 10^3 to about $1.6 \cdot 10^4$. In particular, for each value of light attenuation four DAQ runs have been started, two with blue light and two with green light, running the DAQ SW both in monitor and analysis operating mode. All the data has been taken at 40 kHz sampling rate, with the parameter *Events per display* set to $5 \cdot 10^4$.

Figure 3.14 shows the results obtained with the monitor mode, while Figure 3.15 summarizes the peak values returned by the analysis mode. The y–values and errors correspond to the numbers read in the *CH0 peak [mV]* and *CH0 error [mV]* fields in the DAQ SW main dialog window, while the x–values correspond to the light intensities on the photocathode, calculated as 10^5/attenuation.

Observing the four data series it is clear that the PMTs readout system behaviour is linear along all the scanned range of light intensity. Nevertheless, the experimental errors returned by the DAQ SW are very small and seem to be underestimated. Now, the DAQ SW errors are calculated as standard deviations of the mean over $5 \cdot 10^4$ triggered events: these errors include the behaviour of the whole electronic chain, from PMT response statistical variations to noises picked–up by the long BNCs, from possible ground problems to eventual shaper instabilities. The fact that these errors are so small, the relative error being less than 0.08%, indicates that the electronic chain is stable and noise free. The problem has to be found in the optical part of the apparatus,

mainly in the ND gelatine optical filters, which show an actual attenuation different from the declared one. This can be confirmed by noticing that the experimental points relative to the same attenuation factor appear to be shifted up or down in the same way in all the four series. Of course it could be possible to repeat the measurements using calibrated filters to eliminate the systematics, but this would give no important information. It is then possible to start designing the definitive six–channel shaper amplifier.

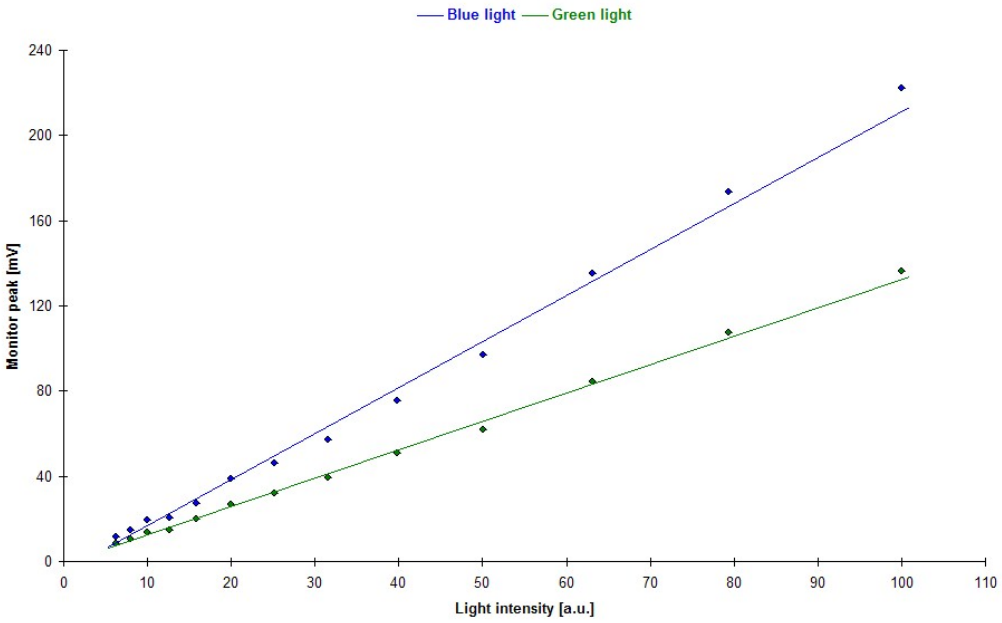

Figure 3.14: monitor peak, in mV, as a function of the light intensity on the PMT photocathode.

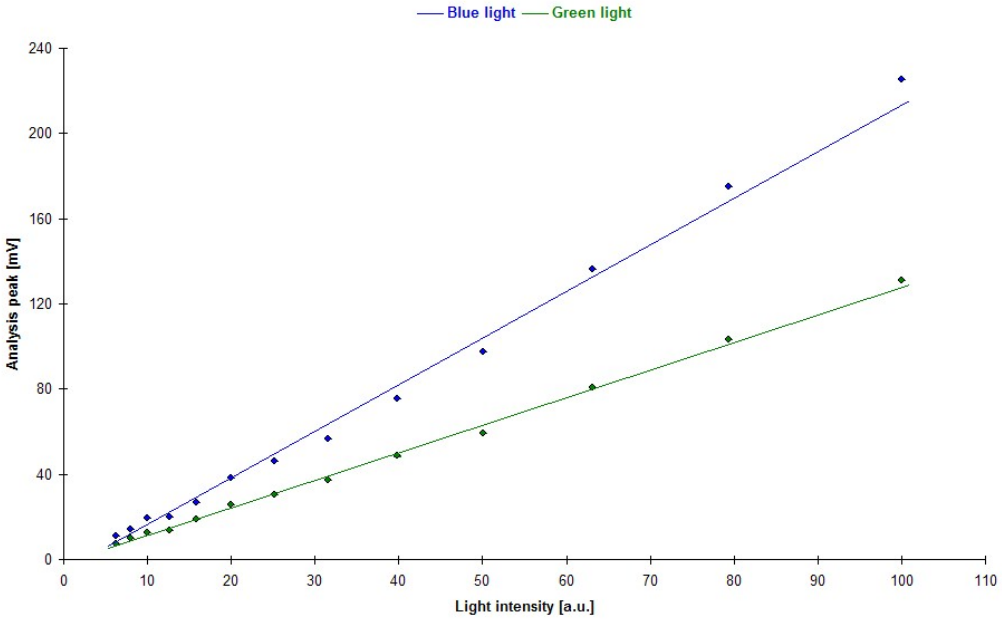

Figure 3.15: analysis peak, in mV, as a function of the light intensity on the PMT photocathode.

3.5 – NIM MODULE DESIGN AND PRELIMINARY TEST

As introduced in paragraph 3.3, both the analogical and the digital part of the six PMTs readout electronics are requested to fit into a single–width or, maximum, into a double–width NIM module. The chosen solution for the analogical part is to use six electronics boards similar to the one used for the prototype shaper amplifier. The schematic of each board is shown in Figure 3.16, the main differences with respect to the prototype being highlighted below.

- The third stage gain has been fixed to 19 by removing the 50 kΩ potentiometer and by substituting R23 with a 18 kΩ resistor. This will assure a better gain stability.
- The two 100 nF capacitors in the high–pass Bessel filter and the 47 nF capacitor in the low–pass filter have been changed from ceramic type to polystyrene type, the capacitor values themselves being maintained. As a consequence, a much lower temperature drift in the time constants and hence a more stable output is obtained.
- The operational amplifiers Analog Devices AD829 used in the prototype have been substituted either with Analog Devices OP27 or Analog Devices OP37, depending on the stage gain: OP27 is optimised for a low gain and so it has been used in the second and fourth stage, while OP37 is optimised for a gain greater than five and so it has been installed in the first and third stage. This change makes the electronics boards cheaper without losing in performance.
- The board components layout has been optimised by moving R24 to the R1 socket and R25 to the R15 socket.

The NIM module should also be able to provide an analogical output to be used in triggering the Odin acquisition supervisor during the magnetic distortion tests data acquisitions with the HPDs. The detailed procedure to be followed to trigger the Odin will be fully explained in chapter 4. For the moment it is sufficient to say that the triggering signal can be generated starting from a non–inverted shaper output. For this reason, a non–inverting unitary buffer has been included in the analogical electronics, its input coming from the non–inverted output of one of the shaper amplifiers.

Figure 3.17 shows the left side of the realized double–width NIM module. The bigger boards, numbered from 1 to 6, are the shaper amplifiers, while the smaller board on the right of the picture is the non–inverting unitary buffer. All the seven electronics boards are fixed on a plexiglass support, shaped in such a way to leave all the components accessible for a fast replacing. The module front panel presents seven BNC connectors, six analogical inputs and one analogical output. Each board is grounded in a double way: via one of the signal wires to the corresponding isolated BNC connector on the front panel and also via a 2 kΩ resistor connected to the NIM backpanel ground pin by one of the supply wires.

Also the NI USB–6211 has been included into the module, fixed on a plexiglass plate on the NIM module right side. The shaper amplifiers differential outputs have been connected via wires to the ADC differential inputs, from channel zero to channel five. The high speed USB interface port for connection with an external computer has been made accessible from the front panel. The boards top side and the digitiser, comprehensive of all the wiring, are shown in Figure 3.18. The wires correspondences between analogical inputs, board numbers and digitiser differential input channels are summarized in Table 3.1.

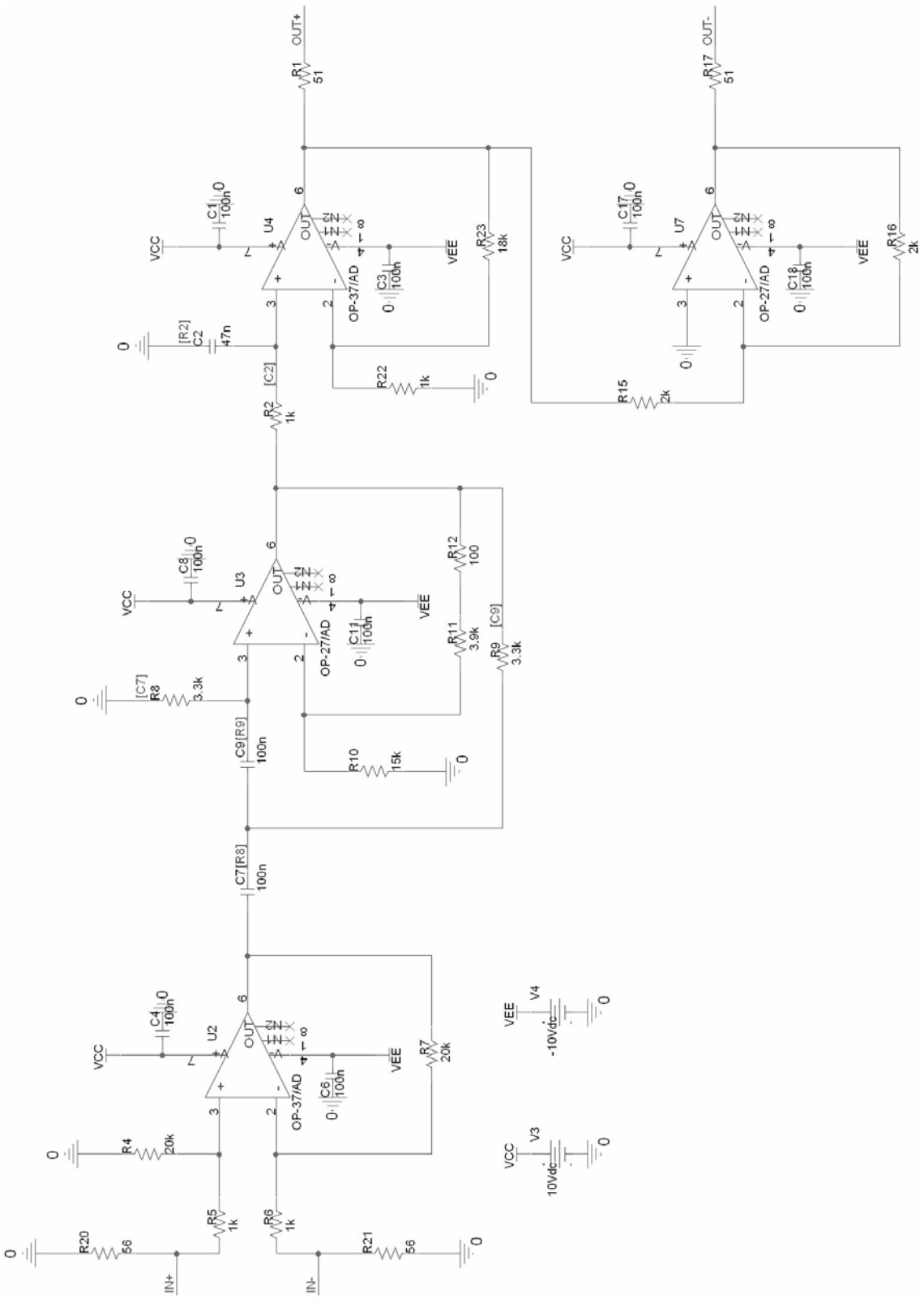

Figure 3.16: schematic of the re–optimised shaper amplifier to be used in the final NIM module.

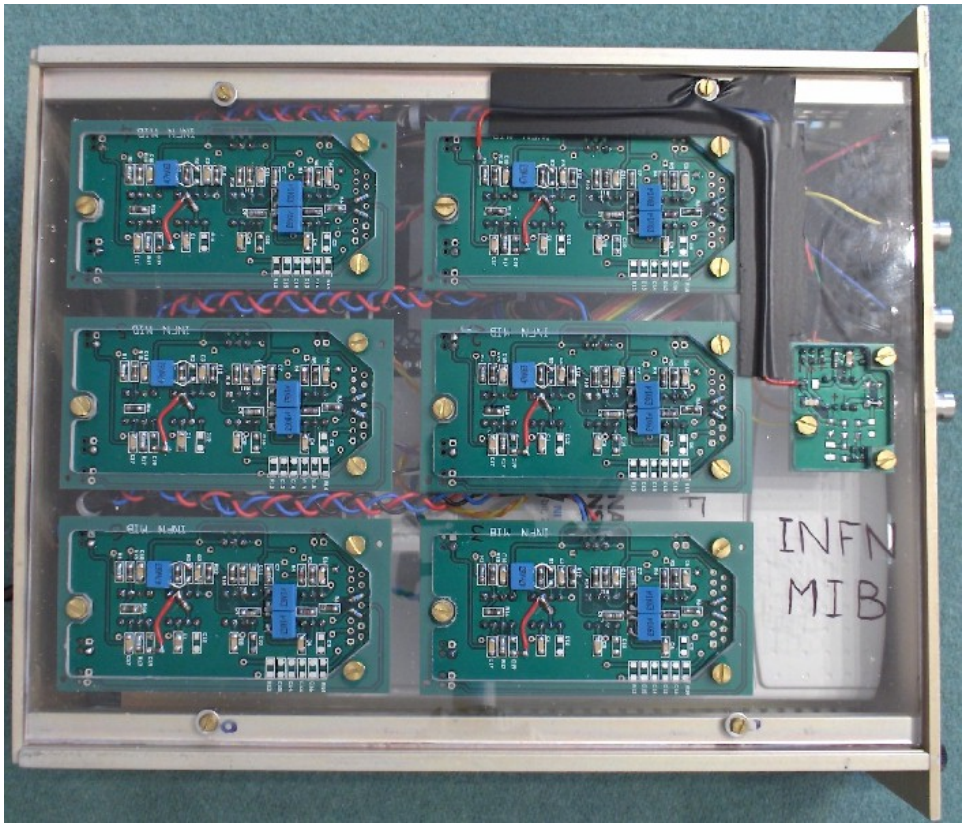

Figure 3.17: left side of the six–channel shaper amplifier + ADC double–width NIM module.

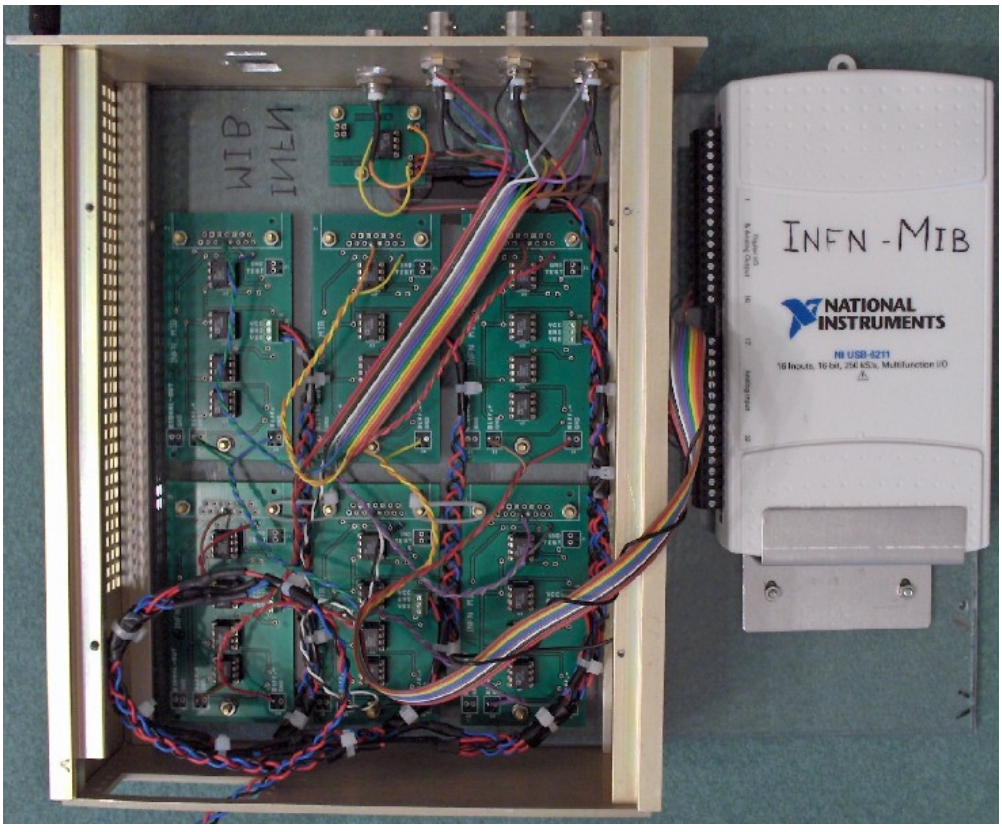

Figure 3.18: right side (opened) of the six–channel shaper amplifier + ADC double–width NIM module.

Front panel BNC connector	Wire colours	Board number	ADC differential AI
Left, top	Brown/red	1	ai0
Left, middle	Orange/yellow	2	ai1
Left, bottom	Green/blue	3	ai2
Right, top	Violet/grey	4	ai3
Right, middle	White/black	5	ai4
Right, bottom	Brown/red	6	ai5

Table 3.1: HW connections inside the NIM module and associated SW channels.

The six shaper amplifier electronics boards have been tested in standalone mode in Milano, by injecting an attenuated square wave and observing the corresponding two analogical output signals on a oscilloscope: all of them behave exactly as expected, without any undesired noise. The NIM module analogical output to be used as a source for the Odin triggering signal shows instead small spikes superimposed on the canonical waveform. These spikes are clearly due to the NI USB–6211 internal multiplexer, since their frequency changes according to the ADC sampling frequency and because they disappear stopping the digitiser. Anyway, given the small amplitude of the spikes and considering the purpose this signal has to accomplish, they do not constitute a problem.
The last tests carried out in Milano are about the module stability under temperature variations. A Sony Tektronix function generator is used to create a square wave with 50 mV peak–peak amplitude, –25 mV offset, 240 Hz frequency and 25% duty cycle. This signal is then split in two lines: one line is sent to one of the NI USB–6211 differential AIs in order to monitor the function generator stability, while the other line enters a 25 dB passive attenuator. In this way the ratio between the two signals does not depend on any drift of the function generator, thus improving the measurement accuracy. The attenuated signal is then split into six lines, which enter in the NIM module six analogical inputs. The six corresponding differential outputs are connected to the NI USB–6211 digitiser, while the NIM module analogical output is connected to an oscilloscope to real–time check that the waveform doesn't show any problem. At last, a National Semiconductor LM50 analogical centigrade temperature sensor, connected to the last available digitiser differential AI, allows to measure and record the temperature during all the data–taking period. Both the NIM module and the LM50 are supplied using an external power supply at ±10 V.
In order to measure the voltage drift of the only analogical part under temperature variations, the NIM module and the LM50 have been inserted into a programmable environmental chamber, while the digitiser has been left at room temperature. The environmental chamber has then been programmed to execute a 34 h temperature cycle, according to the following:

- T decreased from 26°C to 0°C in 1 hour;
- T maintained at 0°C for 1 hour;
- T increased from 0°C to 50°c in 14 hours;
- T maintained at 50°C for 2 hours;
- T decreased from 50°C to 0°C in 14 hours;
- T maintained at 0°C for 1 hour;
- T increased from 0°C to 26°C in 1 hour.

A modified version of the DAQ SW described in paragraph 3.3 has been used during the 34 hours long temperature cycle to acquire and record data from all the eight differential AIs of the NI USB–6211. The acquisition has been executed in analysis operating mode, with 30 kHz sampling frequency and with the *Events per display* parameter set to 10^5.
Observing the recorded data, one can notice that the temperature values in the first hour and in the last hour of the thermal cycle have larger rms values. This can be easily explained remembering that in these two time periods the temperature was changing of about half a degree per minute, while in the rest of the cycle the temperature change was less than 0.06 degrees per minute. Excluding the data at the beginning and at the end, a linear regression has been executed along all the thermal cycle in order to obtain the relative output voltage drift per unit degree on each of the six boards. The obtained values are reported in Table 3.2, in the column named *Drift in test 1*.

Board number	Drift in test 1 [ppm/°C]	Drift in test 2 [ppm/°C]
1	97.7 ± 2.3	100.2 ± 1.5
2	116.1 ± 2.4	114.7 ± 1.6
3	171.4 ± 4.1	113.8 ± 1.6
4	131.9 ± 2.3	124.6 ± 1.5
5	127.0 ± 2.4	129.1 ± 1.5
6	168.9 ± 4.3	116.9 ± 1.4

Table 3.2: results of the drift tests performed on the six shaper amplifier electronics boards.

The test has then been repeated using the same experimental setup, but including the NI USB–6211 inside the environmental chamber, in order to check if any further drift is added by the digitiser. The same temperature cycle has been applied and the acquisition has been run with the same settings. The results of the data analysis are summarized in Table 3.2, in the column named *Drift in test 2*.
The results obtained in the two tests are more or less the same, meaning that no important contribute is given to the system drift under temperature variation by the digitiser. This agrees with the low gain drift of a few ppm/°C declared in the NI USB–6211 datasheet. Looking more in detail at the data, the results of the two tests are in agreement within one sigma for boards 1, 2 and 5 and within two sigmas for board 4. However, boards 3 and 6 showed different behaviours during the two tests, the results being separated by about 10 sigmas. This is quite strange and not completely understood, but it does not constitute a problem, since even a relative voltage drift of 200 ppm/°C is well below the requirements the NIM module has to satisfy.

3.6 – NIM MODULE TEST IN THE PIT

The six–channel shaper amplifier + ADC double–width NIM module introduced in the previous paragraph has been installed in a NIM crate housed in D3, on the third floor of the LHCb counting room. This crate also houses the PMTs HV power supply and some other electronics. The module behaviour has been checked during the magnetic distortion tests in October 2007 and again at the beginning of November 2007.

The light source used during all the tests in the pit is the Mitsubishi PK10 LED projector described in paragraph 2.5, which has been moved from the laboratory 156 to the LHCb cavern. The beamer has not been placed in the final position inside the RICH2 vessel, but for the moment it has been fixed outside the vessel, until the exact final positions will be decided and the support towers will be ready. Figure 3.19 shows the actual position of the projector: it has been located at the base of the RICH2 A–side, reversed and inclined in such a way to partially illuminate the C–side columns. All the A–side columns remain shaded.

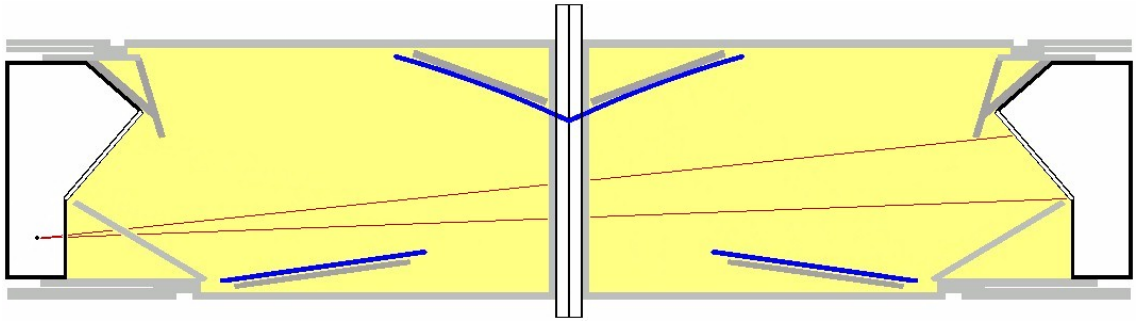

Figure 3.19: beamer position outside the RICH2 vessel during the tests carried out in October 2007 and in November 2007.

The projector is controlled by a computer positioned in the pit, about 30 m away from RICH2 and connected to the beamer via a long VGA cable. The projected pattern is constituted by a matrix of green dots in correspondence to the HPDs and by three bigger green spots on the PMTs photocathode.
The three PMTs on C–side are supplied with the nominal voltage of –1250 V, while the three PMTs on A–side are disconnected from the HV power supply. All the six BNCs are connected to the module. Table 3.3 summarizes the data relative to the six PMTs, comprehending the HV cables numbers, the BNC signal cables numbers and the BNCs connection position on the NIM module front panel.

PMT position	HV cable	BNC cable	Module BNC connector
A–side, top, middle	7068	7071L	Left, top
A–side, top, magnet side	7136	7127	Left, middle
A–side, bottom, magnet side	7137	7128	Left, bottom
C–side, top, middle	7141	7132	Right, top
C–side, top, magnet side	7142	7133	Right, middle
C–side, bottom, magnet side	7143	7134	Right, bottom

Table 3.3: cabling data of the six RICH2 PMTs.

The main problem encountered in the pit environment are the ground loops. The loop can go from the HV power supply to the tubes and back to the NIM crate via the BNC cables or it can be created when the gounds of two BNC cables from the PMTs are joined together. The use of isolated BNC connectors for all the channels of the NIM module and the introduction of 2 kΩ resistors on the safety grounds allows to eliminate

such problems. Figure 3.20 shows the digitalised waveforms as they are displayed by the DAQ SW once the ground loop problems have been eliminated.

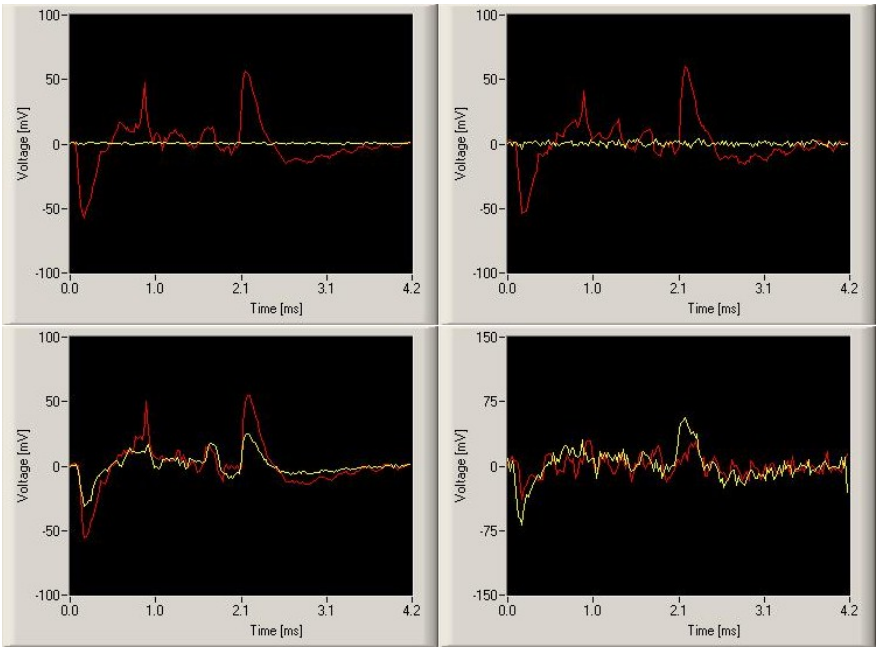

Figure 3.20: waveforms observed in the LHCb pit.

- The waveforms displayed in Figure 3.20 (top, left) have been obtained maintaining the module outside the NIM crate and supplying it with a low voltage power supply at ±12 V. The red signal is generated shaping the anodic signal of one of the C–side PMTs, while the yellow signal shows the filter output when no cable is connected at the input. Considering that the projector light intensity is quite low, the result is satisfactory. The strange behaviour of the red signal after the main peak is due to the blank spaces in the light emitted by the beamer, as it was fully explained in paragraphs 3.1 and 3.4.
- The waveforms in Figure 3.20 (top, right) have been obtained under the same conditions as the previous ones, except from the fact that now the yellow signal is obtained connecting one of the A–side PMTs, which are not supplied.
- In Figure 3.20 (bottom, left) both the waveforms are generated shaping the anodic signals of tubes on the C–side. The peak amplitude of the yellow curve is lower because the photocathode of the corresponding PMT is partially shaded and so it sees a lower quantity of light.
- Figure 3.20 (bottom, right) shows how the situation changes when the NIM module is inserted into the crate and the two channels are interchanged. There is clearly some noise entering from the ground pin, which deteriorates the S/N, but the software is still able to extract the peak value with good accuracy.

In these conditions, it was possible to exploit the three photomultipliers on C–side to align the test pattern during the magnetic distortion tests of October 2007. At the beginning of November 2007 the alignment procedure was repeated and the results confirmed that the projector's spatial stability is good, since a drift of one pixel was noticed in only one of the three PMTs.

4 – HPDs Quantum Efficiency Monitoring

The DLP DMD LED projector which has been selected as the light source for the magnetic distortion tests could also be used to periodically monitor the RICH2 HPDs quantum efficiency variations under aging. The basic idea is to shine a known amount of light on the photodetectors and to record the mean number of firing pixels in each HPD: a decrease in this number is an indication of a quantum efficiency loss. Since the beamer can provide more than one primary colour, it is also possible to monitor the Q.E. in different ranges of wavelength.
This kind of measurements can be done in parallel to the magnetic distortion tests, exploiting the same test pattern, or it can be carried out during dedicated runs. In both cases, in order to avoid undesired stray light effects, it would be good to use a dedicated shaped test pattern, to be carefully aligned before each data taking to assure that the same number of projector's pixels hit the HPD photocathode.
The alignment procedure is based on the PMTs response as explained below and, if automated, it can be completed in a few minutes. Starting from one of the three PMTs inserted in each photodetector plane, the beamer is programmed to draw a black screen with an horizontal line of a primary colour near the presumed PMT position. The line is then moved up or down and the corresponding peak values calculated by the PMTs readout system are recorded, until all the positions which give a non–zero response have been found. The procedure is then repeated using a vertical line to be moved to left or right. The non–zero response positions will form a rectangular zone corresponding to the PMT photocathode. These steps have to be repeated with all the three PMTs, which constitute absolute reference points that can be used to fit the prepared test pattern into the image. The described procedure allows to align the pattern with a precision corresponding to the projector's pixel size on the photodetector plane, which is exactly what is needed to assure that the same number of beamer's pixels hit the HPD photocathode.
The selected DLP projector is a commercial device and so it is not designed to have the long–term stability required for this kind of quantum efficiency monitoring: a decrease in the mean number of firing pixels could be due not to a real Q.E. loss, but to a variation in the amount of light emitted by the beamer itself. In order to solve this problem, it is possible to put a beamsplitter just downstream the projector and to exploit one of the two beams to measure the actual light intensity with a photodiode used as power meter. The quantity to be monitored is not just the mean number of firing pixels, but the ratio firing pixels/incident light. The PMTs, being placed at the same level than the HPDs, can give an indication of this quantity, but unfortunately they can undergo Q.E. losses similarly to the HPDs. For this reason, in case no strange phenomenon is noticed at the PMT level, the monitored quantity will be the ratio firing pixels/emitted

light. The PMTs can give important information that the power meter cannot give: first of all they are located at the same place than the HPDs, behind the photodetector window, and so they are affected by all the environmental variations in the same way as the HPDs are. Furthermore, the HPDs are complicated devices and the variations in the mean number of firing pixels can be due to many different reasons, while the PMTs are much simpler and well known.

4.1 – EXPERIMENTAL PROCEDURE

The monitoring technique described in the previous introduction will be considered for further developments in the case its sensitivity on relative quantum efficiency variations is better than 10%. In this paragraph I will explain the experimental procedure followed to estimate this sensitivity. The measurements have been performed in the laboratory 156 at CERN, which has been already described in paragraph 2.3.

Although it is not possible to directly increase and decrease the Q.E. by a known amount, it is of course possible to simulate such a situation. In fact, the direct consequence of a Q.E. loss is a proportional decrease in the number of produced photoelectrons: reducing the amount of light emitted by the beamer, with a fixed HPD response, will give the same effect and will thus simulate a Q.E. loss. The basic idea is then to execute different DAQ runs with the HPDs, changing the ND optical filters placed in front of the projector and recording the firing pixels statistical distributions. Since all the measurements are done in a period of few weeks, there is no need to use a power meter to monitor the long–term light intensity decrease: the actually measured quantity is the mean number of firing pixels and not the ratio firing pixels/emitted light.

The experimental apparatus is basically the one shown in Figure 3.11, plus the HPD column and the relative readout electronics. The Mitsubishi PK10 DLP DMD LED beamer is programmed to shine on the photodetector plane the test pattern shown in Figure 4.1 (left), which is composed by a black screen with a matrix of blue dots for each of the three active HPDs and with a big blue spot for each of the two PMTs. As it can be seen from the figure, the dot matrices have been shaped following the HPDs photocathode contour, in order to minimize the undesired stray light effects. The pattern is then aligned following the matching procedure described in the introduction to this chapter.

In this apparatus, the prototype shaper amplifier illustrated in paragraphs 3.2 and 3.4 is used to readout the anodic signal from PMT2. The non–inverting output is sent to a eight–channels NIM discriminator set in such a way to generate a pulse in correspondence with the beginning of each photon bunch. This pulse is converted from NIM to ECL logic using a NIM–ECL/ECL–NIM adapter and it is then sent to the Odin acquisition supervisor board in order to acquire data from the HPDs only when they are illuminated by the projector's light. This trick allows to increase the signal/background ratio in the stored data files by a factor from two to four with respect to an acquisition with random triggers.

The column L0 boards, the external L1 board, the event builder software and the online monitoring software are set to operate in LHCb mode. After turning on the low voltages boards via the Detector Control System (DCS) software, the online monitor appears to be very noisy, because the HPDs silicon chips are not reverse–biased. When the silicon bias power supply is set to a voltage of 60V, the most part of the noise disappears, but a few intrinsically noisy pixels continue to fire even without being excited. At this point it

is possible to increase slowly the high voltage, checking in the meanwhile the column behaviour via the online monitor. At around –8 kV HV it is possible to distinguish the first pattern structures and to spot three tubes with high ion feedback. When the voltage of –19.8 kV is reached, I start a DAQ run of about 10^5 events and I set the event builder software to record all the acquired data on disk. Figure 4.1 (right) shows the projected pattern as it appears on the online monitor.

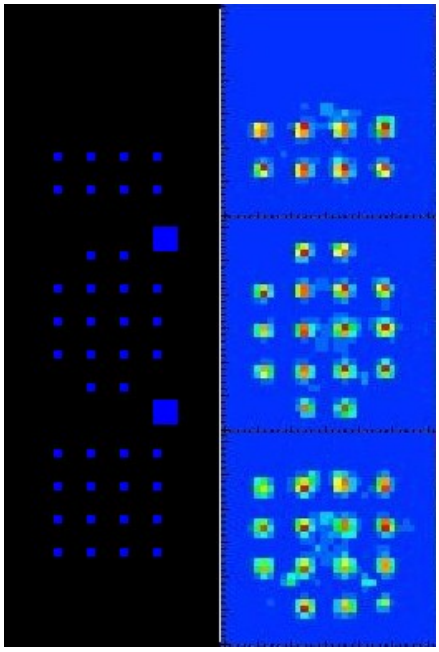

Figure 4.1: the test pattern programmed on the projector (left) and the same pattern as it appears on the online monitor at 19.8 kV HV (right).

The three active HPDs, from top to bottom, are respectively HPD 628, HPD 629 and HPD 684. None of them has any noisy pixel, but HPD 628 shows a light ion feedback, as it can be noticed by the cluster of counts in the centre which does not correspond to any pattern structure. The response of HPD 629 is very clean, while HPD 684 shows two filament–like structures which start from the bottom corners and cross each other in the centre. These structures are due to the two bottom external pattern pixels which hit the Mumetal shield and are reflected on the photocathode surface. This hypothesis is confirmed by the observation that the filament–like structures can be eliminated simply by shifting up the dot matrix relative to HPD 684.
Figure 4.2 is a complete online monitor screenshot taken during a run. Numbering the graphs from the top left corner, the first sixteen plots show the count frequency of each HPD silicon pixel in the column. The three tubes with high ion feedback are clearly visible on the top left corner: this effect is particularly marked on the tube represented in the sixth plot, as it can be seen from the scale and from the cluster of counts in the centre. The pixel chips represented in the fourth, fifth and ninth plots have noisy pixels, while the eighth, twelfth and fourteenth plots are respectively HPD 628, 684 and 629. The seventeenth plot corresponds to the superimposition of all the previous ones and can be useful to keep under control the general situation. The last five plots represent respectively the hit distribution on HPD 628, on HPD 684, on HPD 629, on all the HPDs and the hit trend of all the HPDs. These are the most important quantities to keep

under control while ramping up the high voltage, in order to check that the light incident on the photodetectors is not too intense. Furthermore, these are also the plots which will be used to monitor the Q.E.s.

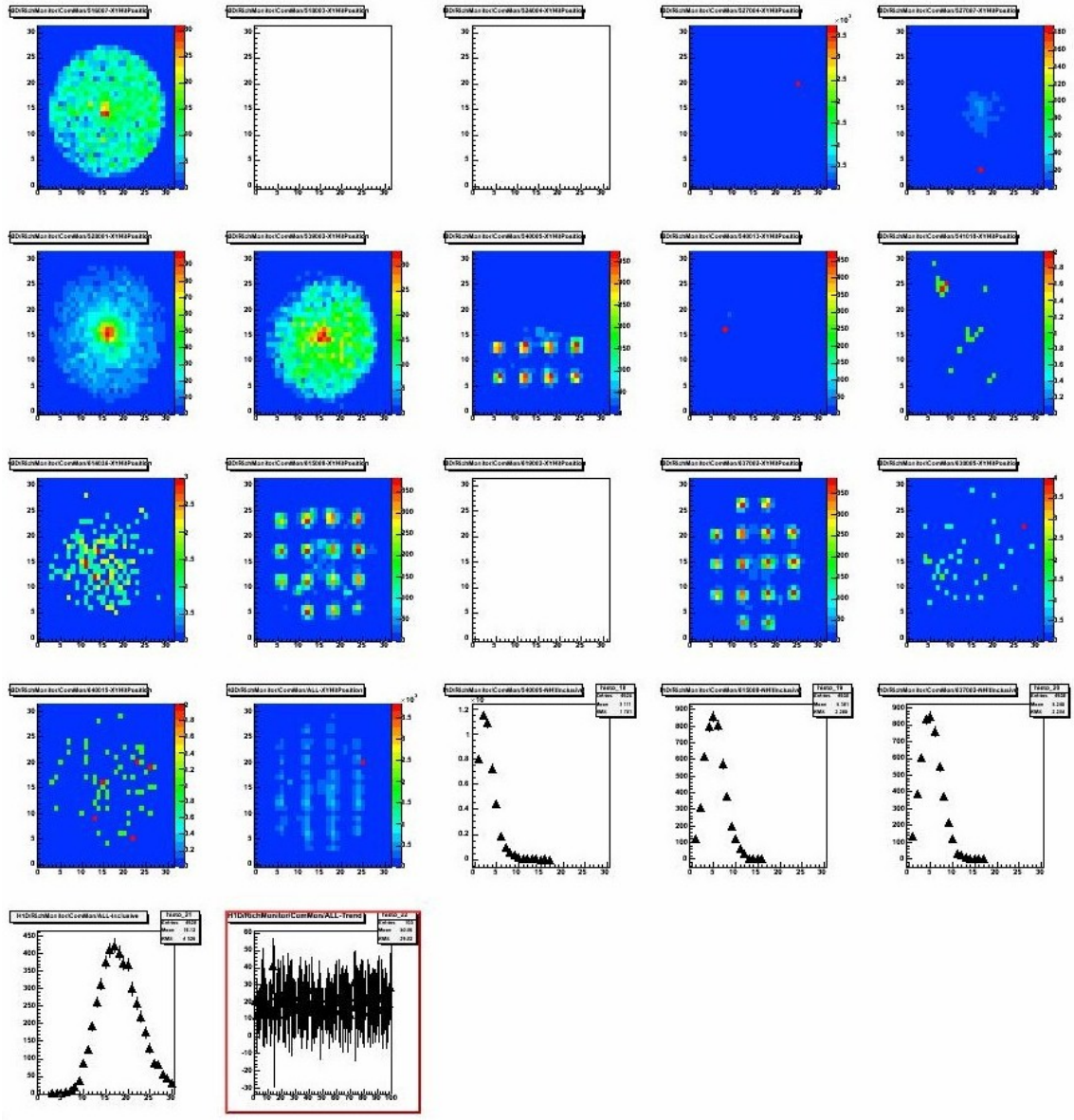

Figure 4.2: a typical online monitor screenshot.

4.2 – DATA ANALYSIS AND RESULTS

Using the experimental procedure illustrated in the last section, some data taking runs with blue light and with different light attenuations have been performed, each run recording about 10^5 triggered events.

The data analysis has been carried out on the basis of the following assumptions.

- When the HPD photocathode is hit by a mean number of photons per unit time equal to $\langle \#_\gamma/dt \rangle$, a mean number of photoelectrons per unit time equal to $\langle \#_{pe}/dt \rangle = \text{Q.E.} \cdot \langle \#_\gamma/dt \rangle$ will be released, thus producing a response *R* in the

anode pixel chip. The result of a quantum efficiency loss is a proportional decrease of $\langle \#_{pe}/dt \rangle$ and then of R. An externally controlled decrease of $\langle \#_{\gamma}/dt \rangle$ with a fixed quantum efficiency would produce exactly the same effect. As a consequence, it is possible to estimate the sensitivity S of the relative quantum efficiency monitoring technique by evaluating the sensitivity S' of the response R to a variation in the incident light intensity.

- As it can be noticed from Figure 4.2, the actual anode response R is not simply a number, but it is a firing pixel spectrum. This distribution represents a random phenomenon with a fixed temporal mean $\langle R \rangle$ and then it can be described from a theoretical point of view using a Poisson probability density function. Since a Poisson is completely defined by the mean, it is possible to identify the firing pixel spectrum with its mean value, which is much more easy to handle. Figure 4.3 shows three Poisson fits on real data relative to HPD 628, 629 and 684. The fits have been performed with Minuit: since the used minimization function shows problems when fitting a rescaled histogram, the original data has been fitted with a non–renormalized Poisson.

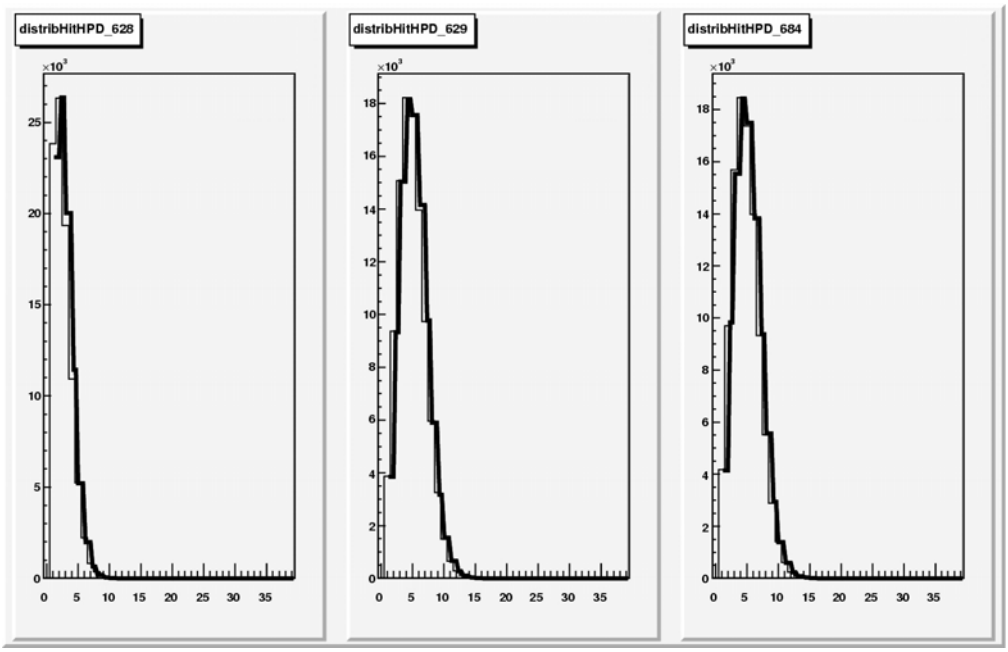

Figure 4.3: experimentally observed firing pixel spectra for HPD 628, 629 and 684 (thin lines) and fitted Poisson probability density functions (thick lines).

- The mean response $\hat{R}$ extracted from the fit is an estimator of the actual Poisson parameter $\langle R \rangle$ and it is distributed around $\langle R \rangle$ following a normal probability density function with mean $\langle R \rangle$ and unknown standard deviation σ. If it is possible to find the gaussian rms value, the sensitivity S' of the response R to a relative variation in the incident light intensity can be simply calculated as a relative resolution, according to the formula:

$$S = S' = \frac{FWHM}{\langle R \rangle} \approx \frac{FWHM}{\hat{R}} = 2\sqrt{2\ln 2}\,\frac{\sigma}{\hat{R}} \approx 2.35\,\frac{\sigma}{\hat{R}}$$

- Since I have only one or two experimental points for each light intensity, it is not possible to extract σ from a gaussian fit on the $\hat{R}$ spectrum. However, one can estimate σ in an indirect way if the resolution trend as a function of the light intensity is known. In first approximation, one can suppose the sensitivity S' to be constant over all the range of considered light intensities, which implies the gaussian rms value to be proportional to the estimated anode response.
- The amount of incident light on the HPDs photocathode is very low during all the data taking. In fact, the maximum value of $\hat{R}$ estimated from the firing pixel spectra is less than 5.7 firing pixels per event on a single HPD. This is very important, because under this condition the HPDs, although being intrinsically digital, behave as analogical devices, since they give a mean response $<R>$ proportional to the light intensity on the photocathode. To demonstrate this, let's suppose for a moment that the number of firing pixels corresponds to the number of produced photoelectrons. In LHCb mode, the mean number of photoelectrons per pixel per event will be less than $5.7/32^2 \approx 5.6 \cdot 10^{-3}$, which gives a probability to have more than one photoelectron hit in the same pixel in the same event:
$$P_{(5.6\cdot10^{-3})}(>1) = 1 - P_{(5.6\cdot10^{-3})}(0) - P_{(5.6\cdot10^{-3})}(1) \approx 1.5\cdot10^{-5}$$
As a consequence, the number of firing pixels is actually the same than the number of produced photoelectrons and so the mean anode response $<R>$ has been demonstrated to be linearly proportional to the amount of incident light on the HPD photocathode.
- Given the previous points, it is possible to calculate the sensitivity S of the relative quantum efficiency monitoring technique for each of the three considered HPDs. First of all I plot on a graph the values of $\hat{R}$, estimated from the Poisson fits on the firing pixel spectra, versus the corresponding light intensities, calculated as 10^5/attenuation. I also set the errors on the y–axis to be proportional to the y values themselves, via a proportionality constant K which is the same for all the y values. Then I perform a weighted linear fit to the so obtained data, I calculate the reduced χ^2 and I adjust the value of K until the reduced χ^2 becomes equal to 1. Since K corresponds to the ratio between the $<R>$ gaussian rms value and the estimated $\hat{R}$, the sensitivity will be $S = S' \approx 2.35 \cdot K$.

Figure 4.4 shows the three weighted linear fits of the experimental data used to estimate the gaussian spreads σ. The fits from HPD 629 and 684 are very similar, while the one from HPD 628 lays under the others because this tube has only half the photocathode illuminated by the projector's light. It can be noticed that all the three fits have a non–vanishing ordinate at the origin. This gives an estimation of the dark count rate in each tube, due to noisy pixels, thermionic emissions from the photocathode or real photoelectric effects induced by non–shielded environmental light.

Table 4.1 summarizes the values of $K = \sigma/\hat{R}$ and S extracted from the data. The sensitivity ranges from 4.4% to 8.7%, thus resulting inside the required value of 10%. The obtained values could be a bit overestimated, since the values of emitted light are affected by an error, as it was noticed in paragraph 3.4. In conclusion, the considered HPD quantum efficiency monitoring technique has been proven to be adequate and it can be considered for further developments.

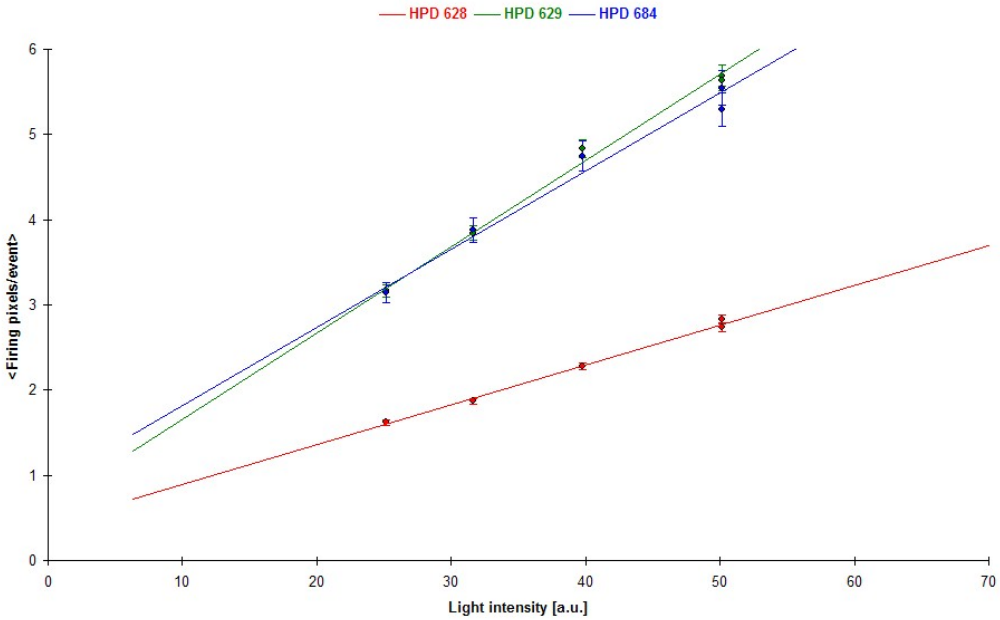

Figure 4.4: mean number of firing pixels/event as a function of the light intensity for the three HPDs illuminated by the projector's light.

HPD number	***K* [%]**	***S* [%]**
628	1.87	4.40
629	2.15	5.06
684	3.69	8.69

Table 4.1: values of *K* and *S* extracted from the data analysis.

APPENDIX

The following is the software code used to control the NI USB–6211 digitiser included in the NIM module and to execute the required real–time data elaboration. It has been developed with LabWindows/CVI, a C–based programmation language by National Instruments, and it requires the CVI real time engine to be install on the hosting computer in order to run properly. For details on how to operate this software see paragraph 3.3.
The code reported here below is contained in the *PMTsDAQsw.h* header file. It defines the constants used in the User Interface Resource (UIR) file, links the definitions to the actual codes handled by the program and declares the callback functions prototypes.

```
/*****************************************************************************/
/* LabWindows/CVI User Interface Resource (UIR) include file                 */
/* Copyright (c) National Instruments 2007. All rights reserved.             */
/* WARNING: Do not add to, delete from, or otherwise modify the contents of  */
/*          this include file.                                               */
/*****************************************************************************/


#include <userint.h>


#ifdef __cplusplus
 extern "C" {
#endif
// Panels and controls
#define MEAPAN                          1
#define MEAPAN_ASIMEA                   2
#define MEAPAN_CSIMEA                   3
#define PHOMUL                          2
#define PHOMUL_PHYCHA                   2
#define PHOMUL_MAXINP                   3
#define PHOMUL_MININP                   4
#define PHOMUL_SAMRAT                   5
#define PHOMUL_EVEPER                   6
#define PHOMUL_REAEVE                   7
#define PHOMUL_TRIEVE                   8
#define PHOMUL_CH0PEA                   9
#define PHOMUL_CH0ERR                  10
#define PHOMUL_CH1PEA                  11
#define PHOMUL_CH1ERR                  12
#define PHOMUL_CH2PEA                  13
#define PHOMUL_CH2ERR                  14
#define PHOMUL_CH3PEA                  15
#define PHOMUL_CH3ERR                  16
#define PHOMUL_CH4PEA                  17
#define PHOMUL_CH4ERR                  18
#define PHOMUL_CH5PEA                  19
#define PHOMUL_CH5ERR                  20
#define PHOMUL_STATES                  21 // Callback function: States
```

```
#define PHOMUL_STAMON                   22 // Callback function: Stamon
#define PHOMUL_STAANA                   23 // Callback function: Staana
#define PHOMUL_DISWRI                   24
#define PHOMUL_STOACQ                   25 // Callback function: Stoacq
#define PHOMUL_QUIPRO                   26 // Callback function: Quipro
#define TESPAN                          3
#define TESPAN_ASITES                   2
#define TESPAN_CSITES                   3
// Callback prototypes
int  CVICALLBACK Quipro(int panel,int control,int event,void *callbackData,
 int eventData1,int eventData2);
int  CVICALLBACK Staana(int panel,int control,int event,void *callbackData,
 int eventData1,int eventData2);
int  CVICALLBACK Stamon(int panel,int control,int event,void *callbackData,
 int eventData1,int eventData2);
int  CVICALLBACK States(int panel,int control,int event,void *callbackData,
 int eventData1,int eventData2);
int  CVICALLBACK Stoacq(int panel,int control,int event,void *callbackData,
 int eventData1,int eventData2);
#ifdef __cplusplus
 }
#endif
```

The code reported here below is contained in the *MyHeader.h* header file. It declares the *Initalize* and *Terminate* functions prototypes, the constants and the global variables.

```
/****************************************************************************/
/* LHCb collaboration                                                       */
/* INFN Milano - Bicocca                                                    */
/* RICH2 photo multiplier tubes data acquisition software                   */
/* This software allows to read the integrated anodic signal of the 6 RICH2 PMTs */
/****************************************************************************/



void Initialize(double *,int *,TaskHandle *,FILE **,int *,int *,double **,int *);
void Terminate(TaskHandle *,int *,int *,double **,FILE **);



/*****************************************************************************/
/* User settable constants:                              Default values:     */
/* Dperiod [ms] -> beamer's period, typically 1/(n*(refresh rate))           */
/*                                                       =4.166666666666667E+0  */
/* Dtimout [s]  -> amount of time to wait for the function to read the samples */
/*                                                       =5.E+0              */
/* Dpredut [--] -> fraction of the period to be used for baseline evaluation */
/*                                                       B=5.E-2   G=2.5E-2  */
/* Dristim [ms] -> amount of time between the beginning of the bunch and the peak */
/*                 position                              =8.3376E-2          */
/* Da      [--] -> real part of the Bessel poles, times Dtau_H =-8.666666666666667E-1 */
/* Db      [--] -> absolute value of the imaginary part of the Bessel poles, times */
/*                 Dtau_H                                =4.988876515698589E-1  */
/* Dtau_L  [ms] -> low-pass RC (integrator)              =4.7E-2             */
/* Dtau_H  [ms] -> high-pass CR (differentiator)         =3.3E-1             */
/* Dpeadut [--] -> fraction of the period to be used for peak fitting        */
/*                                                       B=3.6E-2   G=7.4E-2 */
/* Dscafac [V]  -> scaling factor for the peak value     =6.2153E-1          */
/*****************************************************************************/
const double Dperiod=4.166666666666667E+0;
const double Dtimout=5.E+0;
const double Dpredut=5.E-2;
//const double Dpredut=2.5E-2;
const double Dristim=8.3376E-2;
const double Da     =-8.666666666666667E-1;
const double Db     =4.988876515698589E-1;
const double Dtau_L =4.7E-2;
const double Dtau_H =3.3E-1;
const double Dpeadut=3.6E-2;
//const double Dpeadut=7.4E-2;
```

```
const double Dscafac=6.2153E-1;
/********************/
/* Other constants: */
/* DO NOT MODIFY    */
/********************/
const double De_3=1.E-3,De3=1.E+3,Dzero=0.E+0;
const int Izero=0,Ione=1,Itwo=2,Ithree=3,Ifour=4,Ifive=5;
/*****************************************************************************/
/* acqtyp defines the acquisition type according to the following scheme:    */
/* acqtyp=0 -> test,       running   (displays waveform)                     */
/* acqtyp=1 -> monitoring, running   (looks for peak and subtracts baseline) */
/* acqtyp=2 -> analysis,   running   (fits peak and baseline)                */
/* acqtyp=3 -> test,       stopped                                           */
/* acqtyp=4 -> monitoring, stopped                                           */
/* acqtyp=5 -> analysis,   stopped                                           */
/*****************************************************************************/
int phomul,acqtyp;
```

The code reported here below is contained in the *PMTsDAQsw.c* source file. It contains the main program, the callback functions and the *Initialize* and *Terminate* functions.

```
/*****************************************************************************/
/* LHCb collaboration                                                        */
/* INFN Milano - Bicocca                                                     */
/* RICH2 photo multiplier tubes data acquisition software                    */
/* This software allows to read the integrated anodic signal of the 6 RICH2 PMTs */
/*****************************************************************************/



#include <stdio.h>
#include <stdlib.h>
#include <math.h>
#include <time.h>
#include <NIDAQmx.h>
#include "PMTsDAQsw.h"
#include "MyHeader.h"



int main(int argc,char *argv[])
{
 // Loads main panel, displays it and operates it (until QuitUserInterface() is called)
 phomul=LoadPanel(Izero,"PMTsDAQsw.uir",PHOMUL);
 DisplayPanel(phomul);
 RunUserInterface();
 // Discards main panel
 DiscardPanel(phomul);
 return(Izero);
}



int CVICALLBACK States(int panel,int control,int event,void *callbackData,
 int eventData1,int eventData2)
{
 if(event==EVENT_COMMIT)
 {
  TaskHandle testas;
  FILE *tesfil=NULL;
  double tesrat,*tesdat=NULL,peak;
  int teseve,tescha,tesdim,tespan,reaeve=Izero,trieve=Izero,preris,*pos=NULL,i,nsRfec,
   trig_d,j,pos1,pos2,k,colors[3]={VAL_RED,VAL_YELLOW,VAL_BLUE};

  // Defines acquisition type and initializes acquisition
  acqtyp=Izero;
  Initialize(&tesrat,&teseve,&testas,&tesfil,&tescha,&tesdim,&tesdat,&tespan);
  // Acquisition and TEST commands
  // Initializes offset constant
  preris=(int)((Dpredut*Dperiod+Dristim)*tesrat);
```

```
  // Allocates test memory
  pos=malloc(tescha*sizeof(int));
  // Loops until Stop acquisition button pressed
  while(acqtyp<Ithree)
  {
   // Loops until teseve events have been triggered on each physical channel
   for(i=Izero;i<teseve;)
   {
    // Reads analog input on specified physical channels
    DAQmxReadAnalogF64(testas,DAQmx_Val_Auto,Dtimout,DAQmx_Val_GroupByChannel,tesdat,
     tesdim,&nsRfec,NULL);
    reaeve++;
    // Loops on physical channels and breaks loop if one channel doesn't trigger
    for(trig_d=Ione,j=Izero;trig_d==Ione&&j<tescha;j++)
    {
     // Finds peak in the first half of the vector
     pos1=j*nsRfec;
     pos2=pos1+nsRfec/Itwo;
     peak=tesdat[pos[j]=pos1];
     for(k=pos1+Ione;k<pos2;k++)
      if(tesdat[k]<peak)
       peak=tesdat[pos[j]=k];
     // Checks if physical channel is triggerable; if not, trig_d is set to zero
     pos[j]-=preris;
     if(pos[j]<pos1)
      trig_d=Izero;
    }
    // Updates graph(s) if each physical channel has triggered
    if(trig_d==Ione)
    {
     i++;
     DeleteGraphPlot(tespan,TESPAN_ASITES,-Ione,VAL_DELAYED_DRAW);
     if(tescha>Ithree)
      DeleteGraphPlot(tespan,TESPAN_CSITES,-Ione,VAL_DELAYED_DRAW);
     for(j=Izero;j<tescha&&j<Ithree;j++)
      PlotY(tespan,TESPAN_ASITES,tesdat+pos[j],nsRfec/Itwo,VAL_DOUBLE,VAL_THIN_LINE,
       VAL_SIMPLE_DOT,VAL_SOLID,Ione,colors[j%Ithree]);
     for(;j<tescha;j++)
      PlotY(tespan,TESPAN_CSITES,tesdat+pos[j],nsRfec/Itwo,VAL_DOUBLE,VAL_THIN_LINE,
       VAL_SIMPLE_DOT,VAL_SOLID,Ione,colors[j%Ithree]);
    }
   }
   // Calculates main panel values
   trieve+=teseve;
   // Updates main panel values
   SetCtrlAttribute(phomul,PHOMUL_TRIEVE,ATTR_CTRL_VAL,trieve);
   SetCtrlAttribute(phomul,PHOMUL_REAEVE,ATTR_CTRL_VAL,reaeve);
   // Processes system events
   ProcessSystemEvents();
  }
  // Deallocates test memory
  free(pos);
  // Terminates acquisition
  Terminate(&testas,&tespan,&tescha,&tesdat,&tesfil);
 }
 return(Izero);
}


int CVICALLBACK Stamon(int panel,int control,int event,void *callbackData,
 int eventData1,int eventData2)
{
 if(event==EVENT_COMMIT)
 {
  TaskHandle montas;
  FILE *monfil=NULL;
  char datnam[21];
  double monrat,*mondat=NULL,*peak=NULL,*PeaVol=NULL,*PeaErr=NULL,baslin;
  int moneve,moncha,mondim,monpan,reaeve=Izero,trieve=Izero,prewid,preris,i,nsRfec,
   trig_d,j,pos1,pos2,pos3,k;
  time_t dattim;

  // Defines acquisition type and initializes acquisition
```

```
acqtyp=Ione;
Initialize(&monrat,&moneve,&montas,&monfil,&moncha,&mondim,&mondat,&monpan);
// Acquisition and MONITOR commands
// Initializes offset constants
prewid=(int)(Dpredut*Dperiod*monrat);
preris=prewid+(int)(Dristim*monrat);
// Allocates monitor memory
peak=malloc(moncha*sizeof(double));
PeaVol=malloc(moncha*sizeof(double));
PeaErr=malloc(moncha*sizeof(double));
// Loops until Stop acquisition button pressed
while(acqtyp<Ithree)
{
 // Clears monitor arrays
 for(i=Izero;i<moncha;i++)
 {
  PeaVol[i]=Dzero;
  PeaErr[i]=Dzero;
 }
 // Loops until moneve events have been triggered on each physical channel
 for(i=Izero;i<moneve;)
 {
  // Reads analog input on specified physical channels
  DAQmxReadAnalogF64(montas,DAQmx_Val_Auto,Dtimout,DAQmx_Val_GroupByChannel,mondat,
   mondim,&nsRfec,NULL);
  reaeve++;
  // Loops on physical channels and breaks loop if one channel doesn't trigger
  for(trig_d=Ione,j=Izero;trig_d==Ione&&j<moncha;j++)
  {
   // Finds peak
   pos1=j*nsRfec;
   pos3=pos1+nsRfec;
   peak[j]=mondat[pos2=pos1];
   for(k=pos1+Ione;k<pos3;k++)
    if(mondat[k]<peak[j])
     peak[j]=mondat[pos2=k];
   // Checks if physical channel is triggerable; if not, trig_d is set to zero
   pos2-=preris;
   if(pos2<pos1)
    trig_d=Izero;
   else
   {
    // Evaluates baseline
    baslin=Dzero;
    pos3=pos2+prewid;
    for(k=pos2;k<pos3;k++)
     baslin+=mondat[k];
    // Subtracts baseline
    peak[j]-=baslin/(double)prewid;
   }
  }
  // Updates monitor arrays if each physical channel has triggered
  if(trig_d==Ione)
  {
   i++;
   for(j=Izero;j<moncha;j++)
   {
    PeaVol[j]+=peak[j];
    PeaErr[j]+=peak[j]*peak[j];
   }
  }
 }
 // Calculates main panel values
 trieve+=moneve;
 for(i=Izero;i<moncha;i++)
 {
  PeaVol[i]/=(double)moneve;
  PeaErr[i]=PeaErr[i]/(double)moneve-PeaVol[i]*PeaVol[i];
  if(PeaErr[i]>Dzero)
   PeaErr[i]=sqrt(PeaErr[i]/(double)moneve);
  else
   PeaErr[i]=Dzero;
 }
 // Updates main panel values
```

```
   switch(moncha)
   {
    case 6:
     SetCtrlAttribute(phomul,PHOMUL_CH5ERR,ATTR_CTRL_VAL,PeaErr[Ifive]*De3);
     SetCtrlAttribute(phomul,PHOMUL_CH5PEA,ATTR_CTRL_VAL,PeaVol[Ifive]*De3);
    case 5:
     SetCtrlAttribute(phomul,PHOMUL_CH4ERR,ATTR_CTRL_VAL,PeaErr[Ifour]*De3);
     SetCtrlAttribute(phomul,PHOMUL_CH4PEA,ATTR_CTRL_VAL,PeaVol[Ifour]*De3);
    case 4:
     SetCtrlAttribute(phomul,PHOMUL_CH3ERR,ATTR_CTRL_VAL,PeaErr[Ithree]*De3);
     SetCtrlAttribute(phomul,PHOMUL_CH3PEA,ATTR_CTRL_VAL,PeaVol[Ithree]*De3);
    case 3:
     SetCtrlAttribute(phomul,PHOMUL_CH2ERR,ATTR_CTRL_VAL,PeaErr[Itwo]*De3);
     SetCtrlAttribute(phomul,PHOMUL_CH2PEA,ATTR_CTRL_VAL,PeaVol[Itwo]*De3);
    case 2:
     SetCtrlAttribute(phomul,PHOMUL_CH1ERR,ATTR_CTRL_VAL,PeaErr[Ione]*De3);
     SetCtrlAttribute(phomul,PHOMUL_CH1PEA,ATTR_CTRL_VAL,PeaVol[Ione]*De3);
   }
   SetCtrlAttribute(phomul,PHOMUL_CH0ERR,ATTR_CTRL_VAL,PeaErr[Izero]*De3);
   SetCtrlAttribute(phomul,PHOMUL_CH0PEA,ATTR_CTRL_VAL,PeaVol[Izero]*De3);
   SetCtrlAttribute(phomul,PHOMUL_TRIEVE,ATTR_CTRL_VAL,trieve);
   SetCtrlAttribute(phomul,PHOMUL_REAEVE,ATTR_CTRL_VAL,reaeve);
   // Updates strip chart(s)
   if(moncha<Ifour)
    PlotStripChart(monpan,MEAPAN_ASIMEA,PeaVol,moncha,Izero,Izero,VAL_DOUBLE);
   else
   {
    PlotStripChart(monpan,MEAPAN_ASIMEA,PeaVol,Ithree,Izero,Izero,VAL_DOUBLE);
    PlotStripChart(monpan,MEAPAN_CSIMEA,PeaVol,moncha-Ithree,Ithree,Izero,VAL_DOUBLE);
   }
   // Writes disk file
   if(monfil!=NULL)
   {
    time(&dattim);
    strftime(datnam,21,"%Y/%m/%d %H:%M:%S ",localtime(&dattim));
    fprintf(monfil,"%s",datnam);
    for(i=0;i<moncha;i++)
     fprintf(monfil,"%.2lf %.2lf ",PeaVol[i]*De3,PeaErr[i]*De3);
    fprintf(monfil,"\n");
   }
   // Processes system events
   ProcessSystemEvents();
  }
  // Deallocates monitor memory
  free(PeaErr);
  free(PeaVol);
  free(peak);
  // Terminates acquisition
  Terminate(&montas,&monpan,&moncha,&mondat,&monfil);
 }
 return(Izero);
}


int CVICALLBACK Staana(int panel,int control,int event,void *callbackData,
 int eventData1,int eventData2)
{
 if(event==EVENT_COMMIT)
 {
  TaskHandle anatas;
  FILE *anafil=NULL;
  char datnam[21];
  const double
   c1=Dtau_H/(Db*sqrt(Dtau_L*Dtau_L+Dtau_H*Dtau_H+(double)Itwo*Da*Dtau_L*Dtau_H)),
   c2=Da/Dtau_H,c3=Db/Dtau_H,c4=atan(-(Dtau_L+Da*Dtau_H)/(Db*Dtau_H)),
   c5=-Dtau_H*Dtau_H/(Dtau_L*Dtau_L+Dtau_H*Dtau_H+(double)Itwo*Da*Dtau_L*Dtau_H),
   c6=-(double)Ione/Dtau_L;
  double anarat,*anadat=NULL,*peak=NULL,*PeaVol=NULL,*PeaErr=NULL,baslin,den,g;
  int anaeve,anacha,anadim,anapan,reaeve=Izero,trieve=Izero,prewid,preris,peawid,i,
   nsRfec,trig_d,j,pos1,pos2,pos3,pos4,k;
  time_t dattim;

  // Defines acquisition type and initializes acquisition
```

```
acqtyp=Itwo;
Initialize(&anarat,&anaeve,&anatas,&anafil,&anacha,&anadim,&anadat,&anapan);
// Acquisition and ANALYSIS commands
// Initializes offset constants
prewid=(int)(Dpredut*Dperiod*anarat);
preris=prewid+(int)(Dristim*anarat);
peawid=(int)(Dpeadut*Dperiod*anarat);
anarat=(double)Ione/anarat;
// Allocates analysis memory
peak=malloc(anacha*sizeof(double));
PeaVol=malloc(anacha*sizeof(double));
PeaErr=malloc(anacha*sizeof(double));
// Loops until Stop acquisition button pressed
while(acqtyp<Ithree)
{
 // Clears analysis arrays
 for(i=Izero;i<anacha;i++)
 {
  PeaVol[i]=Dzero;
  PeaErr[i]=Dzero;
 }
 // Loops until anaeve events have been triggered on each physical channel
 for(i=Izero;i<anaeve;)
 {
  // Reads analog input on specified physical channels
  DAQmxReadAnalogF64(anatas,DAQmx_Val_Auto,Dtimout,DAQmx_Val_GroupByChannel,anadat,
   anadim,&nsRfec,NULL);
  reaeve++;
  // Loops on physical channels and breaks loop if one channel doesn't trigger
  for(trig_d=Ione,j=Izero;trig_d==Ione&&j<anacha;j++)
  {
   // Finds peak
   pos1=j*nsRfec;
   pos3=pos1+nsRfec;
   peak[j]=anadat[pos2=pos1];
   for(k=pos1+Ione;k<pos3;k++)
    if(anadat[k]<peak[j])
     peak[j]=anadat[pos2=k];
   // Checks if physical channel is triggerable; if not, trig_d is set to zero
   pos2-=preris;
   pos4=pos2+prewid;
   if(pos2<pos1||pos4+peawid>pos3)
    trig_d=Izero;
   else
   {
    // Evaluates baseline
    baslin=Dzero;
    for(k=pos2;k<pos4;k++)
     baslin+=anadat[k];
    baslin/=(double)prewid;
    // Fits peak and subtracts baseline
    peak[j]=den=Dzero;
    for(k=Izero;k<peawid;k++)
    {
     g=c1*exp(c2*(double)k*anarat)*cos(c3*(double)k*anarat+c4)+c5*exp(c6*(double)k*
      anarat);
     peak[j]+=g*(anadat[k+pos4]-baslin);
     den+=g*g;
    }
    peak[j]*=Dscafac/den;
   }
  }
  // Updates analysis arrays if each physical channel has triggered
  if(trig_d==Ione)
  {
   i++;
   for(j=Izero;j<anacha;j++)
   {
    PeaVol[j]+=peak[j];
    PeaErr[j]+=peak[j]*peak[j];
   }
  }
 }
 // Calculates main panel values
```

```
   trieve+=anaeve;
   for(i=Izero;i<anacha;i++)
   {
    PeaVol[i]/=(double)anaeve;
    PeaErr[i]=PeaErr[i]/(double)anaeve-PeaVol[i]*PeaVol[i];
    if(PeaErr[i]>Dzero)
     PeaErr[i]=sqrt(PeaErr[i]/(double)anaeve);
    else
     PeaErr[i]=Dzero;
   }
   // Updates main panel values
   switch(anacha)
   {
    case 6:
     SetCtrlAttribute(phomul,PHOMUL_CH5ERR,ATTR_CTRL_VAL,PeaErr[Ifive]*De3);
     SetCtrlAttribute(phomul,PHOMUL_CH5PEA,ATTR_CTRL_VAL,PeaVol[Ifive]*De3);
    case 5:
     SetCtrlAttribute(phomul,PHOMUL_CH4ERR,ATTR_CTRL_VAL,PeaErr[Ifour]*De3);
     SetCtrlAttribute(phomul,PHOMUL_CH4PEA,ATTR_CTRL_VAL,PeaVol[Ifour]*De3);
    case 4:
     SetCtrlAttribute(phomul,PHOMUL_CH3ERR,ATTR_CTRL_VAL,PeaErr[Ithree]*De3);
     SetCtrlAttribute(phomul,PHOMUL_CH3PEA,ATTR_CTRL_VAL,PeaVol[Ithree]*De3);
    case 3:
     SetCtrlAttribute(phomul,PHOMUL_CH2ERR,ATTR_CTRL_VAL,PeaErr[Itwo]*De3);
     SetCtrlAttribute(phomul,PHOMUL_CH2PEA,ATTR_CTRL_VAL,PeaVol[Itwo]*De3);
    case 2:
     SetCtrlAttribute(phomul,PHOMUL_CH1ERR,ATTR_CTRL_VAL,PeaErr[Ione]*De3);
     SetCtrlAttribute(phomul,PHOMUL_CH1PEA,ATTR_CTRL_VAL,PeaVol[Ione]*De3);
   }
   SetCtrlAttribute(phomul,PHOMUL_CH0ERR,ATTR_CTRL_VAL,PeaErr[Izero]*De3);
   SetCtrlAttribute(phomul,PHOMUL_CH0PEA,ATTR_CTRL_VAL,PeaVol[Izero]*De3);
   SetCtrlAttribute(phomul,PHOMUL_TRIEVE,ATTR_CTRL_VAL,trieve);
   SetCtrlAttribute(phomul,PHOMUL_REAEVE,ATTR_CTRL_VAL,reaeve);
   // Updates strip chart(s)
   if(anacha<Ifour)
    PlotStripChart(anapan,MEAPAN_ASIMEA,PeaVol,anacha,Izero,Izero,VAL_DOUBLE);
   else
   {
    PlotStripChart(anapan,MEAPAN_ASIMEA,PeaVol,Ithree,Izero,Izero,VAL_DOUBLE);
    PlotStripChart(anapan,MEAPAN_CSIMEA,PeaVol,anacha-Ithree,Ithree,Izero,VAL_DOUBLE);
   }
   // Writes disk file
   if(anafil!=NULL)
   {
    time(&dattim);
    strftime(datnam,21,"%Y/%m/%d %H:%M:%S ",localtime(&dattim));
    fprintf(anafil,"%s",datnam);
    for(i=0;i<anacha;i++)
     fprintf(anafil,"%.2lf %.2lf ",PeaVol[i]*De3,PeaErr[i]*De3);
    fprintf(anafil,"\n");
   }
   // Processes system events
   ProcessSystemEvents();
  }
  // Deallocates analysis memory
  free(PeaErr);
  free(PeaVol);
  free(peak);
  // Terminates acquisition
  Terminate(&anatas,&anapan,&anacha,&anadat,&anafil);
 }
 return(Izero);
}


int CVICALLBACK Stoacq(int panel,int control,int event,void *callbackData,
 int eventData1,int eventData2)
{
 if(event==EVENT_COMMIT)
  // Changes acquisition type
  acqtyp+=Ithree;
 return(Izero);
}
```

```
int CVICALLBACK Quipro(int panel,int control,int event,void *callbackData,
 int eventData1,int eventData2)
{
 if(event==EVENT_COMMIT)
  // Causes RunUserInterface to return
  QuitUserInterface(Izero);
 return(Izero);
}


void Initialize(double *ratadr,int *eveadr,TaskHandle *tasadr,FILE **filadr,
 int *chaadr,int *dimadr,double **datadr,int *panadr)
{
 char phycha[128],filnam[39];
 double maxinp,mininp;
 int diswri,nsNfec,nsAfec=Izero;
 time_t filtim;

 // Reads input values from main panel
 GetCtrlVal(phomul,PHOMUL_PHYCHA,phycha);
 GetCtrlVal(phomul,PHOMUL_MAXINP,&maxinp);
 GetCtrlVal(phomul,PHOMUL_MININP,&mininp);
 GetCtrlVal(phomul,PHOMUL_SAMRAT,ratadr);
 GetCtrlVal(phomul,PHOMUL_EVEPER,eveadr);
 GetCtrlVal(phomul,PHOMUL_DISWRI,&diswri);
 // Creates task and configures it
 DAQmxCreateTask(NULL,tasadr);
 DAQmxCreateAIVoltageChan(*tasadr,phycha,NULL,DAQmx_Val_Diff,mininp*De_3,maxinp*De_3,
  DAQmx_Val_Volts,NULL);
 DAQmxCfgSampClkTiming(*tasadr,NULL,*ratadr*De3,DAQmx_Val_Rising,DAQmx_Val_ContSamps,
  Ione);
 // Opens disk file
 if(acqtyp!=Izero&&diswri==Ione)
 {
  time(&filtim);
  strftime(filnam,39,"PMTsDAQsw_Data_%Y.%m.%d_%H.%M.%S.dat",localtime(&filtim));
  *filadr=fopen(filnam,"w");
 }
 // Allocates reading data memory
 DAQmxGetTaskAttribute(*tasadr,DAQmx_Task_NumChans,chaadr);
 nsNfec=(int)(*ratadr*Dperiod);
 if(acqtyp==Izero)
  nsNfec*=Itwo;
 *dimadr=*chaadr*nsNfec;
 *datadr=malloc(*dimadr*sizeof(double));
 // Changes main panel dimmed/not dimmed controls attribute
 SetCtrlAttribute(phomul,PHOMUL_PHYCHA,ATTR_DIMMED,Ione);
 SetCtrlAttribute(phomul,PHOMUL_MAXINP,ATTR_DIMMED,Ione);
 SetCtrlAttribute(phomul,PHOMUL_MININP,ATTR_DIMMED,Ione);
 SetCtrlAttribute(phomul,PHOMUL_SAMRAT,ATTR_DIMMED,Ione);
 SetCtrlAttribute(phomul,PHOMUL_EVEPER,ATTR_DIMMED,Ione);
 SetCtrlAttribute(phomul,PHOMUL_REAEVE,ATTR_DIMMED,Izero);
 SetCtrlAttribute(phomul,PHOMUL_TRIEVE,ATTR_DIMMED,Izero);
 if(acqtyp!=Izero)
 {
  switch(*chaadr)
  {
   case 6:
    SetCtrlAttribute(phomul,PHOMUL_CH5ERR,ATTR_DIMMED,Izero);
    SetCtrlAttribute(phomul,PHOMUL_CH5PEA,ATTR_DIMMED,Izero);
   case 5:
    SetCtrlAttribute(phomul,PHOMUL_CH4ERR,ATTR_DIMMED,Izero);
    SetCtrlAttribute(phomul,PHOMUL_CH4PEA,ATTR_DIMMED,Izero);
   case 4:
    SetCtrlAttribute(phomul,PHOMUL_CH3ERR,ATTR_DIMMED,Izero);
    SetCtrlAttribute(phomul,PHOMUL_CH3PEA,ATTR_DIMMED,Izero);
   case 3:
    SetCtrlAttribute(phomul,PHOMUL_CH2ERR,ATTR_DIMMED,Izero);
    SetCtrlAttribute(phomul,PHOMUL_CH2PEA,ATTR_DIMMED,Izero);
   case 2:
    SetCtrlAttribute(phomul,PHOMUL_CH1ERR,ATTR_DIMMED,Izero);
    SetCtrlAttribute(phomul,PHOMUL_CH1PEA,ATTR_DIMMED,Izero);
  }
```

```
  SetCtrlAttribute(phomul,PHOMUL_CH0ERR,ATTR_DIMMED,Izero);
  SetCtrlAttribute(phomul,PHOMUL_CH0PEA,ATTR_DIMMED,Izero);
 }
 SetCtrlAttribute(phomul,PHOMUL_STATES,ATTR_DIMMED,Ione);
 SetCtrlAttribute(phomul,PHOMUL_STAMON,ATTR_DIMMED,Ione);
 SetCtrlAttribute(phomul,PHOMUL_STAANA,ATTR_DIMMED,Ione);
 SetCtrlAttribute(phomul,PHOMUL_DISWRI,ATTR_DIMMED,Ione);
 SetCtrlAttribute(phomul,PHOMUL_STOACQ,ATTR_DIMMED,Izero);
 SetCtrlAttribute(phomul,PHOMUL_QUIPRO,ATTR_DIMMED,Ione);
 // Loads test/monitor/analysis panel, configures it and displays it
 if(acqtyp==Izero)
 {
  *panadr=LoadPanel(Izero,"PMTsDAQsw.uir",TESPAN);
  SetCtrlAttribute(*panadr,TESPAN_ASITES,ATTR_XAXIS_GAIN,(double)Ione/(*ratadr));
  SetAxisScalingMode(*panadr,TESPAN_ASITES,VAL_BOTTOM_XAXIS,VAL_MANUAL,Dzero,
   (double)(nsNfec/Itwo));
  SetAxisScalingMode(*panadr,TESPAN_ASITES,VAL_LEFT_YAXIS,VAL_MANUAL,mininp*De_3,
   maxinp*De_3);
  SetCtrlAttribute(*panadr,TESPAN_CSITES,ATTR_XAXIS_GAIN,(double)Ione/(*ratadr));
  SetAxisScalingMode(*panadr,TESPAN_CSITES,VAL_BOTTOM_XAXIS,VAL_MANUAL,Dzero,
   (double)(nsNfec/Itwo));
  SetAxisScalingMode(*panadr,TESPAN_CSITES,VAL_LEFT_YAXIS,VAL_MANUAL,mininp*De_3,
   maxinp*De_3);
 }
 else
 {
  *panadr=LoadPanel(Izero,"PMTsDAQsw.uir",MEAPAN);
  if(acqtyp==Itwo)
   SetPanelAttribute(*panadr,ATTR_TITLE,"Analysis panel");
  if(*chaadr<Ifour)
   SetCtrlAttribute(*panadr,MEAPAN_ASIMEA,ATTR_NUM_TRACES,*chaadr);
  else
   SetCtrlAttribute(*panadr,MEAPAN_CSIMEA,ATTR_NUM_TRACES,*chaadr-Ithree);
  SetAxisScalingMode(*panadr,MEAPAN_ASIMEA,VAL_LEFT_YAXIS,VAL_MANUAL,mininp*De_3,
   maxinp*De_3);
  SetAxisScalingMode(*panadr,MEAPAN_CSIMEA,VAL_LEFT_YAXIS,VAL_MANUAL,mininp*De_3,
   maxinp*De_3);
 }
 DisplayPanel(*panadr);
 // Starts task and configures reading parameters
 DAQmxSetReadAttribute(*tasadr,DAQmx_Read_OverWrite,DAQmx_Val_OverwriteUnreadSamps);
 DAQmxSetReadAttribute(*tasadr,DAQmx_Read_WaitMode,DAQmx_Val_Sleep);
 DAQmxSetReadAttribute(*tasadr,DAQmx_Read_SleepTime,De_3);
 DAQmxStartTask(*tasadr);
 while(nsAfec<nsNfec)
  DAQmxGetReadAttribute(*tasadr,DAQmx_Read_AvailSampPerChan,&nsAfec);
 DAQmxSetReadAttribute(*tasadr,DAQmx_Read_RelativeTo,DAQmx_Val_MostRecentSamp);
 DAQmxSetReadAttribute(*tasadr,DAQmx_Read_Offset,-nsNfec);
 return;
}


void Terminate(TaskHandle *tasadr,int *panadr,int *chaadr,double **datadr,FILE **filadr)
{
 // Stops task
 DAQmxStopTask(*tasadr);
 // Discards test/monitor/analysis panel
 DiscardPanel(*panadr);
 // Changes main panel dimmed/not dimmed controls attribute
 SetCtrlAttribute(phomul,PHOMUL_PHYCHA,ATTR_DIMMED,Izero);
 SetCtrlAttribute(phomul,PHOMUL_MAXINP,ATTR_DIMMED,Izero);
 SetCtrlAttribute(phomul,PHOMUL_MININP,ATTR_DIMMED,Izero);
 SetCtrlAttribute(phomul,PHOMUL_SAMRAT,ATTR_DIMMED,Izero);
 SetCtrlAttribute(phomul,PHOMUL_EVEPER,ATTR_DIMMED,Izero);
 SetCtrlAttribute(phomul,PHOMUL_REAEVE,ATTR_DIMMED,Ione);
 SetCtrlAttribute(phomul,PHOMUL_TRIEVE,ATTR_DIMMED,Ione);
 if(acqtyp!=Ithree)
 {
  switch(*chaadr)
  {
   case 6:
    SetCtrlAttribute(phomul,PHOMUL_CH5ERR,ATTR_DIMMED,Ione);
    SetCtrlAttribute(phomul,PHOMUL_CH5PEA,ATTR_DIMMED,Ione);
```

```
   case 5:
    SetCtrlAttribute(phomul,PHOMUL_CH4ERR,ATTR_DIMMED,Ione);
    SetCtrlAttribute(phomul,PHOMUL_CH4PEA,ATTR_DIMMED,Ione);
   case 4:
    SetCtrlAttribute(phomul,PHOMUL_CH3ERR,ATTR_DIMMED,Ione);
    SetCtrlAttribute(phomul,PHOMUL_CH3PEA,ATTR_DIMMED,Ione);
   case 3:
    SetCtrlAttribute(phomul,PHOMUL_CH2ERR,ATTR_DIMMED,Ione);
    SetCtrlAttribute(phomul,PHOMUL_CH2PEA,ATTR_DIMMED,Ione);
   case 2:
    SetCtrlAttribute(phomul,PHOMUL_CH1ERR,ATTR_DIMMED,Ione);
    SetCtrlAttribute(phomul,PHOMUL_CH1PEA,ATTR_DIMMED,Ione);
  }
  SetCtrlAttribute(phomul,PHOMUL_CH0ERR,ATTR_DIMMED,Ione);
  SetCtrlAttribute(phomul,PHOMUL_CH0PEA,ATTR_DIMMED,Ione);
 }
 SetCtrlAttribute(phomul,PHOMUL_STATES,ATTR_DIMMED,Izero);
 SetCtrlAttribute(phomul,PHOMUL_STAMON,ATTR_DIMMED,Izero);
 SetCtrlAttribute(phomul,PHOMUL_STAANA,ATTR_DIMMED,Izero);
 SetCtrlAttribute(phomul,PHOMUL_DISWRI,ATTR_DIMMED,Izero);
 SetCtrlAttribute(phomul,PHOMUL_STOACQ,ATTR_DIMMED,Ione);
 SetCtrlAttribute(phomul,PHOMUL_QUIPRO,ATTR_DIMMED,Izero);
 // Deallocates reading data memory
 free(*datadr);
 // Closes disk file
 if(acqtyp!=Ithree&&*filadr!=NULL)
  fclose(*filadr);
 // Clears task
 DAQmxClearTask(*tasadr);
 return;
}
```

BIBLIOGRAPHY

[1] – Particle Data Group, *Particle Physics Booklet* (Institute of Physics, 2006)

[2] – P. Nason et al., *Bottom Production* (G. Altarelli and M. L. Mangano, 2000)

[3] – LHCb Collaboration, *LHCb Technical Proposal* (CERN LHCC, 1998)

[4] – LHCb Collaboration, *LHCb VELO Technical Design Report* (CERN LHCC, 2001)

[5] – LHCb Collaboration, *LHCb Magnet Technical Design Report* (CERN LHCC, 2000)

[6] – LHCb Collaboration, *LHCb Inner Tracker Technical Design Report* (CERN LHCC, 2002)

[7] – LHCb Collaboration, *LHCb Outer Tracker Technical Design Report* (CERN LHCC, 2001)

[8] – LHCb Collaboration, *LHCb Calorimeters Technical Design Report* (CERN LHCC, 2000)

[9] – LHCb Collaboration, *LHCb Muon System Technical Design Report* (CERN LHCC, 2001)

[10] – LHCb Collaboration, *LHCb Technical Design Report – Reoptimized Detector Design and Performance* (CERN LHCC, 2003)

[11] – LHCb Collaboration, *Addendum to the LHCb Muon System Technical Design Report* (CERN LHCC, 2003)

[12] – LHCb Collaboration, *Second Addendum to the LHCb Muon System Technical Design Report* (CERN LHCC, 2005)

[13] – LHCb Collaboration, *LHCb Trigger System Technical Design Report* (CERN LHCC, 2003)

[14] – LHCb Collaboration, *LHCb RICH Technical Design Report* (CERN LHCC, 2000)

[15] – Laura Somerville, *Pixel Hybrid Photon Detectors for the Ring Imaging Cherenkov Detectors of LHCb* (Elsevier, 2005)

[16] – Thierry Gys, *Production of 500 Pixel Hybrid Photon Detectors for the RICH Counters of LHCb* (CERN, 2005)

[17] – http://www.hamamatsu.com

[18] – http://www.wikipedia.it

[19] – http://www.mitsubushielectric.com

[20] – http://www.ni.com

ACKNOWLEDGEMENTS

Here I am at the end of my thesis. I have to acknowledge so many people who helped me during the last ten months. A grateful thank to Clara Matteuzzi for her competent supervision and for giving me the possibility to participate to the LHCb collaboration. Thank you to Carmelo D'Ambrosio for receiving me in CERN, for helping me in the difficulties and for constantly trusting me. A special thank to Gianluigi Pessina for carefully supervising me during all my thesis, from the first electronics design to the elimination of evil ground problems in the actual apparatus. Thanks also to Olav Ullaland for helping me at CERN every time I had a request and for correcting my terrible English in this thesis.
My gratitude goes to all the people I worked with: Thierry Gys, Didier Piedigrossi, Christophe Frei, Erich Albrecht, Stephen Wotton, Richard Jacobsson, Barbara, Nicola, Sean, Gareth, Hugh and anybody else in CERN who answered my questions and helped me in the realization of this thesis.
The particle physics group of the University of Milano–Bicocca and especially to Marta Calvi, Franco Chignoli, Roberto Mazza, Tito Bellunato and Davide L. Perego.
Of course a special thank goes to all my relatives, who constantly encouraged me. In particular I have to thank my mummy, my grandmother Teresa and my dear sweet great–grandma Angela.
Thanks to my Greek family in Saint–Genis–Poully, Yiota Foka, Christina Foka and Katerina Foka for making me feel at home during all my stay at CERN.
All the other people I knew in CERN last summer: Luana, Sarah, Sir Leon, the Polish one, Madalina, Aberto, Gabriel, Bernardo, Simona, Conor, Caterina, Casha, Andrew, Andrei, David and all the others. Thanks to all of you for making CERN so special.
Thanks to my good friend caffeine for helping me to work till late for so many days…
Last but not least, all my friends in Milano, inside and outside University: Miglio, Francesca, Valentina, Cippy, Tamby and Filippo (the bike group!), Ciccio, Mimì, Patchouly, Bobo, Djumbo, LaIlaria, LaSara, Rosy, LaMary, LaMara, all my friends at the University, all the car park crew and all the people of the Desio library.